CHALMERS
UNIVERSITY OF TECHNOLOGY

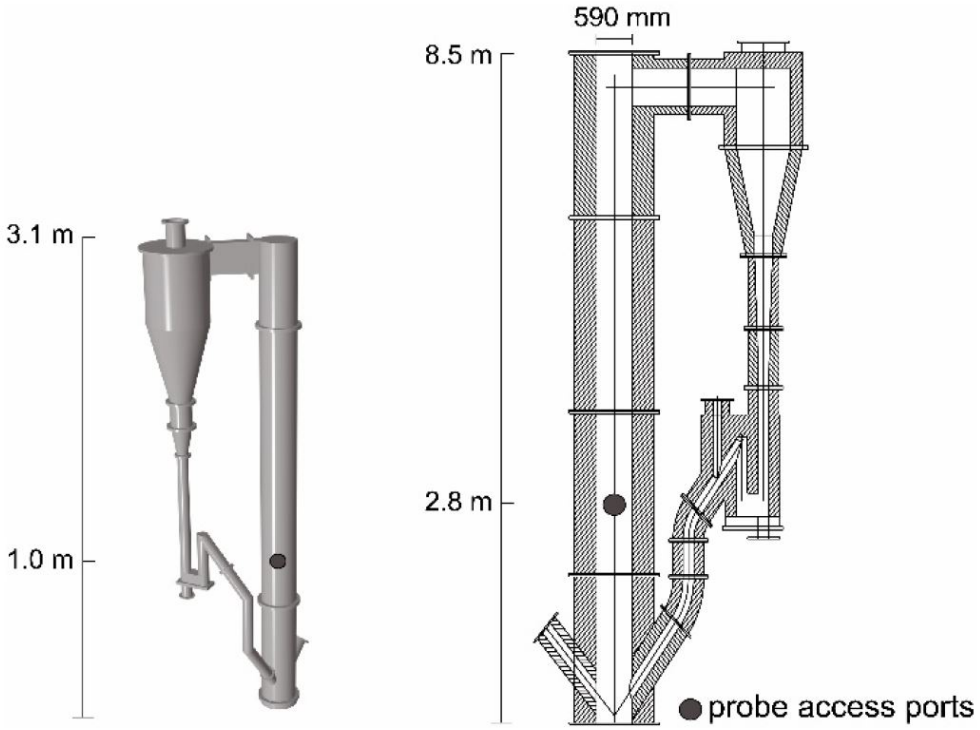

Flow Hydrodynamics in a Scaled Cold Flow CFB Model

Investigation with a Capacitance Probe System

Master's thesis in Innovative and Sustainable Chemical Engineering

VIKTOR ANDERSSON
CHRISTOFFER SELLGREN

Department of Chemical and Biological Engineering
Division of Environmental Inorganic Chemistry
Chalmers University of Technology
Gothenburg, Sweden 2018

Master's thesis 2018:KBTX12

Investigation of the Flow Hydrodynamics in a Scaled Cold Flow CFB Model

Measurements conducted with a Capacitance Probe System

Viktor Andersson
Christoffer Sellgren

CHALMERS
UNIVERSITY OF TECHNOLOGY

Department of Chemical and Biological Engineering
Division of Environmental Inorganic Chemistry
Chalmers University of Technology
Gothenburg, Sweden 2018

Investigation of the flow hydrodynamics in a scaled cold flow CFB model
Measurements conducted with a capacitance probe system
Viktor Andersson
Christoffer Sellgren

Supervisor: Alexander Daikeler, Institute of Energy Systems and Technology, Darmstadt Technical University
Examiner: Henrik Leion, Department of Chemical and Biological Engineering

Master's Thesis 2018:KBTX12
Department of Chemical and Biological Engineering
Division of Environmental Inorganic Chemistry
Chalmers University of Technology
SE-412 96 Gothenburg
Telephone +46 31 772 1000

Cover: Circulating fluidized bed test rigs. Scaled cold flow CFM200 model (left) and hot 1MW CFB600 pilot (right). Daikeler (2018), Darmstadt.

Typeset in LaTeX
Gothenburg, Sweden 2018

Abstract

One way to tackle the ever increasing threat of disasters due to global warming and other environmental issues could be implementation of circulating fluidized bed (CFB) technology, in which there is a need to improve the available knowledge regarding the flow structure and scale up processes. In order to more easily investigate this, the Institute of Energy Systems and Technology at Darmstadt Technical University constructed a scaled, 0.36:1, cold flow model of a hot 1 MW_{th} pilot plant located at campus. The cold flow model and most of its experimental parameters are scaled according to the simplified Glicksman scaling laws. Previous studies have been conducted without scaling the size of the particles used as bed material, which is the focus in this study. However, the density ratio is not scaled accordingly, with the motivation that the hot pilot operates in the viscous limit regime and thus the particle densities might be negligible [1].

Profile measurements of particle concentrations and velocities are conducted at various heights within the cold flow model using a capacitance probe system. The results are validated using continuously conducted pressure profiles, material properties, different entrance points on the riser as well as repeating measurements.

As expected in CFB systems with relatively low particle concentrations and superficial gas velocities (<10 m/s), the core-annular flow structure is present in most of the resulting velocity- and concentration profiles. Depending on the superficial gas velocity and particle size distributions, the core-annular flow structure is often obstructed in the lower regions of the riser. This is believed to be caused by the high amount of recirculating bed material through the loop seal, together with a high resistance particle filter at the air distribution plate, causing particle accumulation in the center of the riser.

The capacitance probe results were well comparable to the hot pilot plant results and showed good accordance to the simplified Glicksman scaling laws. The minor variation in inventory, small change in physical properties of the material and displayed consistency of the equipment all indicate that the acquired data is suitable for further processing.

Keywords: Circulating fluidized bed, scale-up process, flow hydrodynamics, capacitance probe system

Acknowledgements

Firstly we would like to thank our examiner and mentor Dr. Henrik Leion at Chalmers University of Technology for making it possible to do most of the thesis work abroad, but also for his encouragement and trust in us.

We would also like to thank our supervisor Dipl.-Ing. Alexander Daikeler at Darmstadt Technical University. The door to Daikeler's office was always open whenever we ran into a trouble spot or had questions regarding research or writing. Without his passionate participation and input, the experimental work could not have been as successfully conducted. He consistently allowed this paper to be our own work, but steered us in the right direction whenever he thought we needed it. Beside that, Daikeler was very friendly and helped a lot during our time in Germany.

We must also express our profound gratitude to Darmstadt Technical University, Germany, and mostly to the Institute for Energy Systems and Technology. Not only for giving us the opportunity to work there, but also by providing the necessary means to conduct the experiments.

We would also like to acknowledge Ivana Stanicic at Chalmers University of Technology as the second reader. Her valuable comments on this thesis was essential to make the overall impression professional.

Lastly we would like to thank Erasmus+ traineeships for their help providing financial support.

Thank you,

Viktor Andersson
Christoffer Sellgren

Contents

1 Introduction

With the ever increasing threat of disasters due to global warming and other environmental issues, the society has established a demand for effective combustion and exhaust gas treatments. One way to tackle these issues could be the implementation of circulating fluidized bed (CFB) technology. With current advances in the field, there is a need to improve the available knowledge regarding the flow structure and scale up processes in these systems. Therefore the Institute of Energy Systems and Technology at Darmstadt Technical University operates a 1 MW_{th} CFB pilot plant. The pilot is used for investigation of several processes like carbonate and chemical looping in semi-industrial scales.

In order to more easily investigate the flow hydrodynamics of CFB reactors the University constructed a scaled, 0.36:1, cold flow model of the pilot plant. This cold flow model is scaled and operated according to the simplified Glicksman scaling laws in order to accurately reproduce the flow structure of the hot CFB reactor.

A capacitance probe measurement system is used to determine local particle concentration and velocity profiles inside the hot and cold CFB reactor. For the scaled cold flow model several studies have already been conducted with this system. However, the particles in the previous studies were not scaled together with the reactor, but instead same particles with the same size distribution were used for both reactor systems.

In order for the scaling laws to be fulfilled very fine particles with very high apparent density must be used. However, aspects like cost and toxicity makes implementation of these materials difficult. A way to work around this problem can be to scale only the size distribution while keeping the density constant. This might be sufficient since the CFB reactor of the 1 MW_{th} pilot plant is operated in the viscous limit regime with rather low particle Reynolds numbers (Re_p<10) [1].

1.1 Aim of the project

The aim is to conduct in-bed measurements, in the scaled cold flow model, using glass microbeads with varying particle size distributions (PSD) at varied superficial gas velocities. Eventually this work will clarify the influence of particle size distribution on the flow hydrodynamics within CFB reactors.

1.2 Method

Profile measurements of particle concentrations and velocities are conducted at various heights within the cold flow model using a capacitance probe system. Several measurements for calibration and material properties are conducted together with continuously acquired pressure profiles and, externally measured, overall solids entrainment rates. These are used for validating the capacitance probe measurements.

1.3 Constraints

The experimental set up is limited to include four different superficial gas velocities and three different particle size distributions of the bed material.

Measurements are conducted at six out of twelve heights on the left hand side of the reactor. From the same number of right ports, three are studied with one operating superficial gas velocity.

The capacitance probe is mounted on a scale with 0.1 millimeter precision. Measurements are conducted at 38 points across the total riser diameter of 213 millimeter.

2 Theory and Background

The green house gas emission from a combustion plant may be reduced by applying a carbon capture and storage (CCS) system. If combustion is performed with biomass as fuel source and the carbon dioxide can be completely separated and stored, it will result in negative carbon dioxide emissions [2] [3]. Chemical looping combustion, CLC, is one of several methods that can enable carbon dioxide to be captured. CLC is a technological process typically employing a dual circulating fluidized bed system where a metal oxide, employed as bed material, is providing oxygen for combustion in the fuel reactor. The reduced metal is then transferred to the second bed, the air reactor, and re-oxidized before being reintroduced back to the fuel reactor, completing the loop. In that way the fresh air and fuel can be completely separated which simplifies the number of chemical reactions during combustion. Since the oxygen supply comes without nitrogen and the trace gases found in air, the primary source for formation of nitrogen oxide, NOx, is eliminated. Thereby the produced flue gas mostly consist of carbon dioxide and water vapor, beside some other trace pollutants depending on the source of fuel and efficiency of combustion. A well functioned fluidized bed system is therefore of high importance to enable complete combustion and a possibility for efficient exhaust gas separation.

Another common application for circulating fluidized beds is Fluidized Catalytic Cracking, FCC, in the petroleum industry. After crude oil has been distilled and separated into intermediate products they are fed into a FCC unit for further reprocessing. The FCC utilize micro-spherical catalysts as a bed material to break down long carbon chains into high value fuel or other products for the petrochemical industry. The fluidization gas arise from the preheated feed which vaporizes upon contact with the bed material. As the solid bed material leaves the riser it is separated using a cyclone, scrubbed and preheated, in order to vaporize the feed again, before being re-introduced to the riser. The cracking starts as soon as the feed has been vaporized, and is usually completed in three seconds[4]. Because of this, it is crucial to know the internal flow structure since any deviation from the preferred residence time creates a low product selectivity. Reza Sadegbeigi [4] claims that due to the FCC flexibility it could soon see some application in the bio-fuel market.

CLC and FCC are just a two of many applications which can apply the concept of circulating fluidized beds, CFB. With current advances in the field there is a need to improve the available knowledge regarding the flow structure and scale up processes.

2.1 Circulating Fluidized Beds

Circulating fluidized beds usually consist of three main components. A riser where the combustion takes place, a cyclone which uses the centrifugal force to separate the particles from the gas stream and a fluidized loop seal, which collect and reintroduce the particles back to the riser, see figure 1. The main difference between circulating

fluidized beds and other fluidized beds is that they usually have a significantly higher superficial gas, or liquid, velocity causing particles to leave the riser. The mass entrainment creates the need for effective gas-solid separation, in order to keep a constant inventory in the riser, which is usually done with a cyclone. The extra equipment may increase the cost of a CFB unit. However, it does not only create a possibility to extract and regenerate bed material, but also creates more available heat transfer surfaces.

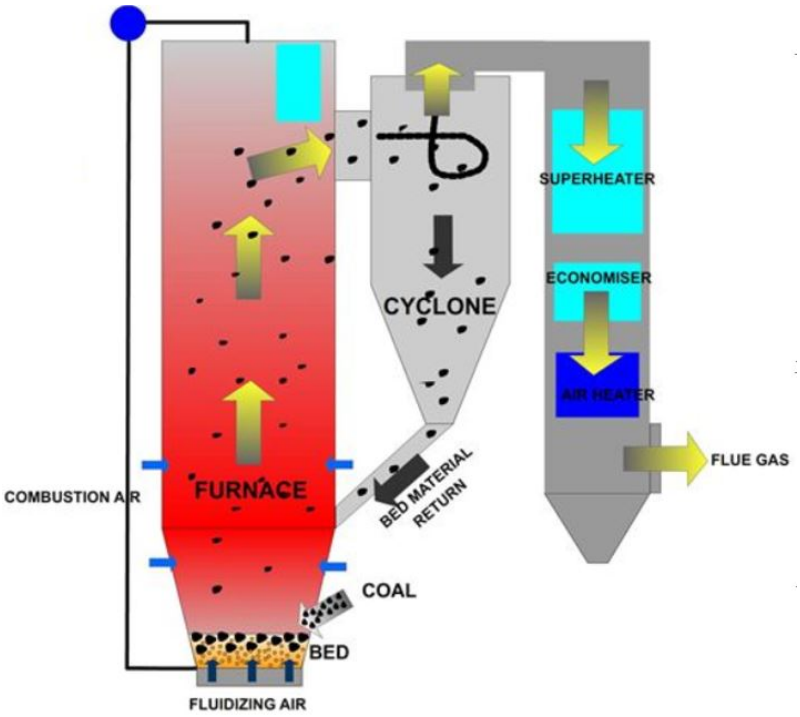

Figure 1: Typical configuration of a circulating fluidized bed [5].

2.1.1 Operating Regimes

When air gets introduced at low velocities it is most often evenly distributed across the bottom plate of the riser due to the pressure drop. The gas tends to take the path of least resistance and flow through the voids left by the solid particles. As the velocity increases the air starts to drag the particles until they are in a state of suspension. This is known as the minimal fluidization regime, which operates with a clear bed surface, small pressure variations inside the riser and limited particle movement. Further increasing the gas flow will eventually cause an onset of bubbling, also known as the bubbling regime, near the distributor plate. For visualization, see figure 2 (left). The bubbles gain size due to coalesce with other bubbles on their way to the bed surface, which causes pressure fluctuation. Increasing the velocity even further causes the bubbles to coalesce at greater extent, until they gain such size that they take up the majority of the riser's diameter. However, this is

only encountered in columns with small diameters. This is known as the slugging regime, see second column in figure 2. The bed surface rise and collapse at a regular frequency which leads to large pressure fluctuations. These regimes can be found in low velocity fluidized beds [6].

It can be beneficial to operate the bed with higher velocities. If the superficial gas velocity is high enough for solid particles to leave the riser it creates an opportunity for heat transfer and regeneration, which is the common operating conditions for circulating fluidized beds. Therefore, increasing the velocity eventually causes a transition from slugging flow to a fully turbulent regime with very small voids and particle clusters. The bed surface becomes hard to distinguish and only small pressure variations occur, see third column in figure 2. Beyond that there is the fast fluidization, with no distinguishable bed surface and significant solid entrainment out of the riser. However, only some of the material leaves the riser and some fall back down to the distribution plate. The fast upward stream usually comes with a low particle concentration in the centre and those particles that do not leave the riser gets pushed outwards towards the riser wall. This phenomena leads to a slower downward flow with higher particle concentration near the wall. These are the characteristics of the so called core-annular flow, see fourth column in figure 2. Since this comes with a reduced cross-section area for the upward flow, it would not be uncommon to measure velocities in the centre higher than the superficial gas velocity introduced at the bottom. Beyond the fast fluidization the pneumatic coneying regime may be found with a very dilute flow and no significant distinguishable concentration profile across the riser, see figure 2 (right)[6].

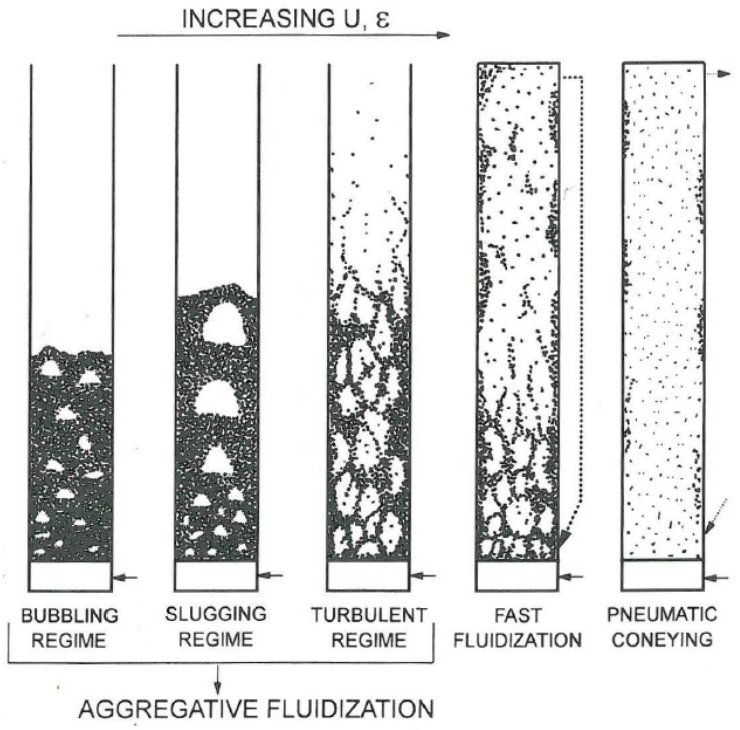

Figure 2: Operating flow regimes [6].

2.1.2 Particle size distribution

The particle size distribution may have various effects on the fluidization properties inside a CFB unit. This can be visualized by formulating a simple equation of motion for the particle based on Newtons second law, gravity force and stokes drag as seen in equation 1.

$$m\frac{\partial u_p}{\partial t} = mg - \frac{\rho_f}{2}A_p C_D |u_f - u_p|(u_f - u_p) \tag{1}$$

By dividing both sides in equation 1 with the mass and applying $m = \rho_p V_p$ creates the fraction $\frac{A_p}{V_p} = \frac{6}{d_p}$ in the drag term. Thus, increasing particle size decrease this fraction and therefore the drag force become less dominant, leading to a reduced particle velocity. This phenomena should cause small particles to be carried higher up in the riser compared to large particles, for superficial gas velocities larger than the minimal fluidization velocity. This is crucial when choosing bed material since two materials with the same density and same average particle size could lead to large differences in both concentration and velocity profiles depending on the size distribution. Wider distribution would carry the smaller particles further creating a more uniform concentration profile which is an important factor when designing any heat transfer surface. The wider size distribution might also increase the bulk

density since the smaller particles may fill the voids left by the larger ones creating a more dense packing.

Another phenomena which may occur in CFB risers that could be explained by the size distribution is the Transport Disengagement Height, TDH. This occurs at the height over the bed when difference in suspension density is negligible [6]. When the larger particles only gain enough momentum to travel a part of the riser height, before joining the outer down-flowing region, the smaller particles might gain sufficient momentum to leave the riser. This would create a height where there are no large particles to leave the up going stream creating a uniform suspension density.

2.2 Scale-up procedures

Circulating fluidized beds have previously been limited by their size in order to be commercially viable for utility boiler demands. In 1997 Yam. Y. Lee, author to chapter 11 in *Circulating Fluidised Beds* [6], claims that CFB boilers have seen a progressive up-scaling in both size and power output. However as Yam. Y Lee mentions, there is a need to further investigate local flow properties in fluidized beds in order to improve up-scaling predictions. This is not only necessary to more reliably increase the capacity of individual plants or to better transfer properties of experimental pilot plants to full scale plants, but also to improve predictions when changing bed materials. For cases with CLC technology the particles used are commonly oxides of different metal alloys which not only can have different size distributions but, more acute, different densities. In fact, Paul Cho investigates twelve different oxygen carriers with densities varying from 4.5 to 9.0 kg/dm^3, in *Development and Characterisation of Oxygen-Carrier Materials for Chemical-Looping Combustion* [7].

2.2.1 Predictive relations

One method would be to use scaling relations to predict the fluidization properties. Glicksman [8] proposed in 1993 the use of simplified relations for scaling different CFB models. Three cold and one hot model were studied and the results from different flow regimes compared. Glicksman used a set of unit-less quantities which are able to describe the characteristics of a CFB unit, see table 1. Here, the parameters that need to be similar according to the simplified Glicksman scaling laws are printed in bold.

Table 1: Dimensionless groups

Parameter	Equation
Froude number, Fr	$\frac{u_0^2}{gL}$
Density ratio	$\frac{\rho_p}{\rho_f}$
Diameter ratio	$\frac{D_{bed}}{d_p}$
Velocity ratio	$\frac{u_0}{u_m f}$
Reynolds number, Re_p	$\frac{\rho_f u_0 d_p}{\mu_f}$,
Archimedes number, Ar	$\frac{d_p^3 \rho_f (\rho_p - \rho_f) g}{\mu_f^2}$

All parameters in the above equations are taken from the experimental conditions except the minimum fluidization velocity u_{mf} that can be calculated according to equation 2 [8].

$$u_{mf} = \frac{\rho_p g (1 - \epsilon_{mf})}{[150 \frac{(1-\epsilon_{mf})^2}{\epsilon_{mf}^3} \frac{\mu_f}{(\phi d_p)^2}]} \tag{2}$$

In the equation above, void fraction of particles in minimum fluidization conditions, ϵ_{mf}, can be assumed to be slightly higher than the void fraction in fixed bed state.

For example when the length scale of the bed is reduced, the superficial gas velocity must be reduced in order to maintain a constant Froude number. Since the minimum fluidization velocity, u_{mf}, depends on the particle size, the size distribution must be altered in order to maintain the velocity ratio. Beyond the set of equations, the scaling relationships also require beds to be geometrically similar, have identical dimensionless particle size distribution and sphericity.

Glicksman [8] mentioned that for low Reynolds numbers ($\mathrm{Re}_p < 8$), it is not necessary to match the gas to solid ratio and particle to bed diameter ratio. This indicates that it is possible to study the effect of particle size distribution in the viscous limit region without interference of material density.

2.2.2 Cold Flow Model

The CFB to be evaluated in this paper is a cold flow model, scaled 0.36:1 to the 1 MW_{th} hot CFB found at Darmstadt Technical University, Germany. The scaled CFB operates at a somewhat elevated room temperature, with a maximum measured value below 43 $^{\circ}C$. The internal riser diameter is 213 mm and the total height extends to almost 3.1 meters, with twelve measurement ports at each side and three in the middle, see figure 3.

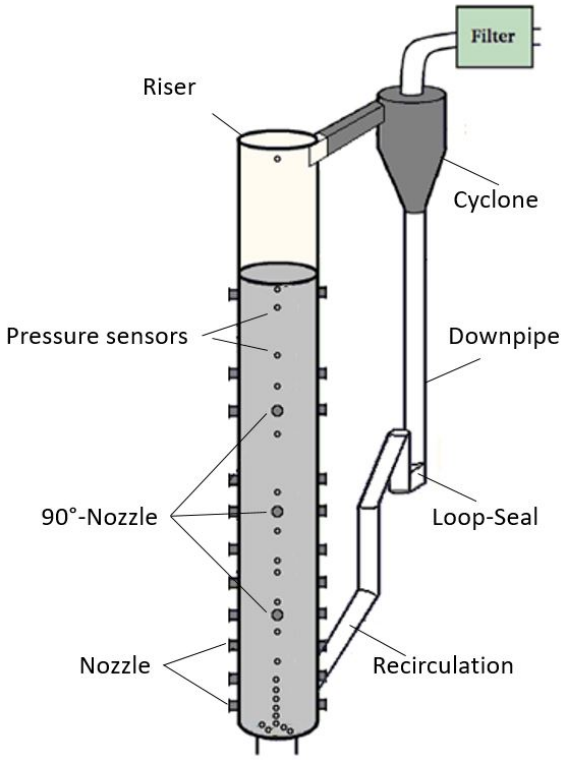

Figure 3: Scaled cold flow CFM200 model, Simon (2016), Darmstadt.

The cold flow model provides a simple measurement plant, easy to access, for evaluating local internal flow characteristics. Due to the low operating temperature, information regarding heat transfer is lost. Instead it allows testing of a wider range of bed materials. The lack of fuel provides an environment of clean particles, void of pollution that might have been introduced by fuel. This eliminates the aspect of soot formation and reduces the risk of particle agglomeration, which can not only interfere with fluidization of the bed but may also inhibit detailed measurements by interfering with the equipment.

Glicksman [8] indicates that the characteristics of the cold flow model still are applicable to the full sized plants regarding the flow hydrodynamics. Even though the flow is not necessarily identical it is preferable to build cold flow models due to their simplicity in comparison to active CFB boilers.

Nevertheless, the up-scaling process does not come without problems. Other than flow hydrodynamics inside the riser and heat transfer surfaces or cyclone efficiency.

2.2.3 Comparison to large pilot

Due to the important scale-up issues in fluidized bed research and vast uncertainties regarding the complex flow structures inside the bed system, it is of high interest to

compare different sized models [6]. One way of doing this is to compare in-bed flow pattern measurements within the 1 MW_{th} pilot plant at TU Darmstadt with the scaled cold flow measurements which has been the focus of this study. In order to compare these results the particle velocity profiles, gathered in the cold flow model, were "re-scaled" according to the Froude number, equation 3.

$$u_{solids,CFM\,re-saled} = u_{solids,CFM\,measured} * \sqrt{\frac{r_{CFB600}}{r_{CFM200}}} \tag{3}$$

The configuration of both models can be seen in figure 4 where the geometrical similarities are listed in table 2.

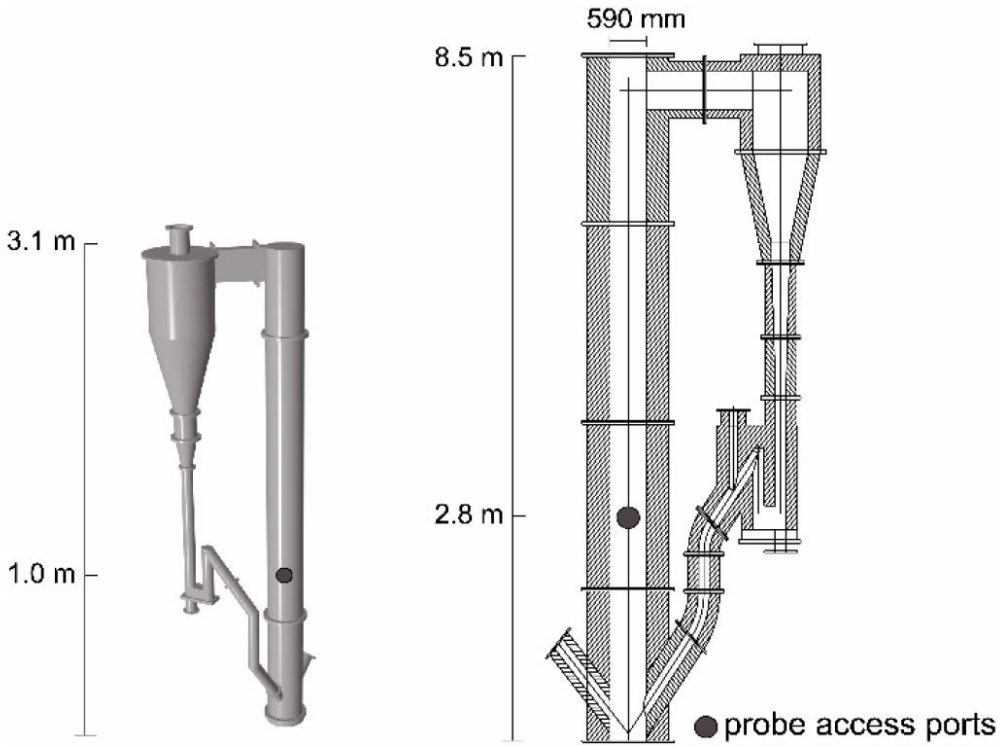

Figure 4: Fluidized bed test rigs. CFM200 (left) and CFB600 (right). Daikeler (2018), Darmstadt.

Table 2: Design parameters for hot and cold circulating fluidized bed reactors.

Parameter	**Unit**	**CFB600**	**CFM200**
Reactor diameter	[mm]	590	213
Reactor height	[m]	8.5	3.1
Material	[-]	Refractory lining	Stainless steel

The hot plant uses standard equipment of typical industrial CFB reactors like bag filters, heat exchangers and thermocouples etcetera. This plant is used as a test rig

for investigations of several different processes in a semi-industrial scale. These include carbon capture processes like gasification [9], chemical looping [10], carbonate looping [11] and combustion tests. The results presented in this paper were collected during a long-term carbonate looping test campaign in the CFB600 in early 2016.

In order to compare the hot and cold results it is essential to scale the operating conditions. For example, by keeping the Froude number constant it might be possible to obtain the scaled superficial gas velocities [8]. It is also possible to scale the inventory amount by keeping the height of the fixed bed constant. Finally, the flow structures for the different particle size distributions inside the cold flow model are compared to the hot pilot plant, thus enabling the determination of systematic differences, which are caused due to different particle characteristics.

2.3 Computational Fluid Dynamics

One field that has seen major improvements over the years, not only in accuracy but also in availability due to increased computational power, is the field of computational fluid dynamics, CFD. The concept of CFD is to divide a system into manageable blocks and then solve the governing equations, such as mass-, momentum- and heat transfer, related to the current system within each block. This concept is applicable to a wide range of systems, including CFBs, and is often used for predictive modelling. CFD simulations are often desired since it is usually cheaper, both economically and time-wise, compared to building and testing a scaled model. However this method would still need verification to ensure that the solutions are reliable. In 2014 Xingying Lan et al. [12] published a paper using CFD, or computational particle fluid dynamics (CPFD), to investigate the effect of polydisperse particle size distributions, PSD, on the fluid dynamics of the CFB. They used an Eularian-Lagrangian formulation with particles described as parcels.

Xingying Lan et al. first performed CFD simulations of monodisperse PSD and compared it to monodisperse experimental data of the same PSD. The simulation was able to reproduce the characteristic core-annular flow for CFB. The difference was that the simulation predicted a slightly lower velocity and higher concentration for the core flow. After the simulations were verified, they continued by introducing different size distributions, namely Gaussian and Lognormal PSD. The results indicated that the lower region of the riser is severely affected by the change in PSD. One of them being that the particle concentration in the lower region was significantly lower for wider PSDs. Information like this is important since most of the heat- and mass transfer occurs in this area. Also the residence time was altered, which has an impact on catalytic reactions in FCC reactors for example. However no verification was done for this simulation or the accuracy of the prediction which would be needed to strengthen the validity of the simulation.

2.4 Electric Charges & Antistatics

Frequent and intense collisions of particles with vessel walls and each other is, by nature, continuously present during fluidization of solid particles. These collisions are known to be the origin of something called tribo-electrification in fluidized beds, whose relevance depends on the operating conditions. Two main differences is charge transfer or charge separation between particles and a surface. The first when two surfaces come into contact, allowing a charge to flow from one surface to another, resulting in similar surface polarities. The second one, also known as bipolar charging, causing surfaces to acquire opposite polarities upon contact. For electrostatic-phenomena such as wall fouling and agglomeration in cold fluidized bed systems, the bipolar charging is of high importance.

The electrostatic charges on vessel walls and particles can, beside the contribution of high-voltage electrical fields, interfere with sensors, affect the motion of fluids and particles and might also lead to malfunction of operations and instruments [13].

The electrostatics are most likely to be relevant for relatively small particles, high superficial gas velocities, low temperatures and high surface-area-to-reactor-volume ratio. It is also important when the dielectric constants of the particles are of intermediate magnitude ($\varepsilon_p > 2$) since this imply gaining and retaining of electrical charges [13]. All of these factors would need to be considered, more or less, in this study.

The intensity, frequency and probability that particles collide with walls or other particles are related to the hydrodynamic characteristics of fluidized beds. However, when the magnitude of electrostatic forces are comparable to hydrodynamic forces, they are likely to affect the particle motions and therefore also the hydrodynamics of the entire bed. Generally, for the bubbling or turbulent regimes, the degree of electrification increase with increasing superficial gas velocity [13]. Where particle-wall interactions dominate the tribo-charging, as it does in the slugging flow regime, an increase in superficial gas velocity can in fact reduce the degree of electrification.

Charged particles tend to increase the minimum fluidization velocity, u_{mf}, affecting the flow properties. Thus, electrostatic forces not only decrease the solids mixing and lead to less vigorous fluidization but may also cause wall sheeting and particle agglomeration. Obstructing the flow properties causes a reduction in solids entrainment. Fotovat et al. [13] demonstrated that both column wall material and particle conductivity have large impact on entrainment due to their effects on the electrostatic charging.

2.4.1 Electrostatic control

The charge generation rate can be reduced by reducing the contact between bed material and walls. This can be achieved by, for example, coating or treating the

inner walls of the reactor or decreasing the contact surface area. F. Fotovat et al. [13] displayed in several experiments that particle charge-to mass ratio increases with decreasing mean particle size. However, if fine particles are added to a bed of coarse granulates they can affect the generation, transfer and neutralization of electrostatic charges and reduce the electrostatic potential of the bed. This is illustrated by Yu et al. [14], who claim that fine particles tend to adhere surfaces of opposite polarity and thereby reduce the contact between coarse particles and walls but also the contact between the coarse particles themselves.

Loss of charges due to the particles surface conduction is the main mechanism of charge dissipation. When particle surface conductivity is increased it evidently leads to enhanced charge dissipation. In this regard, methods like adding hygroscopic (highly water-adsorbent) materials such as Larostat 519, a few ppm of water or conductive fine particles to charged particles in fluidized beds has shown to be successful [13]. Wiesendorf [15] states that another possible way to avoid electrostatic charging can be by adding 1 wt% salt (NaCl) to the bed material.

2.5 Scanning electron microscope

The flow hydrodynamics depends on the shape of the particles used as bed material in the CFB unit. In order to examine the sphericity and surface elements of the particles used in this paper, a Scanning Electron Microscope (SEM) with energy dispersive x-ray (EDX) is used. The SEM produces images of the particles by scanning their surface with a focused beam of electrons. Atoms in the scanned sample interact with the incoming electrons and produce mainly three signals, back-scattered electrons, secondary electrons and element characteristic x-ray. The secondary electrons are used to generate a topographical image of the sample and the characteristic x-ray are used to suggest the present elements.[16][17]

2.6 Measurement Techniques

When studying the flow hydrodynamics inside CFB systems, properties like local solid concentration, mass flux and local velocities are often of interest. This data is used to further improve the knowledge and precision of scale-up processes and serve as CFD validation. There are a few techniques which allows such measurements. These may be categorized as invasive and non-invasive procedures.

2.6.1 Non-invasive methods

Non invasive procedures are preferred whenever possible since they do not interfere with the flow structure inside the measured bed. A non invasive method which is currently common in monitoring fluidized beds are pressure sensors. Since the solids are held in a state of suspension it is possible to relate the change in relative pressure to the amount of solid material. This may be used in order to keep track

of the inventory of the fluidized bed. However, in the case of a circulating fluidized bed it is not as easily implemented due to presence of the loop seal, which cause non-constant pressure profiles close to the distributor plate. Therefore, this method is not reliable when estimating the solid concentration in the lower region of the riser. However it may still be indicative to inventory with regard to the pressure drop of the entire riser over the measurements.

Tomography is another non-invasive method to investigate the local flow characteristics inside a CFB. Gamma (γ) ray tomography have been used already in 1957 by Bartolomew and Casagrande [18] to measure the density and density change on opaque materials inside fluidized beds. The measured intensity of γ-radiation is related to the radiation intensity, equipment geometry, alignment of the source and detector, the composition and amount of the material between the sensor and source. One major advantage with this method is that it does not require much preparation work and can be implemented on most active industrial fluidized beds. However the γ-radiation poses a health risk for those in its vicinity which causes this method to be unattractive.

Another method which has been applied for fluidized beds are fibre optics. However such methods can only measure the flow structure in the outer region unless they are made to be invasive. These kind of probes are limited by the optical transparency and may thus not penetrate far into the flow structures while remaining non-invasive. Having multiple intersecting optical beams, one source and one detector, Ulrich & Hamann [19], were able to relate the intensity of the scattered light to the aspect ratio of the encountered particles in the primary cyclone of the CFB unit. However due to the limited penetration it would not allow for local flow and concentration measurements.

2.6.2 Invasive methods

In order to accurately measure local flow concentrations and velocities within a fluidized bed, some invasive measurements may be required. Werther et al. [20] compared a Laser Doppler Anemometer, LDA, to a single fibre reflection probe, SFR, for measurements in a cold CFB model. The LDA system uses a similar system, as previously discussed, with one source and one optical sensor mounted on a probe. With this construction it is possible to measure the local flow characteristics within a fluidized bed. The other tested equipment is the single fibre reflection, SFR, construction. It uses fibre optics to transmit a beam into the fluidized bed and transmitting the reflected signal back, through the same fibre. The signal is then split and evaluated. One difference between the two is that the measuring volume for SFR is directly in front of the fibre while the LDA measures at a set distance of 19 mm. In comparison, the later might reduce the flow disturbance from the probe. However in dense regions the signal from the LDA may not be able to reach the detector and thus go blind where the SFR should still operate perfectly. Because of that the measurements were performed in the upper dilute zone of the

riser in order to get comparable results. Werther et al. came to the conclusion that the data acquired for the two different equipment's were equally valid. Thus suggesting that having the measurement volume close to the probe does not have any major effect on the flow characteristics, if the equipment is made small enough.

What seems to be the biggest issue with optical measurements is that if there are some particle deposition on the sensor, the equipment will go blind. This effect may be more pronounced in the upper dilute zone of the raiser where fine ash particles may be found without high particle concentrations to act like scrubbing agents. However, since this study is for a cold CFB model using glass particles, there will be no fine ash particles to disturb the measurements.

Other probe systems have been developed such as the suction probe, tested by Rhodes & Laussmann [21]. The suction probe is constructed like a L-bent pipe which is rotatable and thereby enabling measurements for both upwards and down-flowing mass entrainment. A problem with this technique is the influence of the suction velocity. When it is too high or low, the mass entrainment will be overestimated or underestimated respectively.

Another tested concept is the impeller probe developed by Grief and Muschelknautz [19]. The concept is often used by impeller anemometers to measure the local wind or air velocity but now adapted to CFB applications. The concept is that the angular velocity of the anemometer is proportional to the local gas/particle velocity. This probe was adapted with internal cooling for measurements inside a real, hot CFB model. The critical part of the device is the bearing supporting the impeller. Since friction or any other resistance caused by fine particles inside the CFB would interfere with measurements. This probe type could be combined with the previous suction probe to gain both local mass flux and velocity. The impeller probe might also serve to help determine the appropriate suction velocity of the suction probe to increase its accuracy.

The last probe covered in this study is the capacitance probe. Capacitance can be explained as the ratio of change in charge in one conductor induced by a change in an opposing, separate conductor. The rate of change in the sensor conductor in the probe system is related to the dielectric constant of the medium between the conductors. This relates the measured signal to the local volume concentration of particles inside the measurement volume, since the dielectric constant of air is practically negligible. Through proper calibration this device have been able to measure local solids concentration and, through a multiple probe system together with a cross correlation technique, also local particle velocities in both dense and dilute gas-solids flow by [15], [22]. This device allows to measure the sought for local quantities but should also be able to detect the presence of gas bubbles, which is indicative in to what flow regime the CFB is currently operating. This is necessary since different particle size distributions should change the required velocities to operate under different regimes. However, one may not forget the spiteful possibility of electric charges carried by, for example, glass particles. Since the responding change

of the conductor is the measured quantity; performing measurements in electrically charged beds may influence the measurements immensely.

The two most attractive options presented here are, in the opinion of the writers of this thesis, the SFR and the capacitance probe system. They both operate similarly, acquire similar types of data and could be made small enough to reduce the impact of the invasive measurements. For this study the capacitance probe will be used since the system has already been developed an tested at the Technische Universität Darmstadt, Germany [22]. One advantage of the capacitance probe is that for minor deposition the signal disturbance could be treated as an offset under evaluation. This advantage also comes with a loss of the possibility of local imaging using optical methods.

2.6.3 Construction & dielectric constant

The capacitance probe measurement device used in this study is constructed according to figure 5. The device can be fixed to one of the nozzles on the riser, allowing the probe head to be moved in radial direction while conducting in-bed measurements.

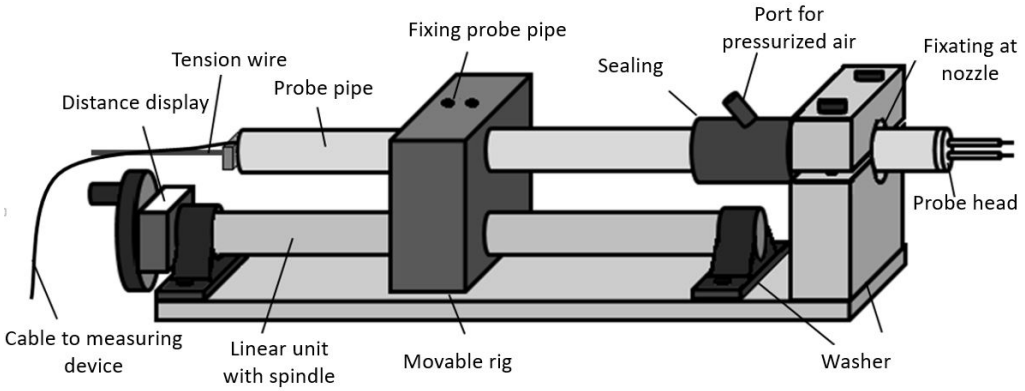

Figure 5: Capacitance probe construction, Jakob (2016), Darmstadt.

The data acquisition of this system is explained in the schematic figure 6. A preamplifier module is used to connect the two probes to a commercially available signal processing unit (Micro-Epsilon Messtechnik GmbH & Co. KG, Germany). Each measurement point is averaged over 500,000 values recorded at a frequency of 7812 Hz, during 64 seconds of measurement time.

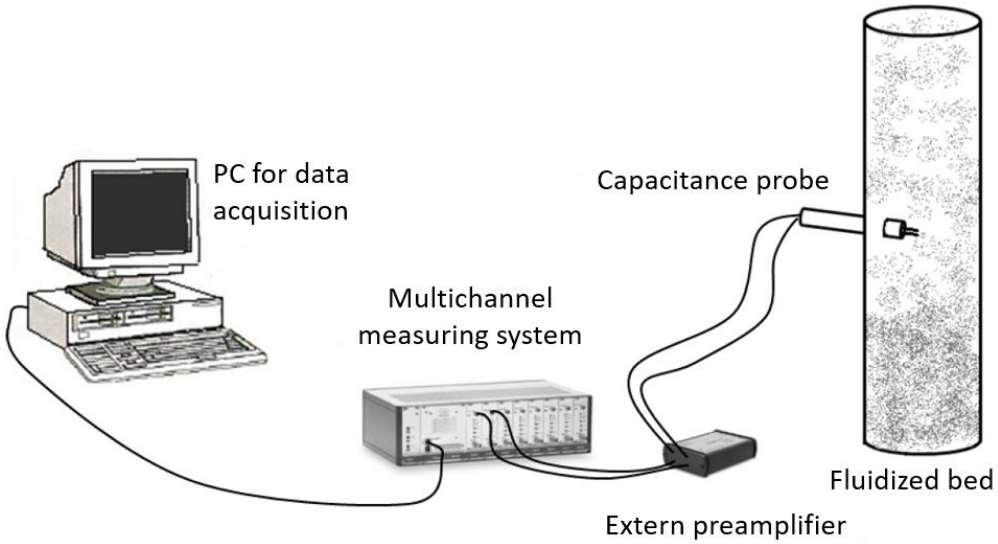

Figure 6: Data acquisition, Jakob (2016), Darmstadt.

The probe is a needle type capacitance probe, depicted in figure 7, constructed with the central conductor extending further than the rest of the device. The needle is surrounded by a non-conductive ceramic material and a surrounding guard. This is inserted into another insulating ceramic rod and finally fitted inside the grounding conductor.

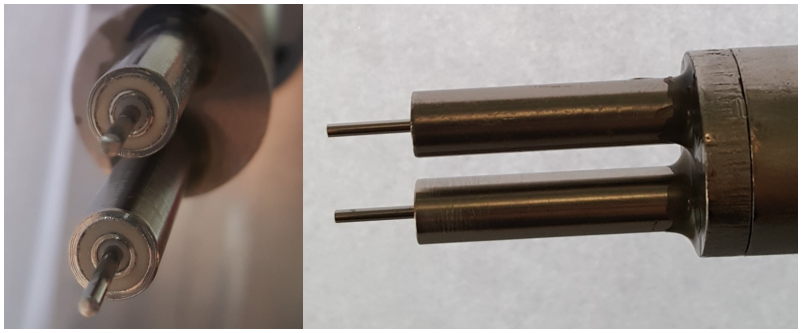

Figure 7: Needle type capacitance probe construction.

The guards purpose is to enable active shielding to suppress any stray capacitance from the wire by applying the same current to the guard as to the sensor. This, to exclusively detect capacity changes within the measurement volume and thus allows the detected output voltage to be directly correlated to the dielectric constant of the suspension located within the sensor volume [15]. Where the dielectric constant K_e of the gas-solids suspension may be visualized as the materials ability to store electrical energy in an electric field. The dielectric constant of the suspension within the sensor volume can be calculated by observing the induced voltage in the ground conductor. Wiesendorf & Werther [15] suggests the following formula for evaluating

the dielectric constant of a suspension within the control volume of the probes:

$$K_e = \frac{U_{ref} - U_0}{U_{ref} - U} \tag{4}$$

Where U_{ref} is the reference applied AC current, U_0 is the base voltage signal measured in solids-free atmosphere and U is the signal measured in the CFB reactor.

Therefore, by applying a current to the central conductor it establish an electrical field between it and the ground capacitor. The electrical field induces a net transport of electrons in the ground capacitor as a response to the current applied to the central conductor. The strength of the electrical field is related to the dielectric constant within the sensor volume which in turn can be connected to the surrounding solid volume concentration. The base capacitance is often determined in vacuum but due to the low dielectric constant of air (1.000264) [15] it can be determined in air without any major errors.

2.6.4 Calibration & Solid Volumetric concentration

With knowledge of the signal characteristics it becomes possible to associate it with specific conditions in order to determine the local volume concentrations. By measuring the dielectric constant for the suspension with a known concentration and the base dielectric constant without any solid particle interference, it is possible to estimate the local volumetric concentration of solid particles. Possibly the simplest concentration to measure would be in fixed bed where the concentration can be calculated with the particle apparent density and bulk density. However it is not necessarily the only state one can measure as a baseline. Since temperature has an impact on the relative dielectric constant of the solid suspension Wiesendorf & Werther [15] suggest that one should measure in a minimal fluidized bed state at operating temperatures instead. It is also important to have knowledge regarding temperature gradients, especially along the upper dilute zone of the riser, since it affects the relative dielectric constant. Since the temperature change due to friction in the cold CFB model is small it should not have any major impact on the measurements or the calibration.

Wiesendorf & Werther [15] also suggest an improved formula which is able to predict the volume concentration of both gas-solid suspensions but also liquid-solid suspensions for both high and low concentration zones, see equation 5.

$$c_v = c_{v,fb} \frac{K_e - K_f}{\Big(K_{e,fb} - K_f\Big(1 + \frac{(K_{e,fb} - K_e)(K_{e,fb} - \beta)}{K_{e,fb} K_f}\Big)\Big)} \tag{5}$$

The dielectric constant $K_{e,fb}$ is measured in a fixed bed state, K_f is the relative dielectric constant for the fluid and K_e is the one measured for the local suspension. All of these constants are calculated from the measured voltage, using equation 4. The parameter β is simply a design parameter chosen as 3 which allows the empirical relationship to fit both gas and liquid systems [15].

2.6.5 Velocity & mass flux calculations

Due to the inherent instability of homogeneous particle suspension the particles tends to form clusters [6]. These clusters result in a very clear signal for the capacitance probe and by using a dual probe setup one may calculate the velocity of the clusters through the signal temporal offset. The probes used have two sensors spaced 12 mm apart, centre to centre. Through cross correlation it is possible to determine the similar segments of the two signals and through the temporal offset between the two segments, together with the known sensor distance, calculate a local particle velocity[15]. The velocity is found by dividing the measurement data into intervals of 500 points and then cross correlating the two signals. Should the normalized cross correlation coefficient be larger than 0.8 they are deemed to have high correlation and are used to determine the velocity for that specific interval. The sample window is spaced to have a 50% overlap with the previous sample window in order to increase number of determined velocity estimation.

In addition to the cross correlation constraint, one may also include other ways of excluding false velocities. For example, if the riser is operated at a superficial gas velocity of 2 m/s it is highly unlikely that measurements of 15 m/s are reliable. Such measurements can be caused by disturbance or chance. One may then introduce an upper limit of what is an acceptable velocity. Should the majority of the readings be well below this limit it should not interfere with the actual measurements and thus be eliminated. The maximum and minimum detectable velocity is dependent on the sensor spacing, sample size window and measurement frequency as:

$$u_{min/max} = \frac{Probe\,spacing}{\left(\frac{Data\,shift}{Measurement\,frequency}\right)} = \frac{d}{\frac{n}{f}} \tag{6}$$

With the used setup yields the theoretically minimum detectable velocity 0.1875 m/s and a maximum detectable velocity of 93.75 m/s. With this current setup it should be possible to measure all relevant velocities occurring in the riser of the cold CFB model. It could be argued that the sample window should be increased to allow lower velocities to be measured. However, this may come at the cost of reliability of the cross correlation of the signals.

The mass flux can easily be calculated from the received concentration and the velocity. Either by integrating over the two profiles to achieve a net mass flux or by using individual measurement points to estimate the local mass flux. The later may also be integrated to achieve a net flux. Wiesendorf proposed [23] calculation of the time averaged mass flux using equation 7.

$$G_{s,l} = \rho_p \bar{c_v} \bar{v_j} \tag{7}$$

Where ρ_p refers to the material density, c_v and v is the determined volumetric concentration and velocity respectively.

2.6.6 Signal instability

During measurements there may be some factors which greatly affect the signal and thus create unreliable results. For example, when doing measurements close to the wall it is apparent that the wall might have some effect on the measured voltage and thus require a different type of evaluation. If the measurement is compared to the previous determined base signal, then being in the proximity of the wall can result in a concentration much larger than what is actually encountered. What can be done is to establish a new base signal based on the 99 % quantile of the measured signal. The inverted measured signal which correspond to the 99% largest signal based on a cumulative distribution function, is chosen as the in situ base signal and thus including the presence of the riser wall or fine particle deposition on probe.

The unpleasant environment found in CFB units may cause the probe geometry to change over time, which is crucial in order to estimate reliable velocities. The alignment of the probe tips have to be checked regularly since it is constructed through fitting rather than adhesive. Luckily the low temperature variation of the equipment should reduce the risk of part rearranging through thermal expansion.

The two probes could both interfere with each others measurement through shielding. Should the local velocity be in an upwards direction the lower probe will interact with the particles and cause them to deviate from their trajectory. Thus the lower probe will affect the measurements done by the upper probe, and vice versa for downwards flow. This shielding effect is accounted for by weighing the concentration of the two probes according to the equation below.

$$c_{v,weighted} = \frac{u_+}{u_{all}} c_{v,p1} + \Big(1 - \frac{u_+}{u_{all}}\Big) c_{v,p2} \tag{8}$$

In equation 8 the indices p1 and p2 simply refers to the first and second probe. The u_+ would refer the number of determined positive velocities and u_{all} is the total determined velocities.

3 Methodology

The study was to investigate profiles of local particle concentrations and velocities for glass microbeads of different particle size distributions inside a scaled cold flow CFB model. The CFB were to be operated at different superficial gas velocities and the measurements was performed with a capacitance probe at different heights of its riser, according to table 3.

Table 3: Heights of the different measurement ports at the riser.

Measurement port	**P1**	**P2**	**P4**	**P7**	**P9**	**P11**
Height [mm]	124	248	496	992	1580	2262
Relative height [-]	0.04	0.08	0.16	0.32	0.51	0.73

Three superficial gas velocities of 1.9, 2.3 and 2.7 m/s were recommended beforehand as well as the positions for each measurement, as seen in table 4. The plan was to conduct measurements at six different left ports and for validation reasons, also three middle and one right port. Since the left and right ports are concentrically aligned it should be sufficient to only conduct measurements at one of the superficial gas velocities in the right port. The original plan was to do tests at two different (100-200 μm and 200-300 μm) particle size distributions. Some measurement ports, superficial gas velocities and number of studied PSDs later came to change.

Table 4: Measurement template for the capacitance probe

Measurement port	**L1**	**L2**	**L4**	**L7**	**L9**
Height [mm]	124	248	496	992	1580
h/H [-]	0.04	0.08	0.16	0.32	0.51
Measurement port	**L11**	**M4**	**M7**	**M9**	**R4**
Height [mm]	2262	496	992	1580	496
h/H [-]	0.73	0.16	0.32	0.51	0.16

Before any measurements could take place, the cold flow CFB reactor was emptied of old material and all ports were provided with new sealing to prevent leakage. After some preliminary tests it was concluded that the reactor had to be upgraded with a new particle mesh at the distribution plate in the bottom of the riser and the fresh air filter after the cyclone needed to be cleaned.

A capacitance probe system was built and provided by the supervisor. The probe position inside the 213 mm wide riser is adjusted with a scale of 0.1 mm precision. For a visualization of the probe and scale device mounted on the riser, see figure 8. For the evaluation procedure to be trustworthy the two probe sensors have to be vertically aligned which was controlled at regular intervals between the experiments.

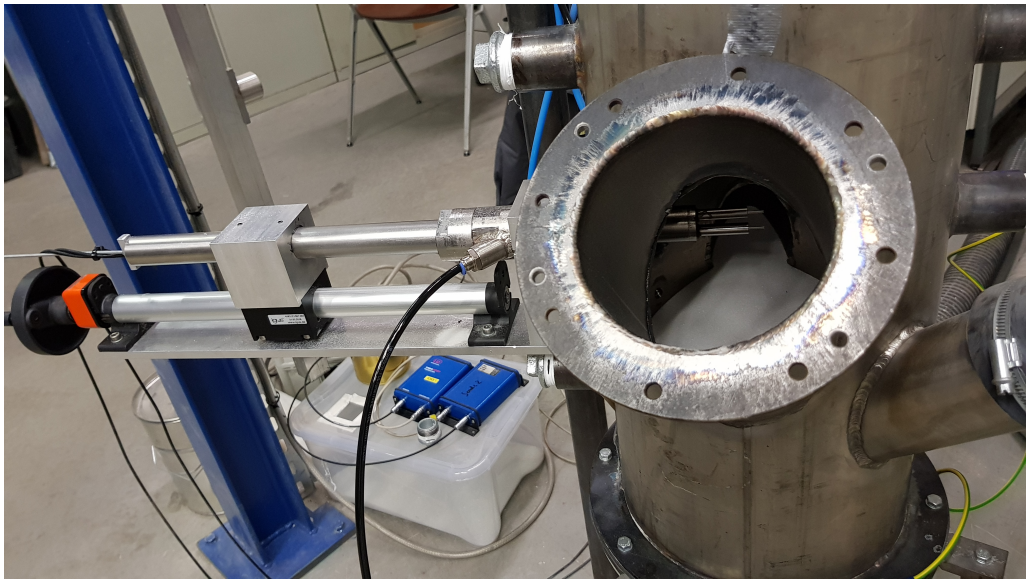

Figure 8: The mounted probe rig in the CFB model.

The first in-bed measurements were collected at 54 locations, which were chosen to be dense in near wall regions and with larger increments near the center of the riser. When evaluating the results from the 54 measurement points it was clear that 38 points should be sufficient to provide feasible results. These 38 points were therefore used as template for the upcoming measurements.

3.1 Material properties

The glass microbeads were purchased from Worf Glaskugeln with particle size distributions of; 70-110, 100-200 and 200-300 μm. Since the larger particles are less prone to interfere with measurements, those two have higher priority.

Before evaluating each measurement some material properties had to be gathered. Values of bulk densities, material densities and dielectric constants for each material were needed. These were also measured after usage to check for material consistency and thus ensure trustworthy results in that aspect. For validation reasons, particle size distributions and pressure profiles were continuously measured.

3.1.1 Bulk density

The material bulk density was measured using a funnel type contraption which allowed the glass particles to settle naturally and consistently into a container of known volume and weight. The container was leveled, weighed and the procedure was repeated five times yielding an averaged bulk density.

3.1.2 Material density

Material density was measured with a pycnometer according to ISO 1183:2012 method. The procedure was to first measuring the weight of the empty pycnometer m_0, on a scale with one hundreds of a gram precision, then adding and weighing 10-30 grams of the solids m_2. The solids were soaked and the pycnometer filled with distilled water before measuring a new weight, m_1. Lastly the pycnometer, emptied of solids and filled with distilled water, was weighed one last time, m_3. Thereby, by using the water density, the solids density were calculated according to equation:

$$\rho_s = \frac{m_2 - m_0}{(m_1 - m_0) - (m_3 - m_2)}\rho_l \tag{9}$$

For trustworthy results the procedure was repeated three times and the final density averaged between these. The water temperature was measured each time and the water density updated if needed. The pycnometer volume was calculated by;

$$V_p = \frac{m_1 - m_0}{\rho_l} \tag{10}$$

This value was compared with the known pycnometer volume and the deviation gave a number on the validity.

3.1.3 Dielectric constant

The signal intensity was first measured in air to establish its base capacitance. Later the capacitance probe was submerged in a fixed bed state using the same method when determining particle bulk density. The signal was recorded and the dielectric constant in fixed bed state was determined according to equation 4 in chapter 2.6.3.

3.1.4 Particle sieving

The particle size distributions were measured with an air jet sieve analysis. The sieving was done by weighing 50 grams of material on the finest sieve for the selected sequence. The sieve was then placed in a machine with a particle collection cyclone and air introduced to disturb the particles. The air pressure was set to 2000 Pa and the sieving continued for 120 seconds. When completed, the remains were weighed on a scale with one hundreds of a gram precision and the procedure was repeated for the remaining sieves. The sieving interval was chosen to be around 50 μm outside the expected size distribution. Then every available sieve is chosen for the intervals. Between ≈50-250 μm for the 100-200 μm material.

3.2 Probe measurements

The larger particle size distributions are easiest to operate, but due to the scaling laws discussed in section 2.2.1, the smaller are of higher interest to the study. Together with the fact that old data of 100-200 μm PSD on different material was

available for comparison, led to the conclusion that the first material studied was of 100-200 μm PSD.

Before introducing inventory material, the riser, loop seal, cyclone and all measurement ports were completely emptied of old material. The reactor was operated empty for a few minutes, to flush out unreachable particles. It was then operated with four kilos of new material, to fill up the ports. The leftovers were removed and lastly a total of 11.2 kg material, 9 kg in the riser and 2.2 kg in the loop seal, was added. By loading material this way the inventory is very accurate, with only small deposition in the ports, and should contain very low amounts of previous material.

In the start, middle and end of every particle size distribution, the solid particle entrainment in the loop seal was measured at the used superficial gas velocities. This was done by temporarily turning off the fluidization gas in the loop seal, while simultaneously measuring the time it took for a specific amount of material to build up. This might be used to detect possible inventory losses, study the affect of particle size distribution and should conform with the calculated mass entrainment at the upper ports by the capacitance probe.

Each probe measurement began by noting the base signals from the centre of the non-operating CFB, to be used for later evaluation and to check for probe consistency between runs. The port number, date, PSD, superficial gas velocity and solid entrainment in the loop seal was registered in a protocol according to figure 22 in appendix 7, and a pressure profile along the CFB-unit recorded as the measurements began. All probe measurements can be seen in figure 28 in appendix 7.

3.2.1 100-200 μm particle size distribution

The measurement template in table 4 was upgraded for 100-200 μm PSD material. The left-port measurements were conducted as planned but three, instead of one, right ports were chosen for validation. Three middle ports were used with an additional superficial gas velocity of 1.5 m/s. All measurements for this material can be seen in table 5, where sections marked with "-" are excluded and the number of "X" correspond to the number of conducted measurements. The reruns were used as validation material to the original runs. The measurements that were conducted more than twice were mostly due to unexpected behaviours in the original runs. The probe measurements were continuously loaded into a provided MatLab code, together with the calibration measurements. The results were studied and validated before moving on.

Table 5: Probe measurements on material 100-200 μm. No measurements were conducted at sections marked with "-" and each "X" correspond to one profile measurement.

Measurement port		**L1**	**L2**	**L4**	**L7**	**L9**	**L11**
Height [mm]		124	248	496	992	1580	2262
h/H [-]		0.04	0.08	0.16	0.32	0.51	0.73
Superficial gas velocity [m/s]	**1.5**	-	-	-	-	-	-
	1.9	XX	XXXX	XX	X	X	X
	2.3	X	X	XX	X	X	X
	2.7	XXX	X	X	XX	X	X
Measurement port		**M4**	**M7**	**M9**	**R2**	**R4**	**R7**
Height [mm]		496	992	1580	248	496	992
h/H [-]		0.16	0.32	0.51	0.08	0.16	0.32
Superficial gas velocity [m/s]	**1.5**	X	X	X	-	-	-
	1.9	X	X	X	-	-	-
	2.3	X	X	X	XXX	XXX	X
	2.7	X	X	X	-	-	-

3.2.2 200-300 μm particle size distribution

The next material to be studied was that of 200-300 μm PSD due to its simplicity. This material was studied with similar procedures as described above. The ports, superficial gas velocities and reruns were according to table 6. The 1.5 m/s superficial gas velocity was only studied for port four and below, since there was no solid concentration in the regions above. That implied a non-existing solid particle entrainment for 1.5 m/s gas velocity.

Table 6: Probe measurements on material 200-300 μm. No measurements were conducted at sections marked with "-" and each "X" correspond to one profile measurement.

Measurement port		**L1**	**L2**	**L4**	**L7**	**L9**	**L11**
Height [mm]		124	248	496	992	1580	2262
h/H [-]		0.04	0.08	0.16	0.32	0.51	0.73
Superficial gas velocity [m/s]	**1.5**	X	X	-	-	-	-
	1.9	X	X	X	X	X	X
	2.3	X	XXX	XXX	X	X	X
	2.7	X	X	X	X	X	X
Measurement port		**M4**	**M7**	**M9**	**R2**	**R4**	**R7**
Height [mm]		496	992	1580	248	496	992
h/H [-]		0.16	0.32	0.51	0.08	0.16	0.32
Superficial gas velocity [m/s]	**1.5**	X	-	-	-	-	-
	1.9	X	X	X	-	-	-
	2.3	X	X	X	X	X	X
	2.7	X	X	X	-	-	-

3.2.3 70-110 μm particle size distribution

Lastly 70-110 μm PSD material came with substantial problems in regard to electrostatic charged particles. This was expected due to the operating conditions and is discussed in section 2.4. This interfered with the measurements in such extent that no trustworthy results could be generated. After a failed attempt to solve this problem with the antistatic agent Neostatic, another more successful attempt was performed with salt, NaCl. The procedure was to add 1 wt% salt, NaCl, to the material by solving salt in water before soaking the glass beads and later dry it in the riser. The salt content was later checked by dissolving the salt on 10g of coated particles in distilled water. They were later strained and rinsed through a 25 μm mesh. By evaporating the excess water the salt to particle mass ratio was attained.

The salt coating maintained the fluidization properties and by quick assessment the problem with electrostatics seemed to be solved. However, due to particle loss in the Neostatic attempt, new material with similar PSD was purchased from another distributor.

After calibration measurements on the new salt coated material, probe measurements as previously described were performed. However, due to excessive particle loss through the cyclone on high superficial gas velocities, the highest 2.7 m/s velocity was never operated. Measurements according to table 7 were conducted.

Table 7: Probe measurements on material 70-110 μm. No measurements were conducted at sections marked with "-" and each "X" correspond to one profile measurement.

Measurement port		**L1**	**L2**	**L4**	**L7**	**L9**	**L11**
Height [mm]		124	248	496	992	1580	2262
h/H [-]		0.04	0.08	0.16	0.32	0.51	0.73
Superficial gas velocity [m/s]	**1.5**	X	X	X	X	X	X
	1.9	X X	X	X X	X	X	X
	2.3	X	X	X	X	X	X
Measurement port		**M4**	**M7**	**M9**	**R2**	**R4**	**R7**
Height [mm]		496	992	1580	248	496	992
h/H [-]		0.16	0.32	0.51	0.08	0.16	0.32
Superficial gas velocity [m/s]	**1.5**	X	X	X	X	X	X
	1.9	X	X	X	-	-	-

3.2.4 100-200 μm particle size distribution, coarse mesh

The evaluated 100-200 μm PSD results were compared with old measurements from sand (limestone) particles of 100-350 μm (mean diameter $d_{p,32} = 193\,\mu m$ PSD) measured with same operation conditions. They displayed significant differences between the results, especially at the lower ports. However, at the time of sand particle measurements a coarse particle mesh was installed at the air distribution plate in the bottom of the riser. Therefore it was of interest to perform some control measurements with glass particles using the same, coarse, mesh in order to investigate its impact on the flow hydrodynamics. Probe measurements were gathered according to table 8.

Table 8: Probe measurements on material 100-200 μm with coarse mesh. Each "X" correspond to one profile measurement.

Measurement port		**L1**	**L2**	**L4**
Height [mm]		124	248	496
h/H [-]		0.04	0.08	0.16
Superficial gas velocity [m/s]	**1.9**	X	X	X
	2.7	X	X	X

3.3 Comparison to hot pilot

For the comparison between the hot 1 MW_{th} pilot plant and the cold flow reactor that was discussed in the theory some design parameters are presented in table 9. In this table an ideally scaled cold flow experimental model is presented in addition to the other conditions.

Table 9: Operating parameters for hot and cold CFB units.

Parameter	CFB600	Ideally	CFM200 glass beads		
Particle type	limestone	scaled	70-110	100-200	200-300
Superficial gas velocity [m/s]	3.5	2.1	1.5/1.9/2.3	1.9/2.3/2.7	
Temperature [°C]	650	30	30	30	30
Inventory riser [kg]	213	21	9	9	9
Particle density, ρ_p, [kg/m^3]	2672	7404	2504	2504	2504
Particle bulk density ρ_b, [kg/m^3]	1478	3067	1500	1448	1486
Particle diameter, $d_{p,32}$, [μm]	203	73	87	129	228
Dynamic gas viscosity, [10^{-6} Pas]	41.1	18.6	18.6	18.6	18.6
Gas density, ρ_g,[kg/m^3]	0.38	1.06	1.16	1.16	1.16

Dimensionless groups for the listed operation conditions are summarized in table 10. The bold face parameters represent those that need to be similar in order to fulfill the simplified Glicksman scaling laws [1] and the formulas for these numbers can be seen in chapter 2.2.1, table 1. Some parameters, such as density ratio, greatly deviates between the hot and cold units. This is to be expected since particle characteristics like diameter and density differs a lot. Not only between the two systems but also between the different sized glass beads, as seen in the table 10.

Table 10: Comparison of the dimensionless groups for hot, CFB600, and cold, CFM200, reactors.

Parameter	CFB600	CFM200 glass beads		
Particle type	limestone	70-110	100-200	200-300
Froude number, Fr	2.1	1.1/1.7/2.5	1.7/2.5/3.1	
Density ratio	6990	2170	2170	2170
Diameter ratio	2914	2448	1651	934
Velocity ratio	197	157/199/241	106/128/150	30/37/43
Reynolds number, Re$_p$	6.6	8/10/12	15/19/22	27/33/38
Archimedes number, Ar	49	54	176	975

For the scaling laws to be fulfilled, very small particles with high density ($d_{p,32} = 73.1\,\mu m$ and $\rho_p = 7404\,kg$ respectively), would need to be used. However, due to handling characteristics and toxicity for these kind materials they could not be

implemented. Nevertheless, the hot 1 MW_{th} pilot was operated in the viscous limit region with low particle Reynolds numbers ($Re_p < 10$), which might allow scaling of the particle size distribution alone and thus neglecting the particle densities [1], see chapter 2.2.1.

3.4 Evaluation & post processing

The conducted data from pressure sensors, capacitance probe measurements and calibration constants were continuously evaluated to create corresponding profiles. The capacitance probe measurements were evaluated with a provided MatLab code to produce excel files containing local particle concentration and velocity profiles etcetera. The corresponding pressure data were evaluated in Python, producing pressure profiles, temperature profiles and inventory approximations.

3.4.1 MatLab evaluation

Since the MatLab code for evaluating the raw data had already been developed, no major input in its functions will be given, but rather a short outline of its construction. The code was provided with geometrical data of the CFB unit and material properties of the glass particles. Each measurement point has their own .CSV document containing the 500,000 data points for both probe tips, collected over a minute. The name of the .CSV file refers to the probe location inside the CFB. The data was loaded and sorted by name of the measurement and evaluated using the techniques discussed in sections 2.6.3-2.6.6. Results of concentration, velocity and mass flux, among others, gets exported to an Excel template for evaluation. It is worth to notice that the concentration was evaluated twice, first using the base signal acquired from measuring in air and secondly using the 99% quantile from the measurement point itself. Both were needed since the former would estimate unlikely high concentration near walls, which is avoided using the 99% quantile. The latter might underestimate the concentration in the lower ports where the occasionally high concentration of particles makes it difficult to determine a suitable base signal.

3.4.2 Pressure profiles

The pressure was recorded at a rate of 1 Hz and mainly used to check the health of the CFB. The sensors, depicted in figure 9 were installed all along the riser, but also in the loop seal as well as air distribution and exit.

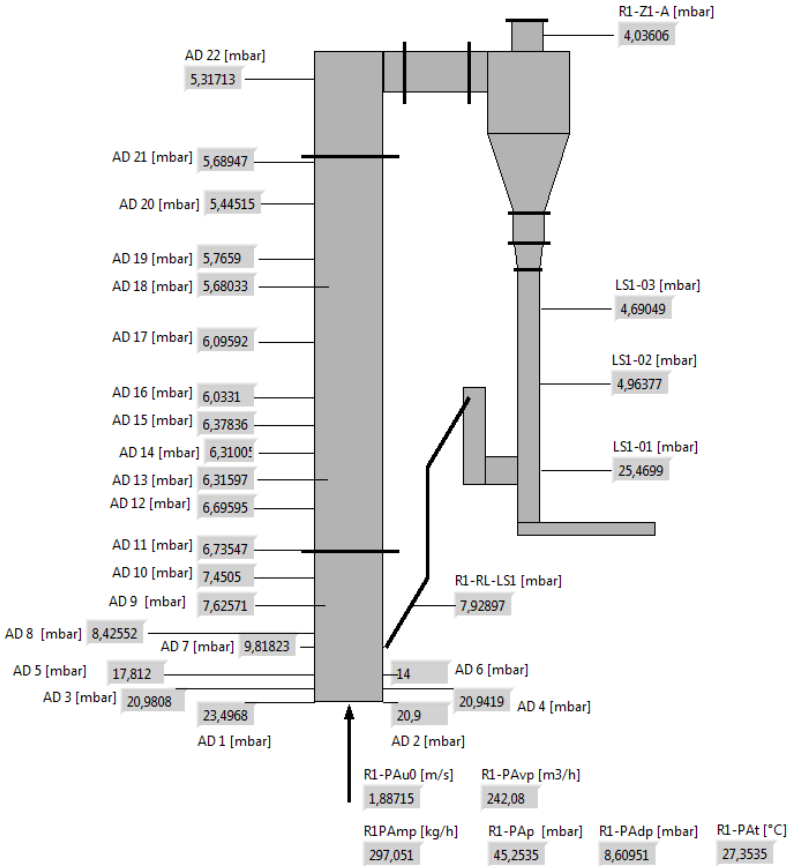

Figure 9: The CFB model with including pressure sensors.

The pressure was initially recorded near the air supply to determine its volumetric flow rate which, together with the riser dimensions, yielded the superficial gas velocity. It was also equipped with a thermocouple to get reliable air properties for the velocity calculation. Pressure sensors before and after the distribution plate indicated towards the cleanliness of the particle filter. The reactor was also equipped with a pressure sensor over the particle filter of the out-going air stream, which gave an indication to how much particles the cyclone failed to separate from the gas stream. The pressure data, containing around 4000x35 values, was evaluated using a self developed script in Python. Each profile was imported and the mean and standard deviation was calculated for each data type. They were sorted by date and plotted against each other in order to check for trends and operation consistency. By applying equation 11, suggested by [19], the data could be used to estimate the current inventory of the riser.

$$m_r \approx \frac{(p_d - p_c)A}{g} \tag{11}$$

Here m_r is the inventory of the riser, p_d is the pressure at the distribution plate and p_c is the pressure just before the cyclone, A is the cross-sectional area of the riser

and g the gravity constant. One alteration of this method was to collect a pressure profile of an empty riser and subtract that from the profile gathered during probe measurements. This method took the natural pressure gradient into account and thus evaluated only the pressure gradient caused by the particles. This method was henceforth referred to as the *modified* inventory approximation.

It was also developed to create a pressure based concentration profile, in order to illustrate the difference in information based on commonly applied industrial solutions to that of the capacitance probe. However, since the lowest measurement point was not located at relative height 0, the data was linearly extrapolated from the two lowest data points.

3.4.3 Electric charges

The signal from both probe tips was displayed in real time during data acquisition, but when electric discharges, seen as spikes, was observed the raw data was loaded into FlexPro to view data. Initially the discharges were few and of no concern to the integrity of the data but as the 70-110 μm particles were introduced it could not be overlooked. With the need to quantify the effect of electric discharges to evaluate the efficiency of the countermeasures, a Python script was developed. The script worked by importing and sorting the raw data of a measurement profile and counting the amount of points with signal intensities above 90 %. This, since the electric discharges caused intensity spikes in the signal, reaching up to 100 %, when the highest encountered signal else wise was the unobstructed base signal measured in air, with values around 84-85 %. Simultaneously the 99 % quantile was calculated. This allowed capturing the effect of electric discharges and agglomeration of particles on the probe from a declining quantile.

3.4.4 Scanning electron microscope

Since the shape of the particle is an important factor in flow hydrodynamics it is preferred to validate the shape of the particles used. Not only because one batch was supplied by a different supplier but the particles were coated which might have affected its shape. Therefore a scanning electron microscope (SEM) was used to analyze topographic image of the particles and energy-dispersive X-ray spectroscopy (EDX) for element identification on the particle surface. Results from the EDX are only presented in appendix 14 without detailed discussion in this study.

The particles were loaded on a pin using an adhesive, double sided, carbon based tape before being dusted of using compressed air as to not damage the equipment. After insertion into the SEM-EDX instrument a topographic image of the material was generated and a few points were chosen for element identification. Additional element mapping was chosen for some of the samples, showing concentrations and a rough map of the suggested elements location. The instrument was calibrated to the composition of carbon tape as to not interfere with measurements.

4 Results and discussion

Due to the vast amount of data procured during this work only parts of it can be displayed in this section. The focus will be laid on explaining the more condensed figures. The full set of data can be found in their respective appendix.

Testing of the two largest materials came with few setbacks with regard to either the CFB unit or the capacitance probe system. However, as described in section 2.4 and 3.2.3 the finest particle size distribution came with some electrostatic based difficulties.

4.1 Electrostatics

The electrostatic problems on 70-110 μm material were expected due to the operating conditions which were discussed in section 2.4. The bipolar charging affected the measurements with high wall fouling in the loop seal and on the probe sensors, see figure 10a. This phenomena was also noticed during the data acquisition where probe number one detected multiple electric discharges and the second probe fouling, see figure 10b. This interfered with the measurements in such extent that no trustworthy results could be generated.

(a) Capacitance probe with bipolar charging.

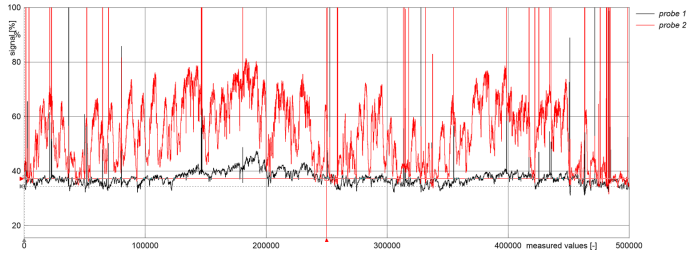

(b) Intensity signals from a capacitance probe system with two sensors.

Figure 10: Indications towards electrostatic effects.

Fotovat et al. [13] demonstrated that both column wall material and particle conductivity have a large impact on electrostatic charging. This could explain why wall fouling was so dominant in the loop seal. Since it was made out of plexiglas, which has low conductivity, it is prone to cause bipolar charging and then retain the charge.

While performing the literature studies some authors encountered similar problems and often used Larostat 519 to solve bipolar charging problem. However, it was considered to be toxic should it enter the lungs and the antistatic compound Neostatic was tested instead. However due to its seemed oily properties this compound caused severe agglomeration at concentrations of 0.91 wt% of active agent to glass particles. Even down towards 0.013 wt% this was noticed. Wiesendorf

& Werter [15] suggested to add 1 wt% salt instead and after the drying process about 0.4 wt% remained on the particles. This method eliminated about all of the noticeable electric discharges and after all tests about 0.3 wt% salt remained on the particles. The reason why it helps could either be that salt help negating the bipolar charging or that the salt inhibits the particle from retaining its charge while in contact with a grounded surface. When examining the particles in a SEM a few large crystals was seen in the unused particles, in figure 11b, which had either been redistributed or broken off while in the riser, as seen in figure 11c. However the success could be attributed to a combination of Neostatic and salt. Since the Neostatic covered glass particle could have coated the inside of the CFB during preliminary test runs, which could have an effect.

4.1.1 Salt coated particles

The finest material was coated with 1 wt% salt, NaCl, in order for the particles not to gain charge. After the drying process, a salt to glass ratio of 0.4 wt% were estimated to coat the particles and after approximately 40 operating hours inside the CFB 0.3 wt% salt remained. The particles were studied in an electron microscope, see figure 11.

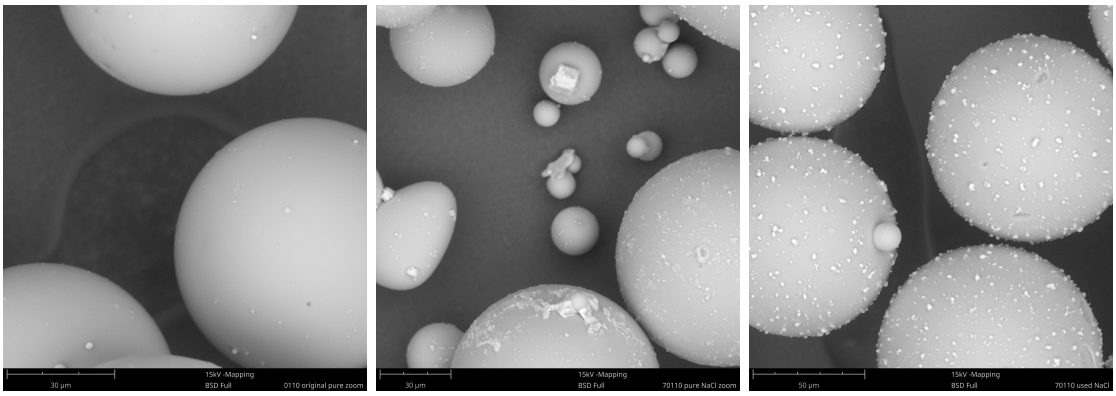

(a) Original material. (b) Salt coated. (c) Salt coated after CFB.

Figure 11: SEM images of 70-110 μm PSD material. Original clean material, salt coated material and salt coated material after 40 operating hours inside CFB model.

4.2 Material properties

After each material had been operated inside the CFB reactor it changed colour from white to grey, see figure 12. The color change may come from abrasion of metal in the riser or residue particles in the air supply. However, no clear changes in surface elements were found in the SEM element mapping process, as seen in appendix 14 tables 29, 30 and 31.

Figure 12: A cup of unused material placed in a container of used material.

It is seen that the material- and bulk densities are around 2500 kg/m^3 and 1480 kg/m^3 respectively, with slightly higher bulk density for the smaller material, see table 11.

Table 11: Density measurements on clean and used material.

Size distribution	**70-110**	**100-200**	**200-300**
Material density [kg/m^3]	2504	2504	2504
Bulk density clean [kg/m^3]	1472.23	1447.19	1486.17
Bulk density clean with salt [kg/m^3]	1486.24	-	-
Bulk density used [kg/m^3]	1514.30	1476.56	1468.76

The dielectric constants for both probe sensors can be seen in table 12.

Table 12: Dielectric constants for both probes on clean material and used material.

Size distribution	**Clean material**		**Used material**	
	Probe 1	**Probe 2**	**Probe 1**	**Probe 2**
70-110	3.400	3.423	3.401	3.432
100-200	3.305	3.389	3.418	3.413
200-300	3.401	3.422	3.312	3.351

The small difference in bulk density between the materials, see table 11, may be attributed to the width of the PSD. Since a wider PSD have smaller particles present which may fill the voids left by the larger ones allowing for a more dense packing. The change in dielectric constant between the materials could be attributed to the difference in bulk density. The lowest bulk density tends to lead to the lower dielectric constant and vice versa. This could be explained by the denser packing providing less room for air which has a lower dielectric constant. The change before

and after use could be accredited to the change in bulk density as displayed in table 11. Both the 70-110 and 100-200 μm PSD showed an increase in bulk density and also an increase in fixed bed dielectric constant. While the 200-300 μm PSD displayed a decrease in bulk density so did the dielectric constant as can be seen in table 12. Other factors which may affect the dielectric constant is discoloration, figure 12. This is believed to be metal shavings worn down from the riser walls during the rough conditions found in the CFB or residue particle from the air supply. However, as mentioned above, no such elements were found in the element analysis performed in the SEM. The addition of, possibly, steel and, in the case of the salt covered 70-110 μm, loss of salt could also be the cause of some change.

The mean sauter diameters, $d_{p,32}$, calculated from sieve analysis, are 87, 129 and 228 μm for the three different particle size distributions. A representative histogram of the change in particle size distribution before and after CFB usage is depicted in figure 13. The figure belongs to the 100-200 μm test series with the un-used material in blue and used material in a light orange color, thus creating a deep purple color where they overlap.

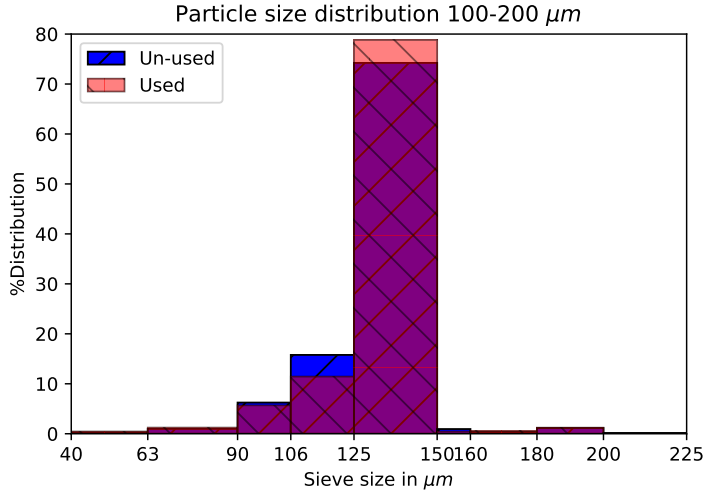

Figure 13: Histogram showing sieving results for used and unused material.

No major difference in size distribution prior to- and post testing was noticed, indicating towards consistency in that regard, see size histograms in appendix 6. The minor differences could be cause by inapt ability of the cyclone to recirculate the small particles at higher velocities, or uneven size distribution in the samples. Though the variations are so small they should not affect the data.

For detailed information about all size distributions, measured solid particle entrainments in the loop seal etcetera, see appendix 6.

4.3 Pressure related results

The acquired pressure data was compiled, averaged and plotted with change in relative pressure to the measuring height as can be seen in figure 14. This was done for all particle sizes and superficial gas velocities separately and can be found in appendix 13. The figure below showing results gathered in the beginning, middle and end of a test period in the CFB with a superficial gas velocity of 1.9 m/s and particle size distributions 70-110 μm, left, and 100-200 μm, right.

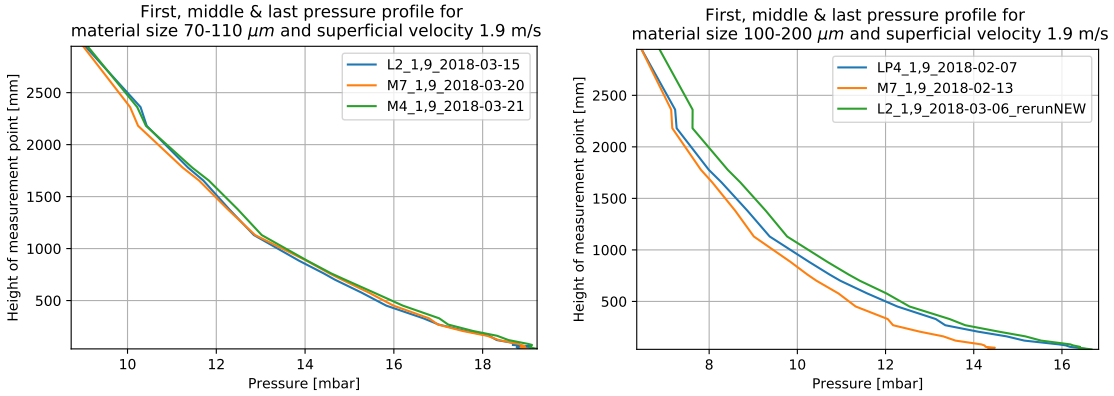

(a) 70-110 μm PSD

(b) 100-200 μm PSD

Figure 14: Pressure profile development for beginning, middle and end measurement of a test period with 1.9 m/s superficial gas velocity.

Unanimous for all pressure profiles is that the pressure decreases with the height of the riser naturally since a pressure gradient is used to induce a flow. The magnitude of pressure is related to the inventory of the riser. Comparing the two diagrams in figure 14 what might be noticed first is that the smaller particles produce a more linear relationship between the pressure and the height compared to the larger ones. This is indicative to the particle distribution inside the riser. The more linear profile would be indicative to a more homogeneous distribution while the more curved one, as seen in figure 14b, would indicate to a distribution prone to the lower dense region. This is even more plain when comparing these to the larges distribution.

Another observation is that the profiles diverge more in the 100-200 μm case than the 70-110 μm as seen in figure 14. This is believed to be due to the testing setup. Before testing it was noticed that there was a substantial particle loss at higher velocities which caused the two lower velocities to be operated first, ending with the 2.3 m/s and excluding the 2.7 m/s measurement. This seems to have allowed the inventory to stay more constant and avoiding particle loss through an inefficient cyclone. In contrast to the two larger size distributions where all superficial velocities were tested before changing ports. In the 100-200 measurements in figure 14b the middle run has a lower pressure than the first while the last has

a higher one. The suggested explanation is that particles exited the CFB through the cyclone with the air stream while performing runs at the higher superficial gas velocities, resulting in a lower pressure. This loss of material was noted and the inventory resupplied before the last run, reproducing a similar pressure in the lower region but an increase at the upper dilute zone. The pressure increase is believed to be due to the particle filter after the cyclone getting filled. This claim is strengthened by observing that for the test series of 100-200 μm, which were performed first, the pressure is between 6-7 mbar in the upper dilute zone with a cleaned filter. For the 70-100 μm PSD, which were performed last, this pressure had increased to around 9 mbar. The particle accumulating in the filter obstructs the flow increasing the pressure.

Quantifying the pressure change into an estimation of inventory material can be seen in figure 15. The estimation is based on the 100-200 μm PSD material and test series with 1.9 m/s superficial gas velocity. The left figure showing inventory approximation according to equation 11. The right figure illustrates a proposed modification to the inventory estimation, unmentioned in literature despite its simplicity. The data is ordered by date.

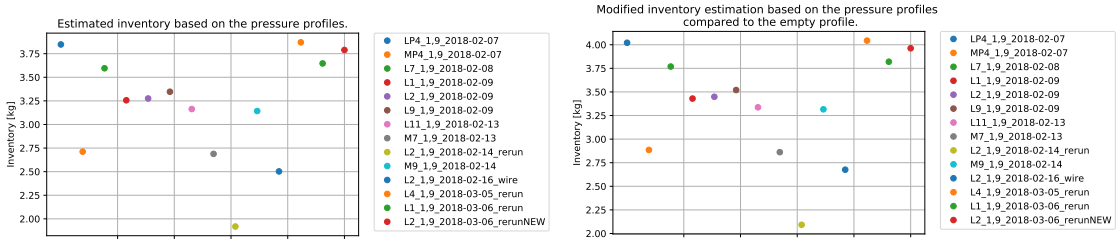

(a) Inventory approximation.

(b) Modified inventory approximation.

Figure 15: Inventory approximation and modified inventory approximation during measurements with 1.9 m/s superficial gas velocity.

What is immediate from the inventory estimation based on pressure calculation presented in 15 is that they fluctuate from run to run. Be that from the inapt pressure sensors or the nature of the measurement itself is unclear. However there is a clear decline in the estimated inventory as tests proceed. The last three runs performed two weeks later, with a resupplied inventory, clearly have a more similar inventory estimation to the very first run. Thus also indicating a continuous inventory loss. Another apparent detail is that the estimated inventory is substantially smaller than the 9 kg of glass beads added to the riser. Yet again be that of inapt pressure sensors, inaccurate nature of the method in a CFB or more likely particles in transition units. In total the CFB was filled with 11.2 kg of glass beads whereas 2.2 kg may be located in the loop seal. However more may be found in the transit from the riser to the cyclone, in the cyclone, transition to the loop seal and so on, making the low estimation seem more reliable. This can be seen when emptying different

parts of the reactor. It was seen that after a test run, the loop seal contained around 2.2 kg of material, the riser around 6-7 kg and the rest (2-3 kg) were stuck in the transit or the measurement ports. Lower superficial gas velocity or larger particle size distributions, both reduced the mass entrainment from the riser, which in turn leads to less particles getting stuck in transit causing the estimation to approach 9 kg.

Motivation for the modified inventory is simple. Subtracting the empty pressure profile, from the measured one, should also include the effect of the measurement ports and the natural pressure gradient forcing the air through the riser. Taking that into account one should acquire a better inventory estimation since the remaining pressure drop should be caused by particles in suspension. Comparing the regular estimation to the modified one in figure 15 the modified one predicts a slightly higher inventory.

Other effects which could interfere with the inventory estimation is that the particles might fill the ports affecting the pressure reading. Also filling the measurement port should reduce the drag caused by it which may affect the modified version.

Temperature readings can be found directly after the blower in order to get reliable air property readings for various calculations. The averaged temperatures for all test series can be found in appendix 13. The figures showing mean temperatures between 25 an $43°C$. The averaged temperature fluctuates depending on the temperature of the day. However a clear increasing trend can be distinguished. Upon inspection it was seen that particles got stuck in the particle filter, at the distribution plate, as testing proceeded. The increased resistance by the clogged filter caused an increase in pressure before the distribution plate. The increased compression of air causes a release of heat which explains the steady increase in temperature despite the fluctuation. After the mesh was cleaned, the temperatures were lowered again. After this observation the filter quality was regularly checked. It was observed that the filter got evenly contaminated and should therefore have little or no more effects on the CFB other than a slight temperature increase. Comparing multiple tests with the same conditions, size, velocity and port, no difference in profiles was observed from a clean to a 'contaminated' particle filter.

In order to illustrate the difference in information based on commonly applied industrial solutions to that of the capacitance probe, concentration profiles based on the measured pressure gradient can be constructed. The pressure based concentrations are later compared to concentrations received from the capacitance probe.

4.4 Capacitance probe measurements

For typical in-bed measurement profiles of mean particle velocities (left) and concentrations (right), see figure 16. The measurements were conducted on 100-200 μm

material, 2.3 m/s superficial gas velocity and normalized riser height of h/H=0.32 (port 7). The figures contain measurements conducted along a horizontal line where the probe was inserted from the left, middle (shifted 90° from the left) and right (shifted 180° from the left). The radius on the x-axis is normalized, where r/R = -1 correspond to r = - 106.5 mm and thus the entrance point of the probe into the riser and r/R = 1 to the fully inserted probe position. For these specific conditions the mean particle velocities in the centre region are 0.6 m/s higher than the superficial gas velocity. For the region close to the wall, the particles stream downwards with velocities reaching -2.6 m/s. Same measurements show particle volume concentrations around 1-1.5 vol. % near walls and 0.5 vol. % in the centre regions of the riser. Calculated via ΔP result in solids volume concentrations of approximately 1.5 vol.% and thus the flow structure around the measurement position can be attributed to the so called dilute zone regime [6]. Derived from the capacitance probe results follows a cross-sectional concentration ($c_{v,s}^{-}$) of 0.8 vol. %.

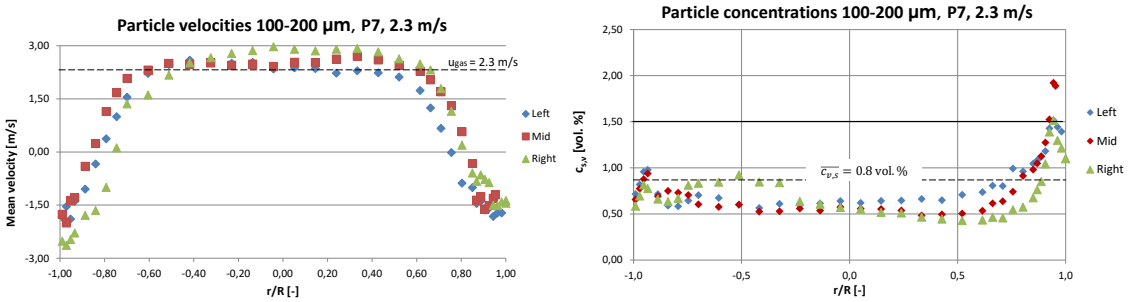

Figure 16: Particle velocities (right) and concentrations (left) for port seven at 2.3 m/s superficial gas velocity and 100-200 μm PSD.

An important feature of these results are that the three different measurements show similar characteristics. This implies that the capacitance probe results show small differences with regard to the entrance point of the riser and thus rotational symmetry mostly preserved.

More or less all resulting velocity- and concentration profiles received from the capacitance probe measurements are typical for circulating fluidized bed systems. With a dense, down streaming particle phase near the walls and a lean, up-streaming particle suspension phase in the center region. Thus, the core-annular flow structure is present, which can be expected from CFB risers operated with not too high particle concentrations and relatively low superficial gas velocities (<10 m/s). The increase in concentration along the riser walls are due to the down flowing stream of particles which were ejected from the up-going stream or simply collided with the top of the riser. Thus creates a re-circulation at the distribution plate. Simultaneously the maximum encountered particle velocity in the centre is generally higher than the superficial gas velocity. This, since the velocity is based on the cross section area, normal to the flow direction. With down streaming particles near the riser walls,

restricting the available cross section area, the gas velocity in the centre increases, above superficial gas velocity value, in order to conserve the volumetric flow rate.

4.5 Velocity and PSD dependence

Compiled particle concentration (left) and velocity (right) profiles gathered by the capacitance probe, at different superficial gas velocities, for the 100-200 μm material can be seen in figure 17. Due to the large span in values the local particle concentration is displayed in logarithmic scale. Important to note is that the top and bottom of the figure is not the top and bottom of the riser, but the highest and lowest measurement heights, corresponding to a normalized riser height as seen on the y-axis. Also the dashed lines in the figure contains exact data received from capacitance probe measurements and all coloured values in-between are interpolated.

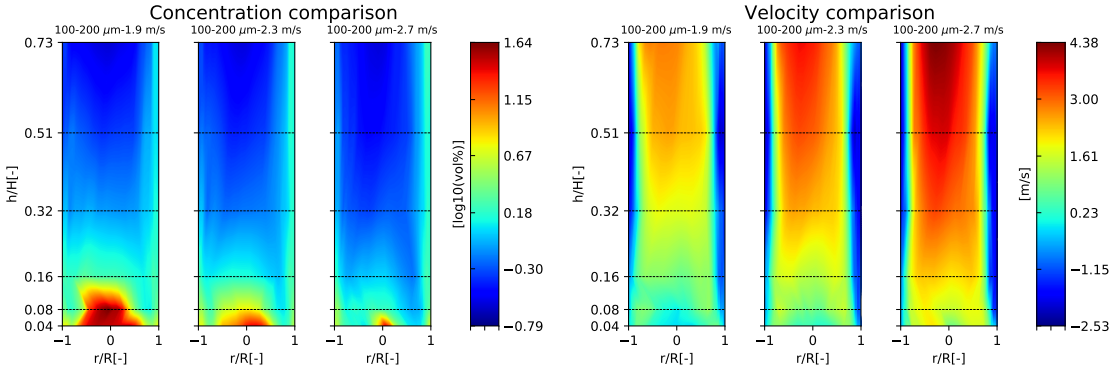

(a) Particle volumetric concentration.

(b) Particle velocity.

Figure 17: Particle velocitiy- (right) and concentration profiles (left) for port seven at varying superficial gas velocities and 100-200 μm PSD.

What can be seen when increasing the superficial gas velocity, is that for higher measurement ports, a change in superficial gas velocity does not come with any significant changes other than more pronounced core-annular flow structure. The particle velocities are up to 1.7 m/s higher than the superficial gas velocity for the case with highest velocity in comparison to no velocity difference for the lowest velocity case. The velocity profiles in figure 17b can be easily connected to the characteristics of the corresponding concentration profiles. Whereas the particle dense centre region in the bottom of the riser comes with a very low or non existing particle velocity. Which could be explained by the air taking the path of least resistance, circumventing the accumulated particles in the centre. Instead, the velocity increases further towards the walls. The velocity profiles are somewhat shifted towards the left, which is believed to be caused by the riser outlet to the cyclone.

The core annular flow is present for all cases, but as the superficial gas velocity decreases a particle dense zone in the centre appear in the lower regions. The local

particle concentration peaks around 43 vol.%, which is not far away from the fixed bed particle concentration, slightly lower than 60 vol.%. The high concentration zone in the centre reduces as the superficial gas velocity increases. This is easily seen in figure 18 with corresponding particle velocities (left) and concentrations (right) for left-side measurements of height h/H=0.08 for superficial gas velocities 1.9, 2.3 and 2.7 m/s.

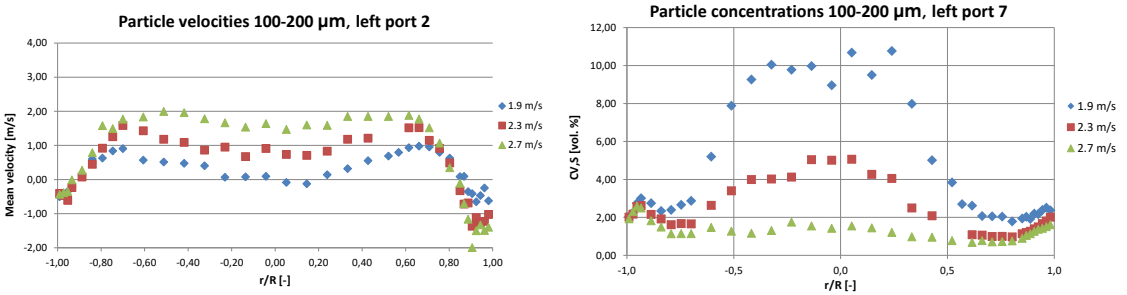

Figure 18: Particle velocities (right) and concentrations (left) for port two at varying superficial gas velocities and 100-200 μm PSD.

The accumulated particles in the bottom of the riser is most likely caused by the loop seal, from which the particles are reintroduced to the centre of the riser in such extent that they form a dead zone. Therefore it is not strange that the particle dense zone decreases with increasing superficial gas velocity, since the particles are more prone to be dragged along with the increasing gas stream. It is also seen that this phenomena is less pronounced for the particles with the largest size distribution, see figure 19. Most likely since these drastically lower the solid entrainment in the loop seal and thus less particles are reintroduced into the centre regions of the riser. The solid entrainment for the largest particles was measured 0.05 kg/s for the giving conditions. In comparison to 0.37 and 0.26 kg/s for the $70-110\mu m$ and $100-200\mu m$ materials respectively. The low entrainment can also be seen from the high concentration zones near the walls which implies that the majority of the up-going particles never leave the riser, but instead stream back down near the walls. In comparison, the finest particles do not create this particle dense zone in the centre due to the fact that these follow the gas stream more easily.

The figure 19 below showing in-bed measurement results from the normalized riser height of 0.08 for small (70-110 μm), medium (100-200 μm) and large (200-300 μm) glass particles, operated at 1.9 m/s superficial gas velocity.

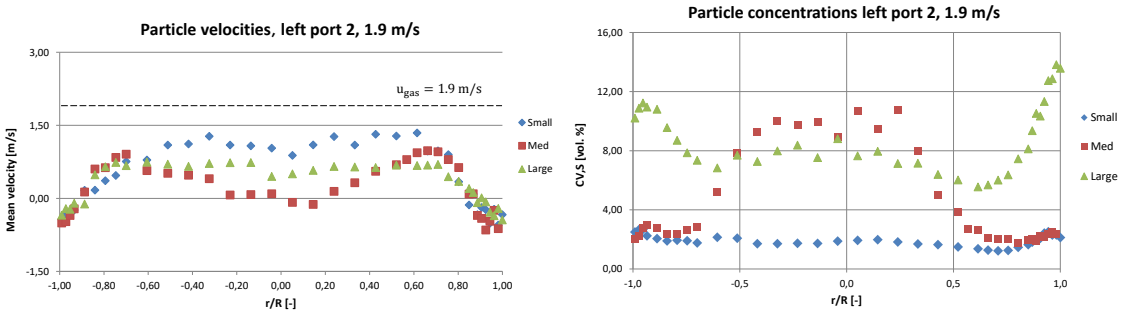

Figure 19: Particle velocities (right) and concentrations (left) for port two (h/H=0.08) at 1.9 m/s superficial gas velocities and three different PSDs.

4.6 Particle filter dependence

Depicted below are figures of particle velocities (left) and concentrations (right) from measurements with glass microbeads of 100-200 μm size distribution (mean diameter $d_{p,32} = 129\,\mu m$). Experiments were conducted with fine and coarse particle filter in the bottom of the riser and limestone of 100-350 μm PSD (mean diameter $d_{p,32} = 193\,\mu m$) conducted with coarse particle filter. The results represent in-bed measurements at normalized riser height of h/H=0.08 with 1.9 m/s superficial gas velocity.

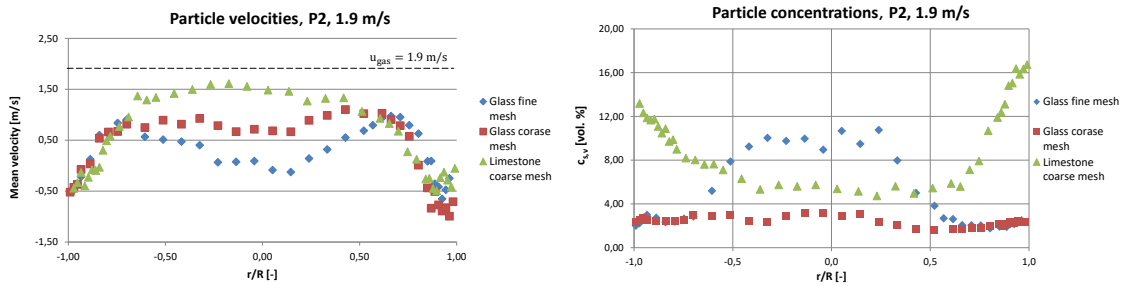

Figure 20: Particle velocities (right) and concentrations (left) for port two (h/H=0.08) at 1.9 m/s superficial gas velocities.

In contradiction to previous results found at the university there should still be a distinguishable core-annular flow in the lower regions of the riser. However, clear from the figures are significant differences in both particle velocity and concentrations. Moving up in the riser or increasing the superficial gas velocity, these changes get less pronounced. Most likely these differences come from the larger resistance and higher pressure drop for the fine filter. Therefore the introduced gas stream gets more evenly distributed across the entire distribution plate and allows the reintroduced particles from the loop seal, to the centre of the riser, to be accumulated. This result would indicate that the coarse filter does not provide sufficient resistance

to achieve an even velocity profile over the distribution plate. This allow most of the air to stream in the centre regions, reducing the amount of accumulated particles in this region.

Another theory could be that as the fine particle filter simultaneously get "clogged" in the centre, forcing the air towards the riser walls. Should that be the case, there should have been a pronounced differences between a newly cleaned filter and the old one. Such a differences was not observed causing the former explanation to be more plausible.

Yet another aspect to consider is that the glass particles used in this study are very spherical, as can be seen in 11. The sphericity of a particle greatly affects the momentum exchange between the solid and gas phase through the drag force. No images was found regarding the sphericity of the previously used limestone particles but they are expected to not be as smooth as the glass particles in this study. This could cause a difference in concentration profile near the distribution plate. Not to forget however, that the tested glass particles in this comparison had a mean diameter of $d_{p,32} = 129\,\mu m$) and the limestone $d_{p,32} = 193\,\mu m$). More suitable would probably be to compare the limestone with the largest glass particles of mean diameter $d_{p,32} = 228\,\mu m$.

4.7 Comparison to large pilot

Darmstadt TU was kind enough to share some of their measurements from their CFM600 hot plant to compare with the cold measurements. However the data was only borrowed it cannot be shown in this report. When comparing the data, at relative height of 0.33 in the CFM600 and 0.32 in CFM200, it was seen that the smallest particles at 1.9 m/s superficial velocity showed the best agreement when scaled to the hot plant. This was to be expected since the optimally scaled conditions, according to Glicksman [8], should correspond to d_p=73 μm and superficial gas velocity of 2.1 m/s, see table 9. However the comparison only agreed well for the velocity profiles while the concentration profiles were greatly overestimated, except for the largest particles at 1.9 m/s superficial gas velocity. This is believed to be caused by either the low inventory in the cold CFM200 since it should be 21 kg to be optimal or neglecting the particle density while scaling. The increase in inventory should provide more resistance and maybe reduce the rate of fluidization, thus lowering the concentration at relative height h/H=0.33. Increasing the density should also achieve this as can be seen in the simple equation of motion for a particle 1. Increasing the density and in turn the mass of a particle of similar volume reduces the magnitude of the drag force. In turn the slip velocity have to increase in order to overcome the force of gravity. This predicts a higher particle concentration in the lower dense region of the riser. Since this density difference was omitted it is likely the cause of the large mismatch in concentration profiles of the two plants.

4.8 Faults and shortcomings

While performing the tests the impact of the probe was assumed to be small enough to cause minimal disturbance to the local flow structure. Early profile evaluation also indicated towards this. However, during further evaluation where the right port profiles were mirrored so that the normalized radius r/R=-1 always represent the left port position, rather than the entrance point, a slight deviation was noticed. When the probe was almost fully inserted it tends to overestimate the velocity and particle concentration with regard to the opposing side measurement, as seen in figures 21b and 21a. It is likely that this is caused by the presence of the probe which reduces the available cross section area, forcing both gas and particles to deviate from their path. The small deviation should not cause any major errors but it may somewhat explain why the profiles are slightly skewed. There is a large concentration increase around r/R=1 side, most clear from the left port measurement. This is most likely caused by the cyclone exit in the opposite region, which cause the particles to leave the riser. As a result, the concentration profiles on the opposite side (r/R=1) are higher due to the higher amount of down streaming particles.

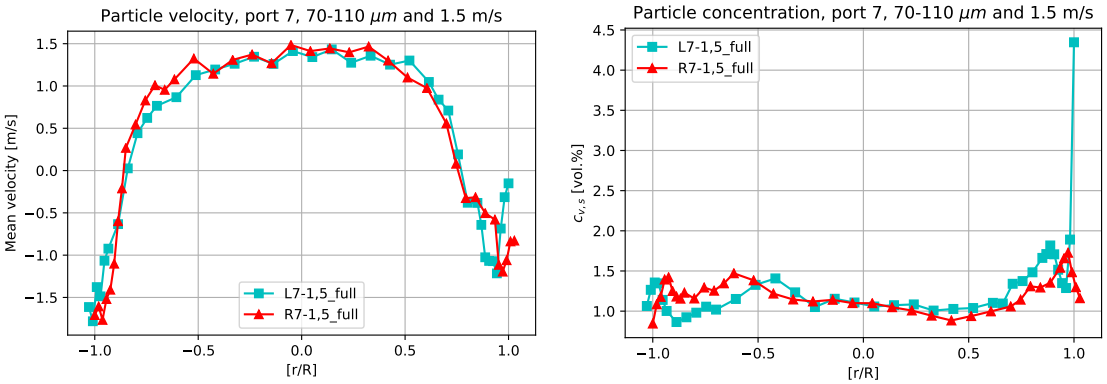

(a) Velocity comparison.

(b) Concentration comparison.

Figure 21: Profile comparison (left vs right ports) at port 7 for 1.5 m/s superficial gas velocity and 70-110μm PSD.

While keeping the superficial gas velocity the same while increasing the particle size, the concentration profile becomes less homogeneous and tends to accumulate toward the lower regions of the riser. This is to be expected according to section 2.1.2. As a result the reduced particle concentration in the upper dilute zone leads to increased particle velocities due to the reduced interphase momentum exchange. However, the velocity profile for the largest particles in figure 22 deviates from this hypothesis by displaying the lowest particle velocity of the three size distributions. This may be explained by the very low particle concentrations in the upper dilute zone, as seen in figure 22a. The lack of particles may render the capacitance probe unable to obtain accurate velocity estimation which might have been avoided if using a single fiber

reflection probe instead. The theory is further strengthened by comparing port 11 measurements at 1.9 m/s superficial gas velocity from the 200-300 PSD to smaller PSD in the appendix. The profiles are are less smooth, for the larger PSD than the others, even if the low velocity is explained elsewise.

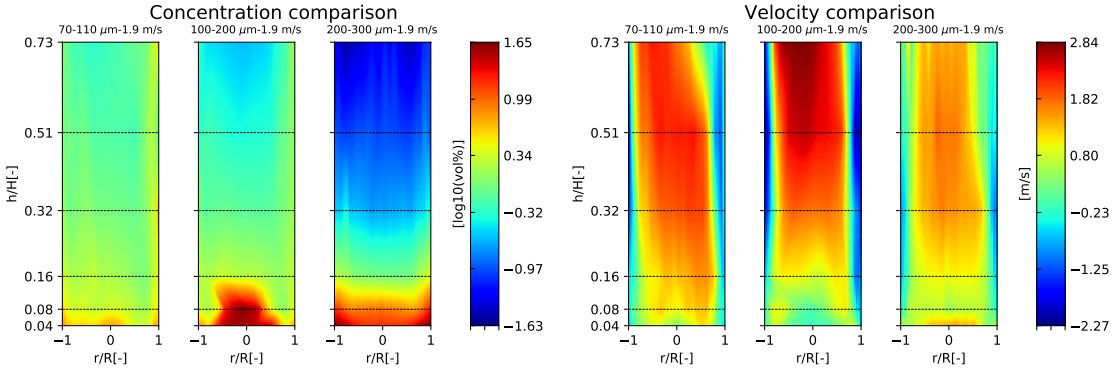

(a) Particle volumetric concentration development with varying PSD.

(b) Particle velocity development with varying PSD.

Figure 22: Particle velocities (right) and concentrations (left) for port seven at 1.9 m/s superficial gas velocities and varying PSD.

Another interesting remark is that the largest particles display a core annular flow structure, but as the superficial gas velocity increases, the particle dense zone in the bottom region as previously discussed, is yet again obtained.

4.9 Further work and improvements

It was not possible within the scope of this project to perform tests with higher particle densities. This should be highly interesting in order to validate the simplified Glicksman scaling criteria of neglecting density ratios during operations in the viscous limit regime. However, if these tests should be performed using the equipment at Darmstadt TU it might be difficult to reach the required superficial gas velocities to enter the fully turbulent regime.

The lower velocities proved to cause smaller inventory loss during operation with fine sized particles. The cyclone is therefore believed to be unable to separate the solids from the gas flow at higher velocities. One improvement to avoid this could be to install a smaller cyclone in series. Literature [6] suggests that large CFB plants often install cyclones parallel to each other since larger cyclones tends to drop in efficiency.

Since the data showed some asymmetry from left to right port, possibly due to the effect of the probe, one could collect half profile from respective side, thus minimizing the intrusion of the probe. The collection from left and right side and collecting all the lowest velocities first could however cause particle loss due

to the extra port changes. One should proceed with caution and observe if these adjustments improve or impairs the results.

5 Conclusion

With the electrostatic problem solved for the smallest particle size distribution, all experiments show consistent and reliable results. As expected in CFB systems with relatively low particle concentrations and superficial gas velocities, the core-annular flow structure is mostly present. The core-annular flow structure is some times obstructed in the lower regions of the riser, depending on the superficial gas velocity and particle size distributions. The cause of this might be the high amount of recirculating bed material through the loop seal, together with a high resistance particle filter at the distribution plate in the bottom of the riser.

The results were well comparable to the hot pilot plant and showed good accordance to the simplified Glicksman scaling laws. The minor variation in inventory, the small change in physical properties of the material and the displayed consistency of the equipment all indicate that the acquired data is suitable for further processing.

References

[1] Leckner, B., P. Szentannai, and F. Winter, (2011), *Scale-up of fluidized-bed combustion – A review*, vol. 90(10), p. 2951-2964, Fuel.

[2] Johnsson, F, Kjarstad, J, Odenberger, M, (2012), *The importance of CO2 capture and storage- A geopolitical discussion*, p. 655-668. Dep. of Energy and Environment, Chalmers University of Technology, Gothenburg, Sweden.

[3] Azar, C, Johansson, D, Mattsson, N, (2013), *Meeting global temperature targets—the role of bioenergy with carbon capture and storage*, Dep. of Energy and Environment, Chalmers University of Technology, Gothenburg, Sweden.

[4] Sadeghbeigi, R, (2012), *Fluid Catalytic Cracking Handbook*, 3rd ed. Waltham, MA, USA: Elsevier.

[5] Zactruba, J, (2009), *How does a Circulating Fluidized Bed Boiler Work*, Bright Hub Engineering.

[6] Grace, J.R, Avidan, A.A, Knowlton, T.M, (1997), *Circulating Fluidized Beds*, 1st ed. Madras, India: Chapman & Hall

[7] PAUL CHO (2005), *Development and Characterisation of Oxygen-Carrier Materials for Chemical-Looping Combustion* , Chalmers University of Technology.

[8] Glicksman, L.R, Hyre, M, Woloshon, K (1993), *Simplified scaling relationships for fluidised beds*, Powder Technology, 77, pp.177-199.

[9] Herdel, P., et al., (2017), *Experimental investigations in a demonstration plant for fluidized bed gasification of multiple feedstock's in 0.5 MWth scale*, Fuel. 205: p. 286-296.

[10] Ohlemüller, P., J. Ströhle, and B. Epple, (2017), *Chemical looping combustion of hard coal and torrefied biomass in a 1MWth pilot plant*, International Journal of Greenhouse Gas Control. 65: p. 149-159.

[11] Hilz, J., et al., (2017), *Long-term pilot testing of the carbonate looping process in 1MWth scale*, Fuel. 210: p. 892-899.

[12] Shi, X, Lan, X, Liu, F, Zhang, Y, Gao, J, (2014) *Effect of particle size distribution on hydrodynamics and solids back-mixing in CFB risers using CPFD simulation*, Powder Technology, 266, pp.135-143.

[13] Fotovat, F, Xiaotao, T.Bi, Grace, J.R (2018), *A perspective on electrostatics in gas-solid fluidized beds: Challenges and future research needs*, 1st ed. Elsevier B.V

[14] X. Yu,W. Li, Y. Xu, J.Wang, Y. Yang, N. Xu, H.Wang, (2010), *Effect of polymer granules on the electrostatic behavior in gas-solid fluidized beds*, Vol. 49, p.132-139, Industrial and Engineering Chemistry Research.

[15] Wiesendorf, V, Werther, J, (2000), *Capacitance probes for solids volume concentration and velocity measurements in industrial fluidized bed reactors*, Powder Technology, 110, pp.143-157.

[16] Stokes, Debbie J, (2008), *Principles and Practice of Variable Pressure Environmental Scanning Electron Microscopy (VP-ESEM)*, Chichester: John Wiley & Sons. ISBN 978-0470758748

[17] Goldstein, J, Newbury, D, Lyman, C, Echlin, P, Lifshin, E, Sawyer, L, Michael, J, (2013), *Scanning Electron Microscopy and X-Ray Microanalysis*, Kluwer Academic/Plenum Puplisher, pp.1-20.

[18] Bartholomew, R.N, Casagrande, R.M, (1957), *Measuring Solids Concentration in Fluidized Systems by Gamma-Ray Absorbtion*, Industrial & Engineering Chemistry, 49, pp.428-431.

[19] Werther, J, (1999), *Measurement Techniques in fluidized beds*, Powder Technology, 102, pp.15-36.

[20] Werther, J, Hage, B, Rudnik, C, (1996), *A comparison of laser Doppler and single-fibre reflection probes for measurement of the velocity of solids in a gas-solid circulating fluidized bed*, Chemical Engineering and Processing, 35, pp.381-391.

[21] Rhodes, M.J, Laussmann, P, (1992), *A simple non-isokinetic sampling probe for dense suspension*, Powder Technology, 70, pp.141-151.

[22] Daikeler, A, Ströhle, J, Epple, B, (conference paper for the 23rd International conference on Fluidized Bed Conversion in Seoul, May 13th-17th 2018), *Experimental Investigation of the Flow Hydrodynamics in a* $1\,MW_{th}$ *Dual Fluidised Bed Pilot Plant With a Capacitance Probe*, Institute for Energy Systems & Technology, Technische Universität Darmstadt, Darmstadt 64287, Germany.

[23] Wiesendorf, V, (2000), *The capacitance probe- a tool for flow investigation in gas-solid fluidization systems*, Aachen, Shaker Verlag.

[24] Martin, M.P, Turlier, P, Bernard, J.R, Wild, G (1992), *Gas And solid behavior in cracking circulating fluidised beds*, Powder Technology, 70, pp.249-258.

[25] Kantzas, A, Wright, I, Kalogerakis, N, (1997), *Quantification of channeling in polyethylene resin fluid beds using X-Ray computer assisted tomography*, Chemical Engineering Science, 52, pp.2023-2035.

6 Appendix material properties

The following appendix cover valuable data required for evaluation and validation of the results from capacitance probe measurements.

For density measurements on different size distributions of glass microbeads, performed on clean material and dirty material received after several operating hours in a cold flow CFB unit, see table below.

Table 13: Density measurements on clean and dirty material.

Size distribution	**70-110**	**100-200**	**200-300**
Material density [kg/m^3]	2504	2504	2504
Bulk density clean [kg/m^3]	1472.23	1447.19	1486.17
Bulk density clean with salt [kg/m^3]	1486.24	-	-
Bulk density dirty [kg/m^3]	1514.30	1476.56	1468.76

Dielectric constants for both probes measured on different size distributions of clean material and dirty material received after several operating hours in a cold flow CFB unit, see table 14.

Table 14: Dielectric constants for both probes on clean material and dirty material.

Size distribution	**Clean material**		**Dirty material**	
	Probe 1	**Probe 2**	**Probe 1**	**Probe 2**
70-110	3.400	3.423	3.401	3.432
100-200	3.305	3.389	3.418	3.413
200-300	3.401	3.422	3.312	3.351

6.1 Material 70-110 μm PSD

Sieving results from glass microbeads of 70-110 μm size distribution. Performed on 50 grams of; clean material and dirty material received after several operating hours in a cold flow CFB unit.

Table 15: Sieving results from glass microbeads of 70-110 μm on clean material and dirty material.

Sieve size [μm]	**40**	**63**	**90**	**106**	**125**
Weight clean [g]	48.91	44.50	27.22	4.01	0.06
Weight clean with salt [g]	49.33	47.04	33.74	6.06	0
Weight dirty with salt [g]	49.42	46.46	34.06	5.12	0

Salt, NaCl, concentrations in the material:

Table 16: Salt concentrations in the material.

Salt, NaCl	**wt % based on inventory**
Added	1
After drying process	0.397
After 40 operating hours inside CFB	0.298

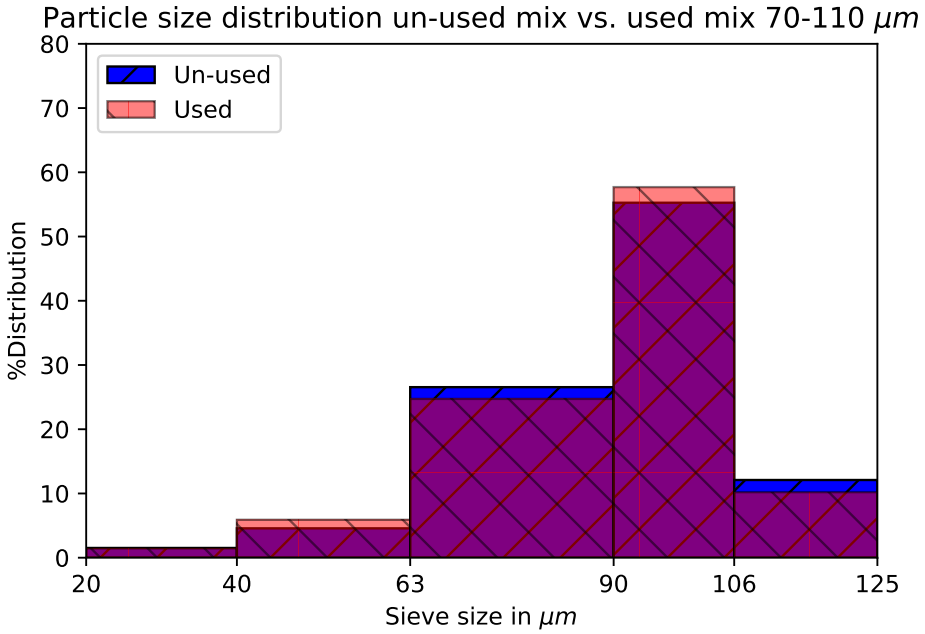

Figure 23: Histogram showing sieving results for material mixed with 1 wt% salt. Used and unused material.

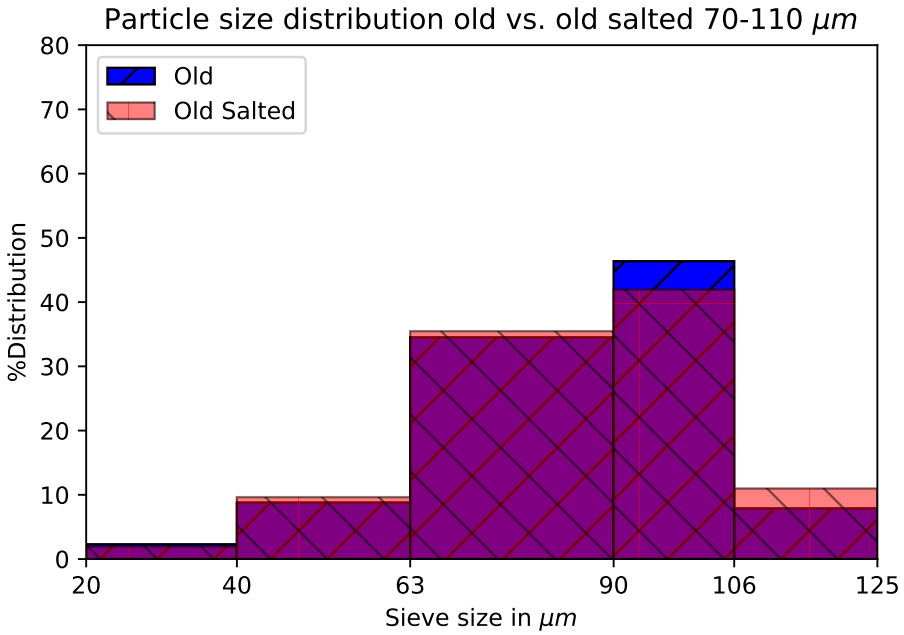

Figure 24: Histogram showing sieving results for clean material and material mixed with 1 wt% salt. The material is from the old batch.

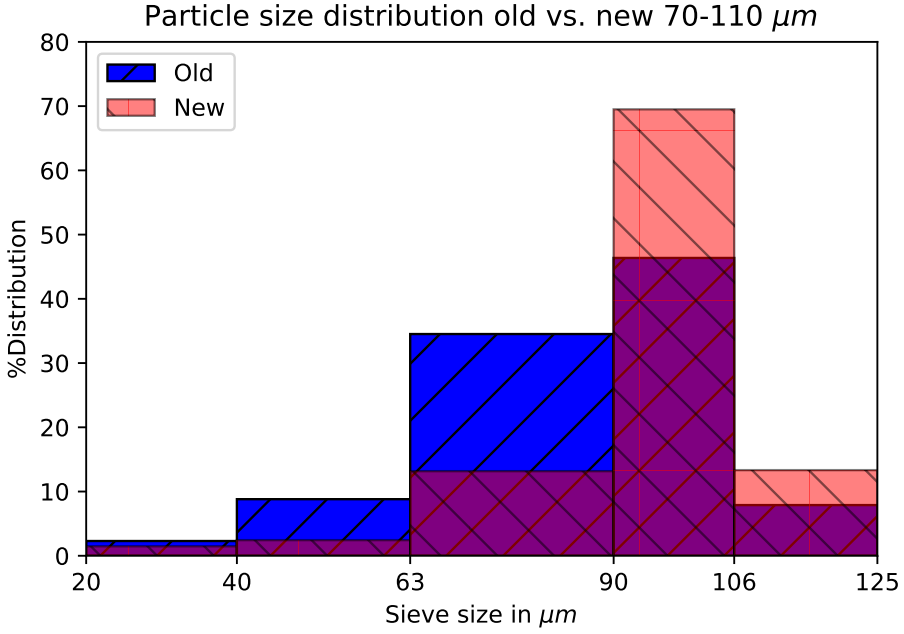

Figure 25: Histogram showing sieving results for clean old- and clean newly purchased material.

Solid particle entrainment measured in loop seal for particle size distribution of 70-110 μm for different superficial gas velocities.

Table 17: Solid particle entrainment in loop seal for 70-110 μm particles.

Date	**Superficial gas velocity [m/s]**	**1.5**	**1.9**	**2.3**
19.03.2018	**Solid entrainment [kg/s]**	0.276	0.373	-
26.03.2018	**Solid entrainment [kg/s]**	-	-	0.588

6.2 Material 100-200 μm PSD

Sieving results from glass microbeads of 100-200 μm size distribution. Performed on 50 grams of; clean material and dirty material received after several operating hours in a cold flow CFB unit.

Table 18: Sieving results from glass microbeads of 100-200 μm on clean and dirty material.

Sieve size [μm]	**63**	**90**	**106**	**125**	**150**	**160**	**180**	**200**	**224**
Mass clean [g]	49.88	49.40	46.28	38.39	1.24	0.8	0.63	0.06	0
Mass dirty [g]	49.84	49.22	46.37	40.64	1.17	0.94	0.66	0.05	0

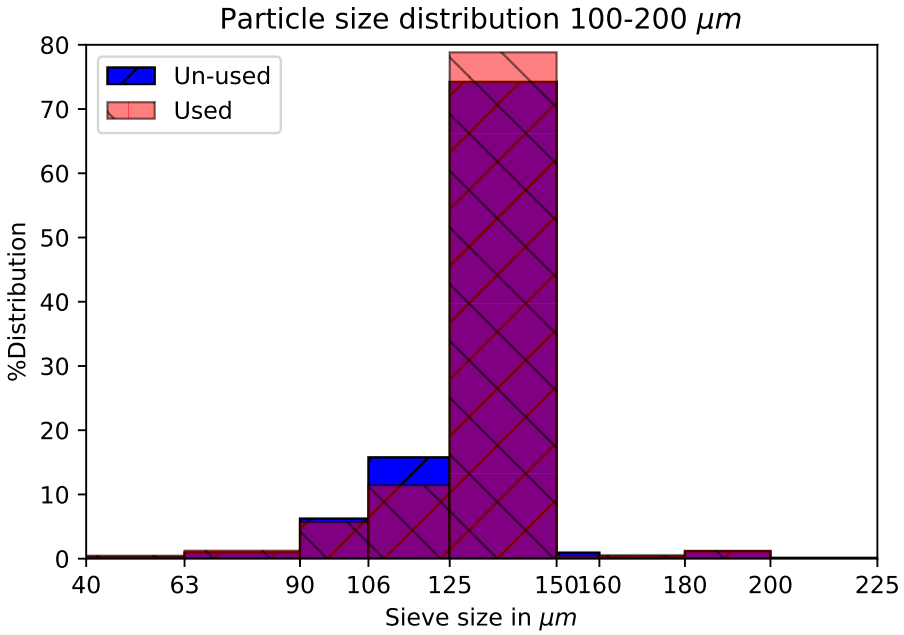

Figure 26: Histogram showing sieving results for used and unused material.

Solid particle entrainment measured in loop seal for particle size distribution of 100-200 μm for different superficial gas velocities.

Table 19: Solid particle entrainment in loop seal for 100-200 μm particles.

Date	**Superficial velocity [m/s]**	**1.5**	**1.9**	**2.3**	**2.7**
07.02-2018	**Solid entrainment [kg/s]**	-	0.293	0.427	0.560
13.02-2018	**Solid entrainment [kg/s]**	0.076	0.224	0.427	0.539

6.3 Material 200-300 μm PSD

Sieving results from glass microbeads of 200-300 μm size distribution. Performed on 50 grams of; clean material and dirty material received after several operating hours in a cold flow CFB unit.

Table 20: Sieving results from glass microbeads of 200-300 μm on clean and dirty material.

Sieve size [μm]	**180**	**200**	**224**	**250**	**280**	**300**	**355**
Weight clean [g]	47.39	44.62	36.89	19.00	0.30	0	0
Weight dirty [g]	47.37	44.25	37.26	17.52	0.73	0.12	0

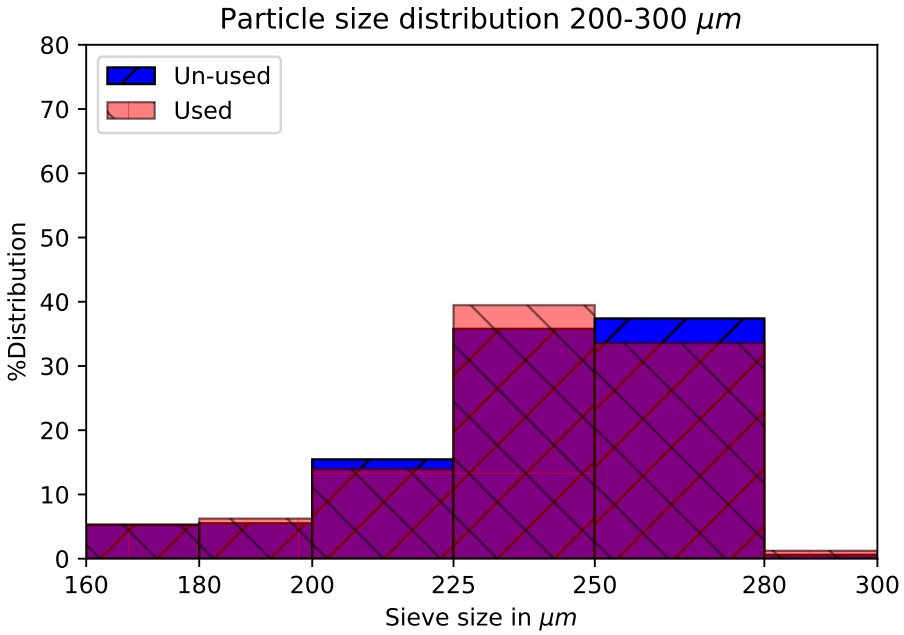

Figure 27: Histogram showing sieving results for used and unused material.

Solid particle entrainment measured in loop seal for particle size distribution of 200-300 μm for different superficial gas velocities.

Table 21: Solid particle entrainment in loop seal for 200-300 μm particles.

Date	**Superficial velocity [m/s]**	**1.5**	**1.9**	**2.3**	**2.7**
19.02-2018	**Solid entrainment [kg/s]**	0	0.094	0.210	0.375
26.02-2018	**Solid entrainment [kg/s]**	0	0.0404	0.184	0.283
27.02-2018	**Solid entrainment [kg/s]**	0	0.031	0.154	0.325

7 Appendix protocol

Below are schematic figures of a test protocol and also the measurement protocol.

Table 22: Test protocol capacitance probe measurements.

date	2018-XX-XX
port	
probe geometry	double - 34 mm length
u$_{gas}$ **[m/s]**	
air flow LS4.1 RC [l/min]	2.1
air flow LS4.1 SC [l/min]	2.1
air flow LS4.1 LV [l/min]	2.1
base signal before S1 [%]	
base signal before S2 [%]	
base signal after S1 [%]	
base signal after S2 [%]	
entrainment mass flow [kg/s]	
pressure filter [mbar]	
scale value at measurement point 213 mm	-8

Table 23: Test protocol measurement points

measurement no.	**point [mm]**	**scale of probe [mm]**	**point distance**
1	2	207	
2	4	205	2
3	6	199	2
4	8	197	2
5	10	195	2
6	12	193	2
7	17	188	5
8	22	183	5
9	27	178	5
10	32	173	5
11	37	168	5
12	47	158	10
13	57	148	10
14	67	138	10
15	77	128	10
16	87	118	10
17	97	108	10
18	107	98	10
19	117	88	10
20	127	78	10
21	137	68	10
22	147	58	10
23	157	48	10
24	167	38	10
25	177	28	10
26	182	23	5
27	187	18	5
28	192	13	5
29	197	8	5
30	202	3	5
31	204	1	2
32	206	999	2
33	208	997	2
34	210	995	2
35	212	993	2
36	214	991	2
37	216	989	2
38	218	987	2

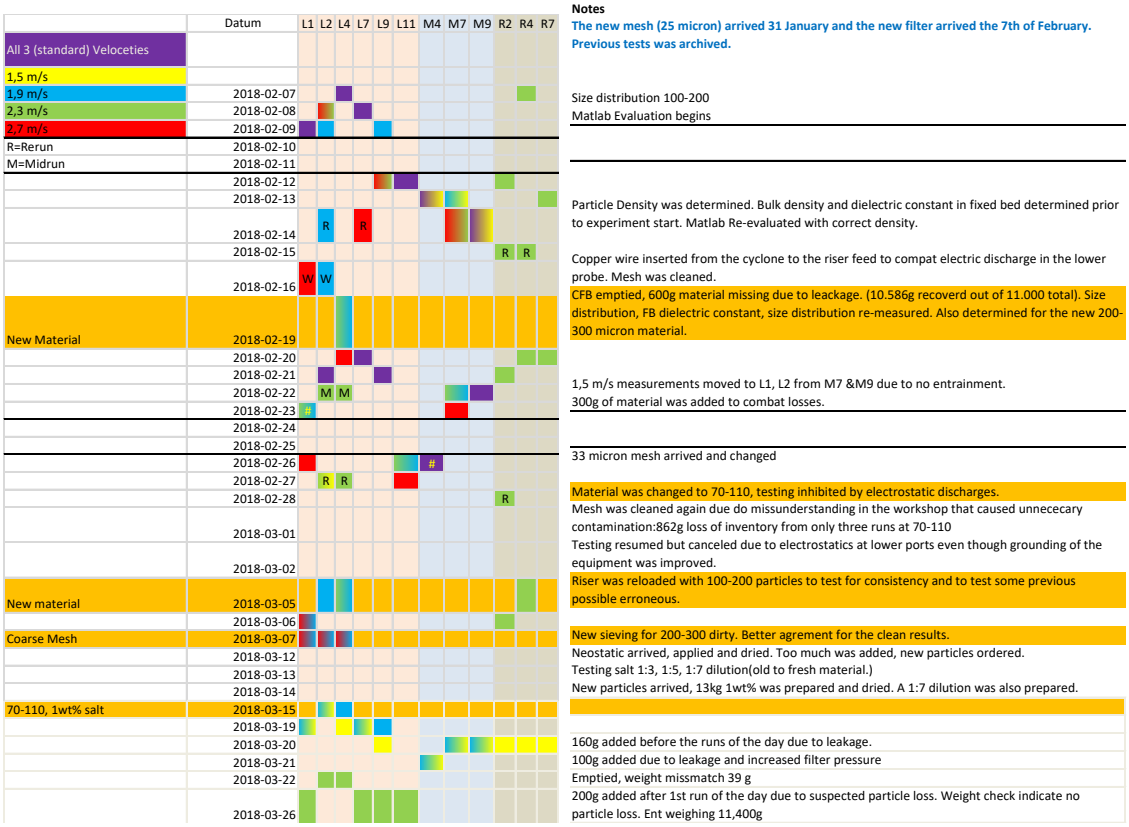

Figure 28: Measurement protocol.

8 Appendix 70-110 μm PSD probe results

Evaluated results from capacitance probe measurements inside a scaled, cold flow CFB model at Darmstadt Technical University. Figures showing profiles of glass microbeads with a size distribution of 70-110 μm for mean particle velocity and, for the two lowest measurement heights, constant weighted particle concentration. Figures for port four and higher shows the weighted quantile of particle concentrations instead. Measurement heights are according to table 24, with a total riser height of approximately 3.1 meters.

Table 24: Heights of the ports on the scaled cold flow CFB model.

Port	**P1**	**P2**	**P4**	**P7**	**P9**	**P11**
Height [mm]	124	248	496	992	1580	2262
h/H [-]	0.04	0.08	0.16	0.32	0.51	0.73

8.1 Compiled data

Results from glass microbeads with a size distribution of 70-110 μm compiled into figures of velocity, concentration and mass flux development across the riser. Note that the shown results are from port one to eleven. That is, from 124 mm to 2262 mm height and not the complete 3.1 m riser height.

8.1.1 Superficial gas velocity 1.5 m/s

Figures of velocity, concentration and mass flux development across the riser operating at 1.5 m/s superficial gas velocity.

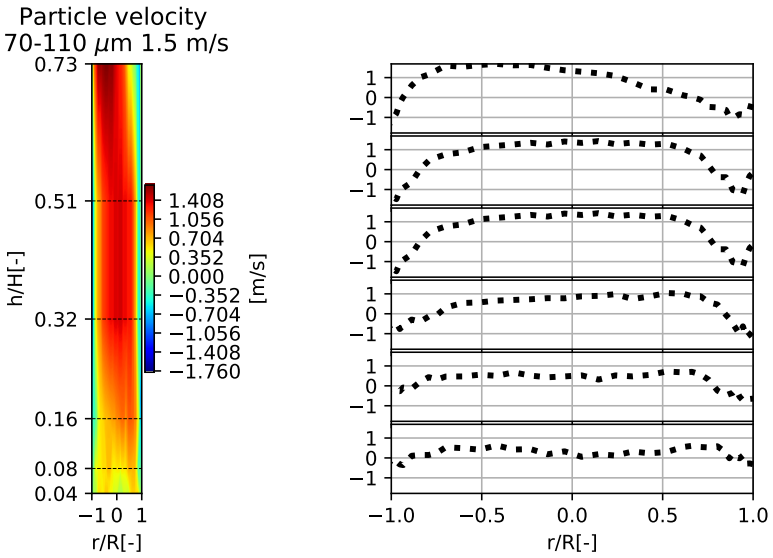

Figure 29: Particle velocity development across the riser.

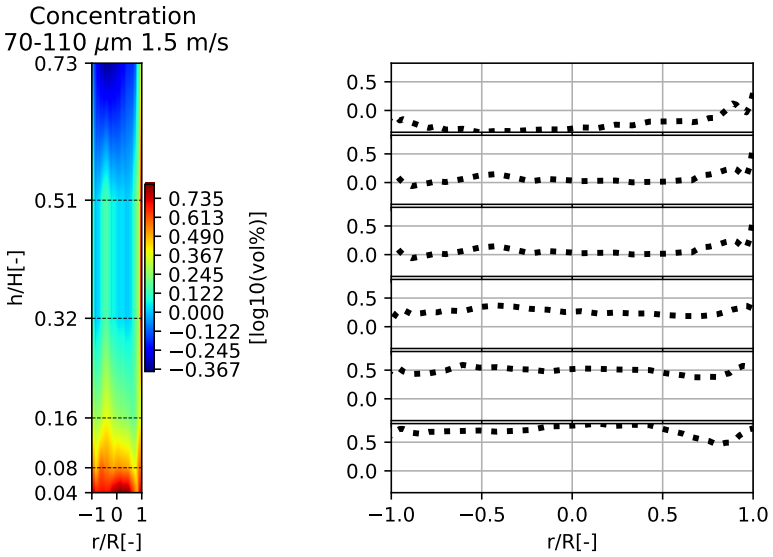

Figure 30: Particle volumetric concentration development across the riser.

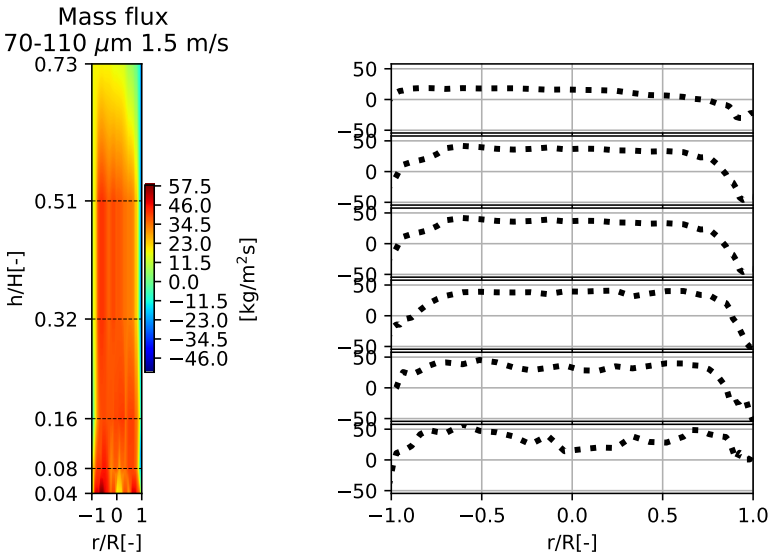

Figure 31: Particle mass flux development across the riser.

8.1.2 Superficial gas velocity 1.9 m/s

Figures of velocity, concentration and mass flux development across the riser operating at 1.9 m/s superficial gas velocity.

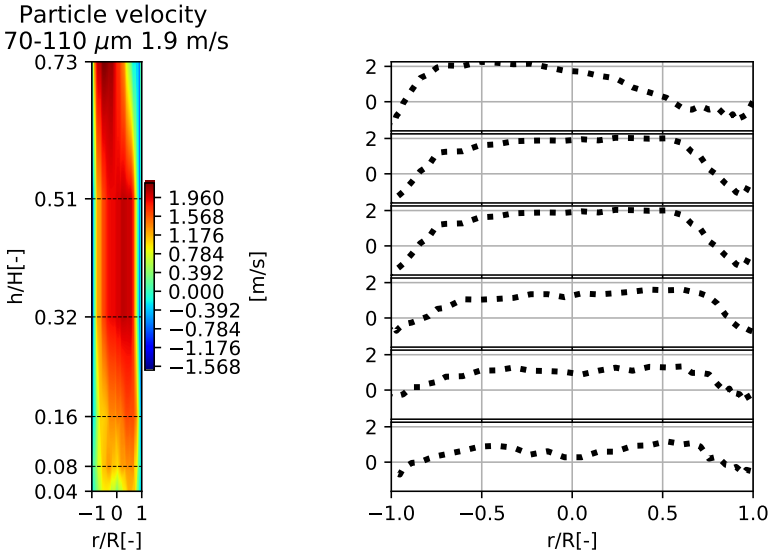

Figure 32: Particle velocity development across the riser.

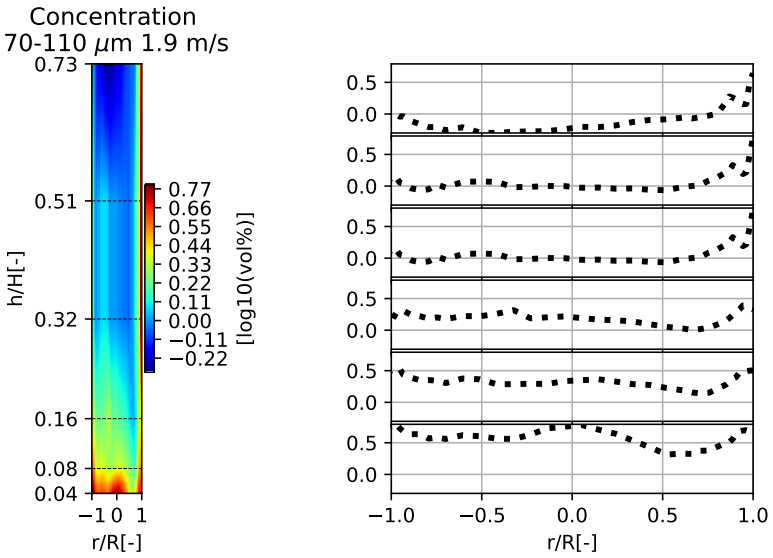

Figure 33: Particle volumetric concentration development across the riser.

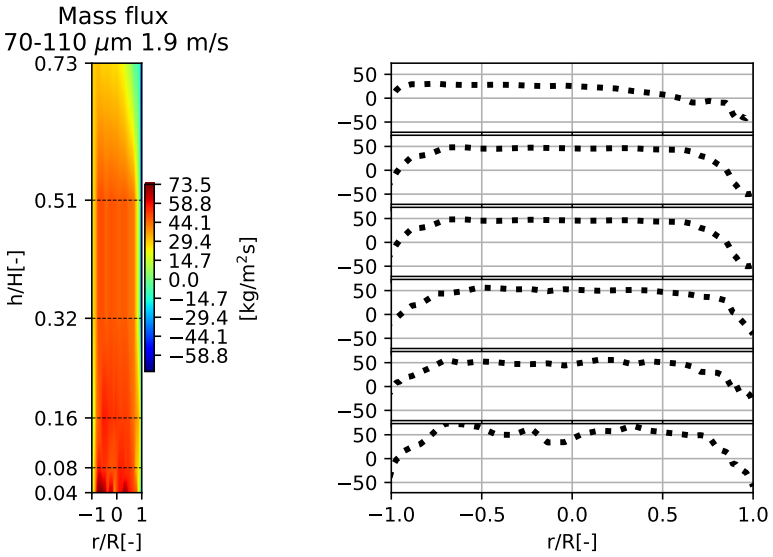

Figure 34: Particle mass flux development across the riser.

8.1.3 Superficial gas velocity 2.3 m/s

Figures of velocity, concentration and mass flux development across the riser operating at 2.3 m/s superficial gas velocity.

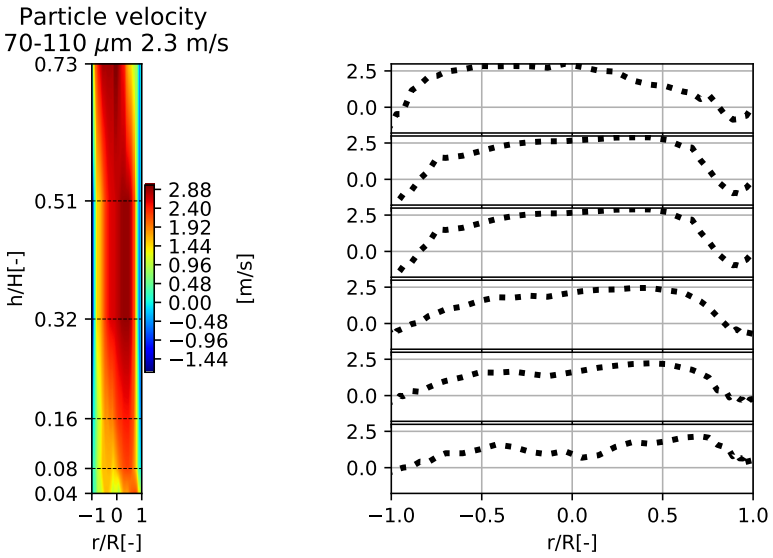

Figure 35: Particle velocity development across the riser.

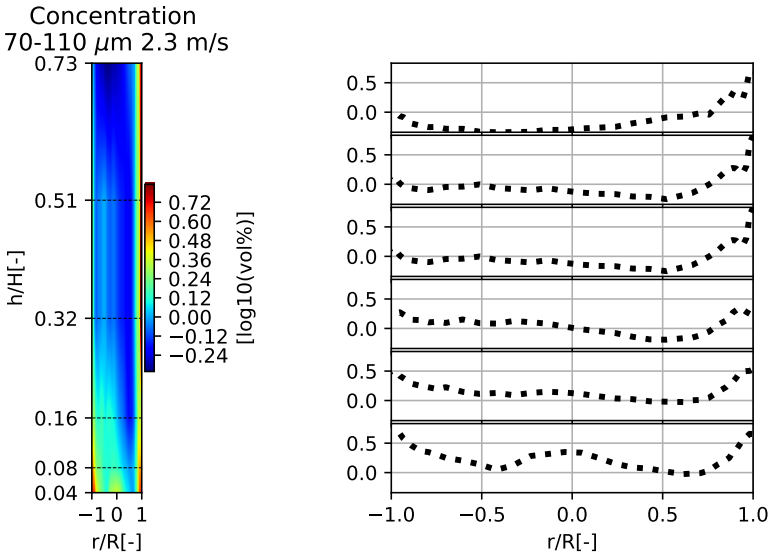

Figure 36: Particle volumetric concentration development across the riser.

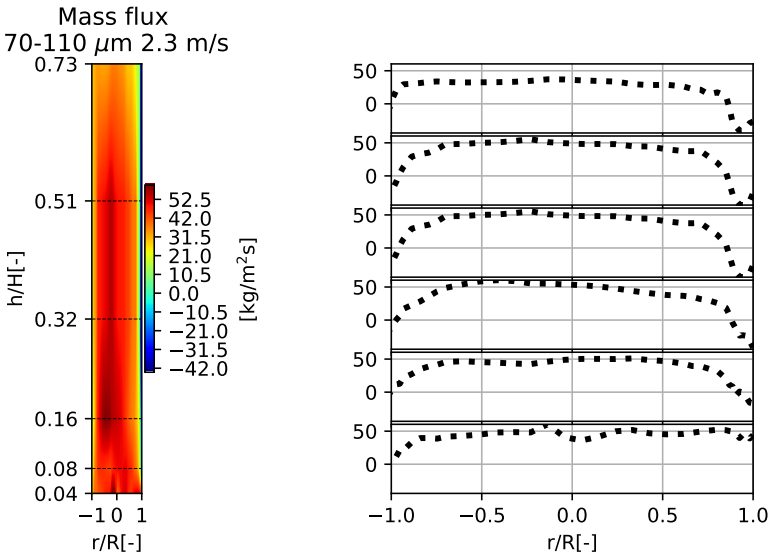

Figure 37: Particle mass flux development across the riser.

8.2 Port one

Following profile measurements are from port one at a height of 124 mm.

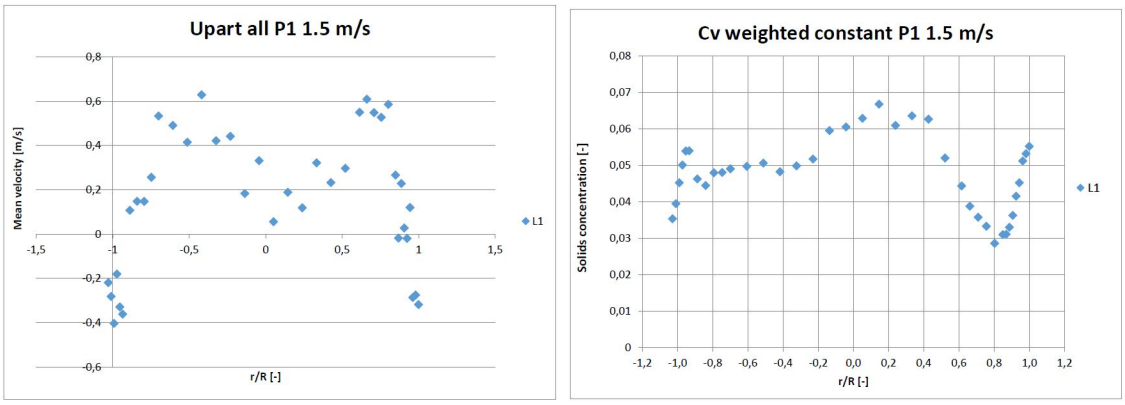

(a) Particle velocity.

(b) Particle concentration.

Figure 38: Profile measurements at port one with 1.5 m/s superficial gas velocity.

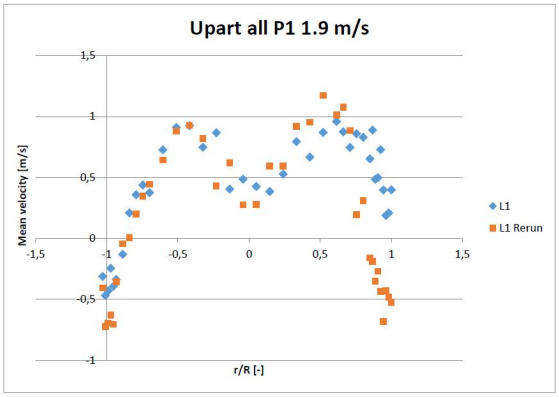

(a) Particle velocity.

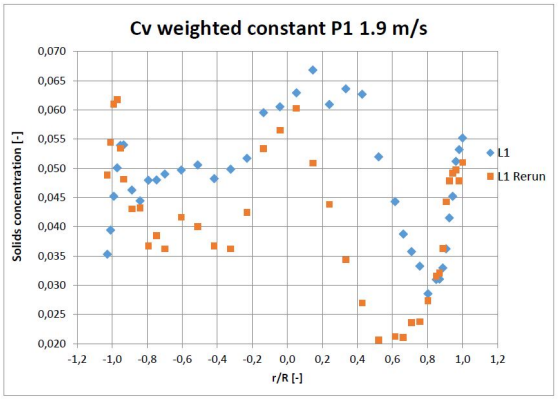

(b) Particle concentration.

Figure 39: Profile measurements at port one with 1.9 m/s superficial gas velocity.

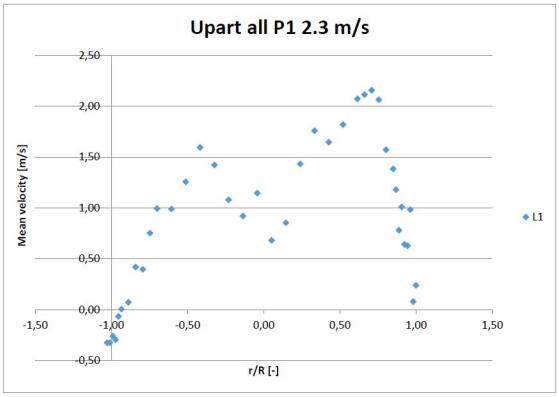

(a) Particle velocity.

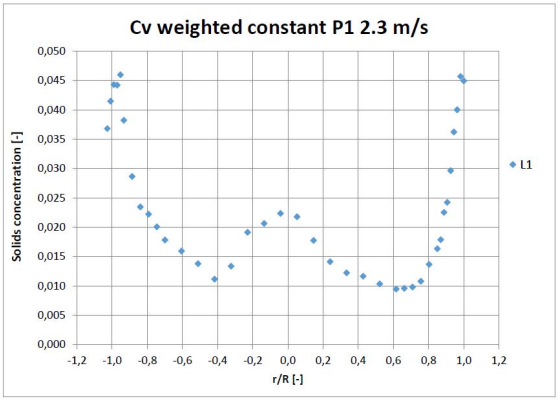

(b) Particle concentration.

Figure 40: Profile measurements at port one with 1.9 m/s superficial gas velocity.

8.3 Port two

Following profile measurements are from port two at a height of 248 mm.

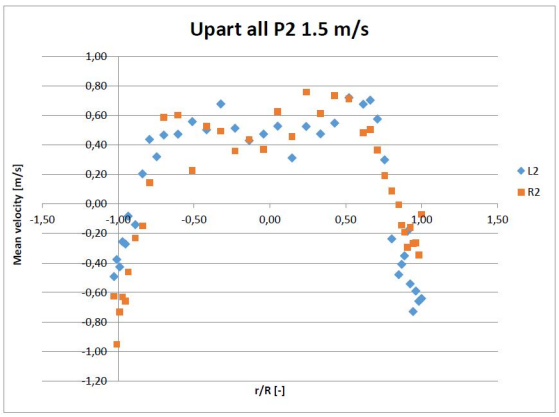

(a) Particle velocity.

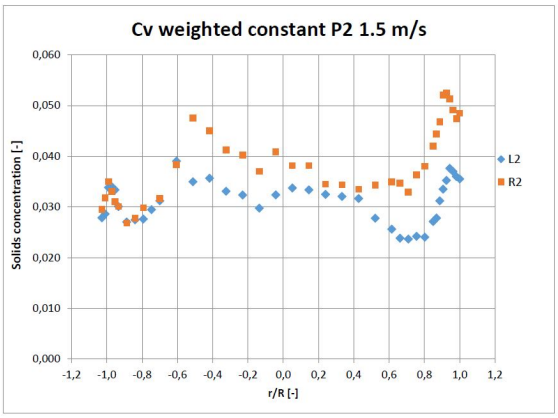

(b) Particle concentration.

Figure 41: Profile measurements at port two with 1.5 m/s superficial gas velocity.

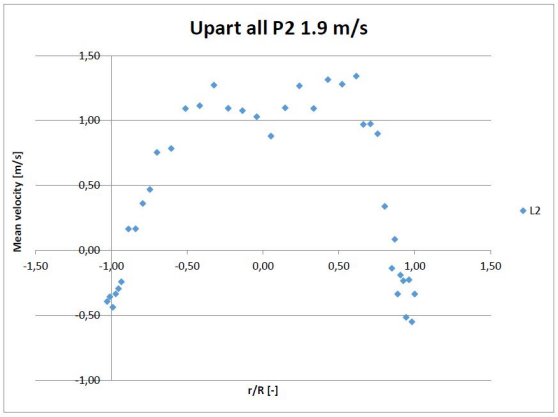

(a) Particle velocity.

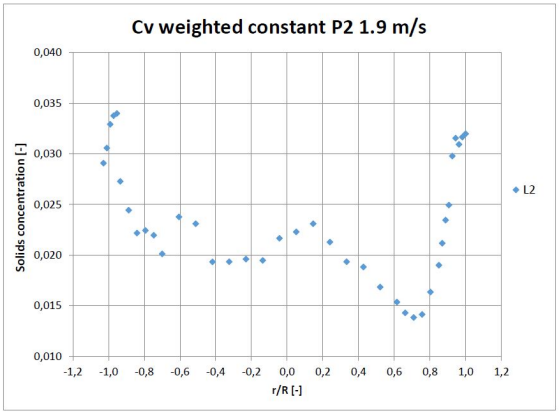

(b) Particle concentration.

Figure 42: Profile measurements at port two with 1.9 m/s superficial gas velocity.

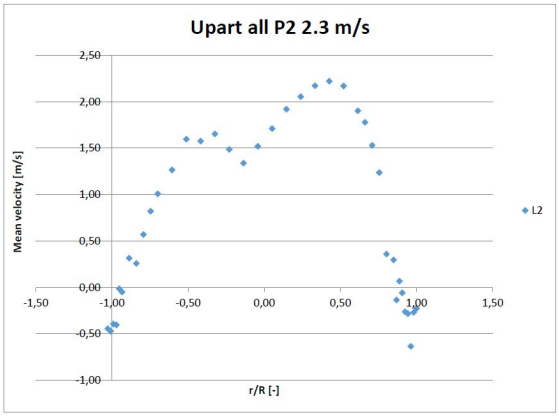

(a) Particle velocity.

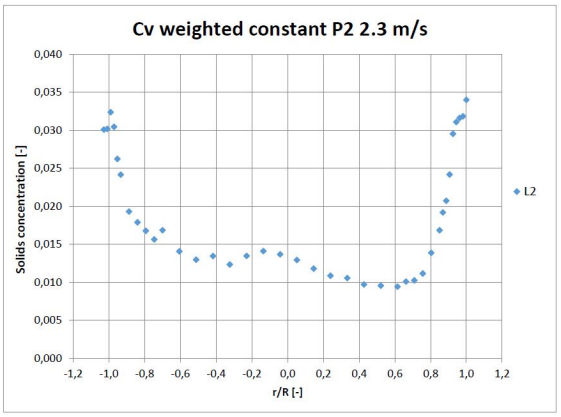

(b) Particle concentration.

Figure 43: Profile measurements at port two with 1.9 m/s superficial gas velocity.

8.4 Port four

Following profile measurements are from port four at a height of 496 mm.

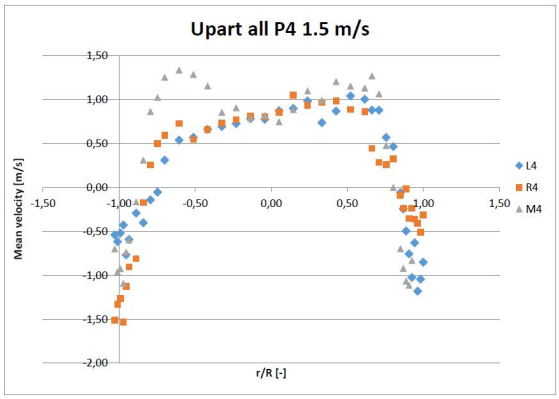

(a) Particle velocity.

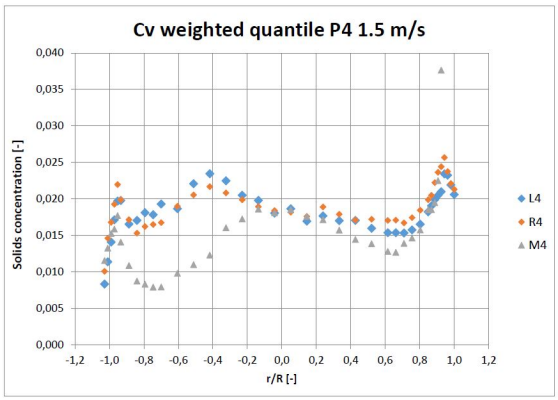

(b) Particle concentration.

Figure 44: Profile measurements at port four with 1.5 m/s superficial gas velocity.

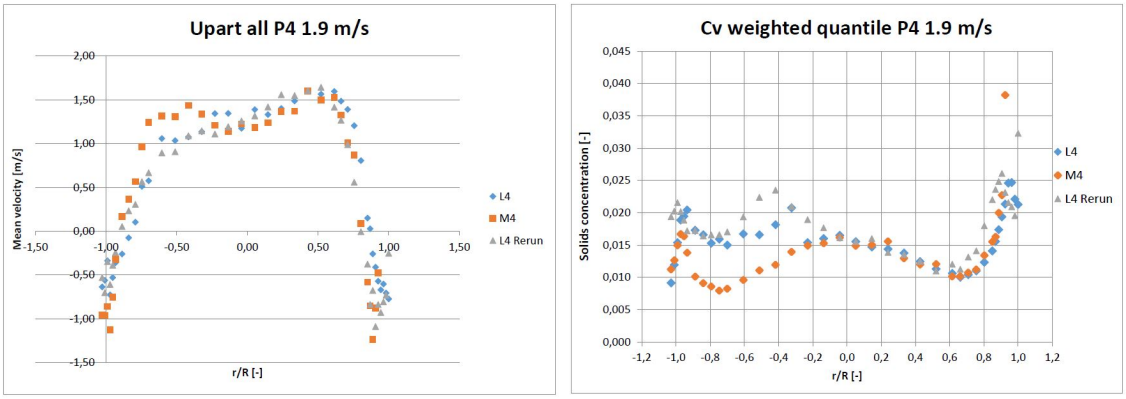

(a) Particle velocity. (b) Particle concentration.

Figure 45: Profile measurements at port four with 1.9 m/s superficial gas velocity.

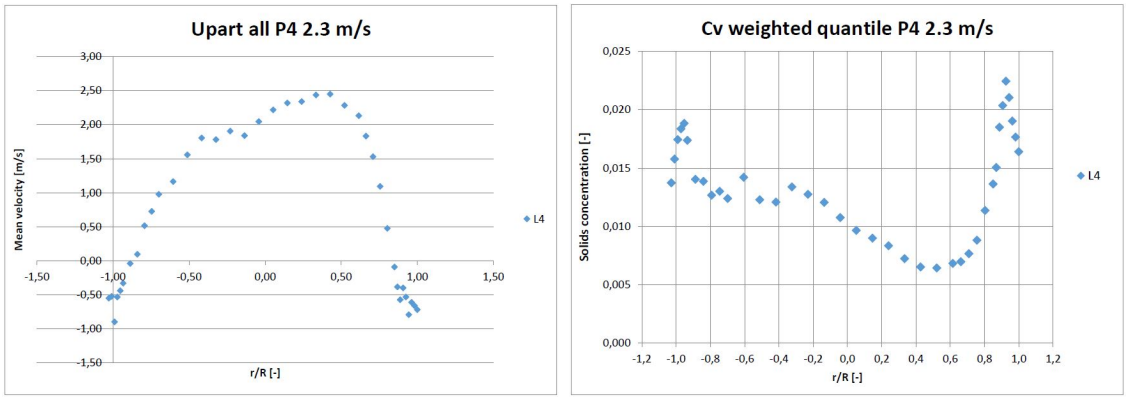

(a) Particle velocity. (b) Particle concentration.

Figure 46: Profile measurements at port four with 1.9 m/s superficial gas velocity.

8.5 Port seven

Following profile measurements are from port seven at a height of 992 mm.

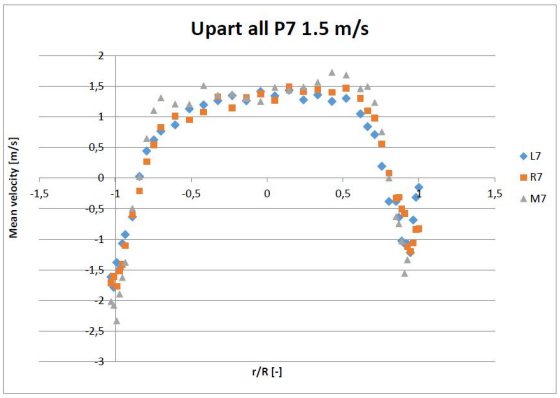

(a) Particle velocity.

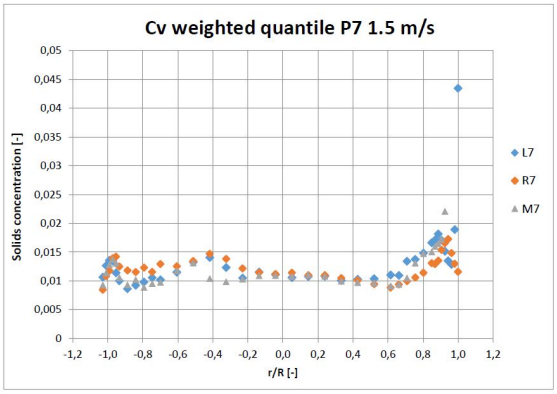

(b) Particle concentration.

Figure 47: Profile measurements at port seven with 1.5 m/s superficial gas velocity.

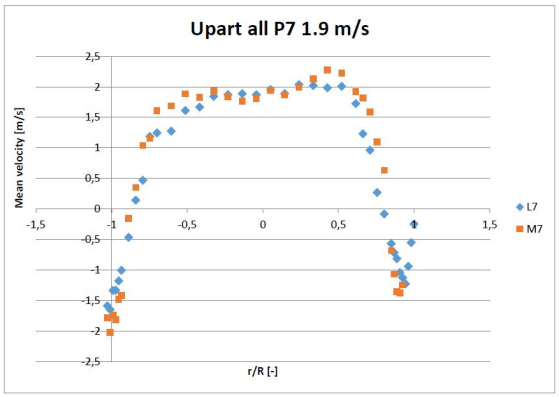

(a) Particle velocity.

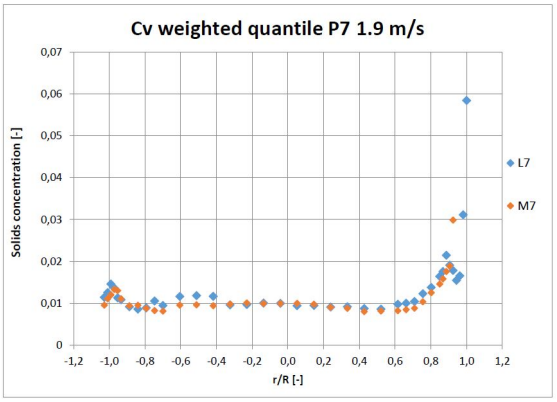

(b) Particle concentration.

Figure 48: Profile measurements at port seven with 1.9 m/s superficial gas velocity.

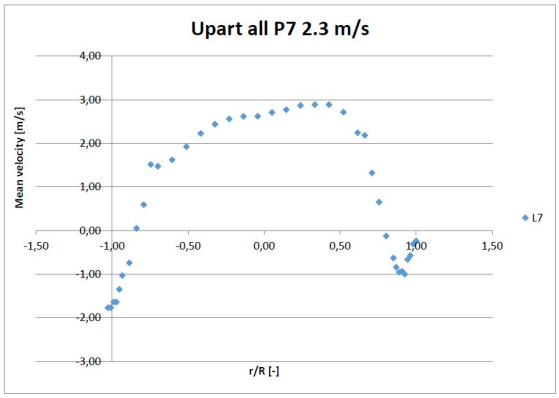

(a) Particle velocity.

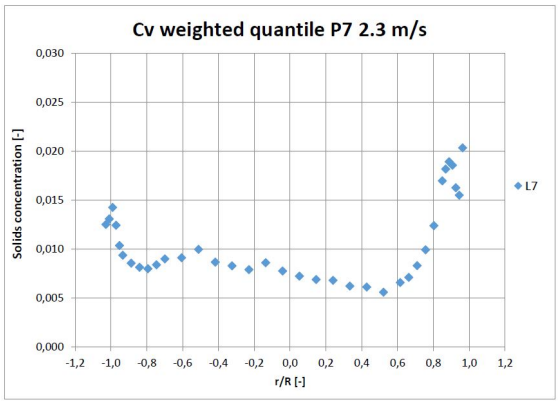

(b) Particle concentration.

Figure 49: Profile measurements at port seven with 1.9 m/s superficial gas velocity.

8.6 Port nine

Following profile measurements are from port nine at a height of 1580 mm.

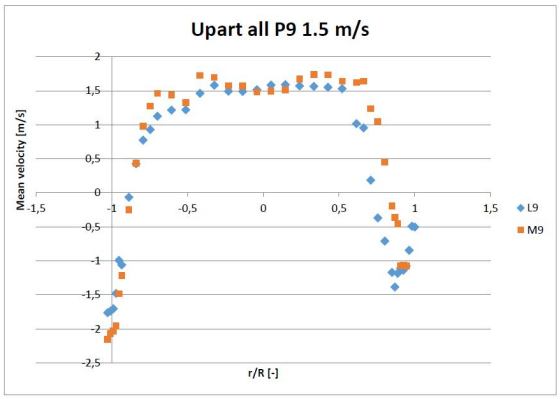

(a) Particle velocity.

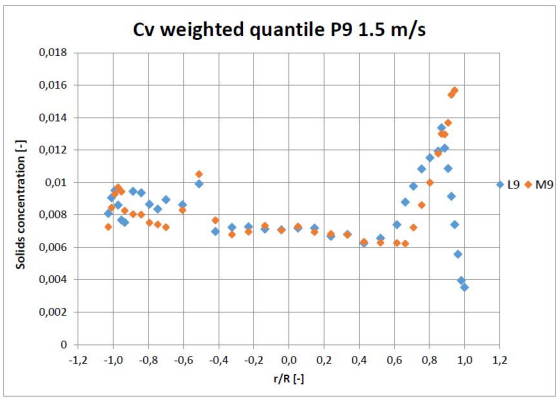

(b) Particle concentration.

Figure 50: Profile measurements at port nine with 1.5 m/s superficial gas velocity.

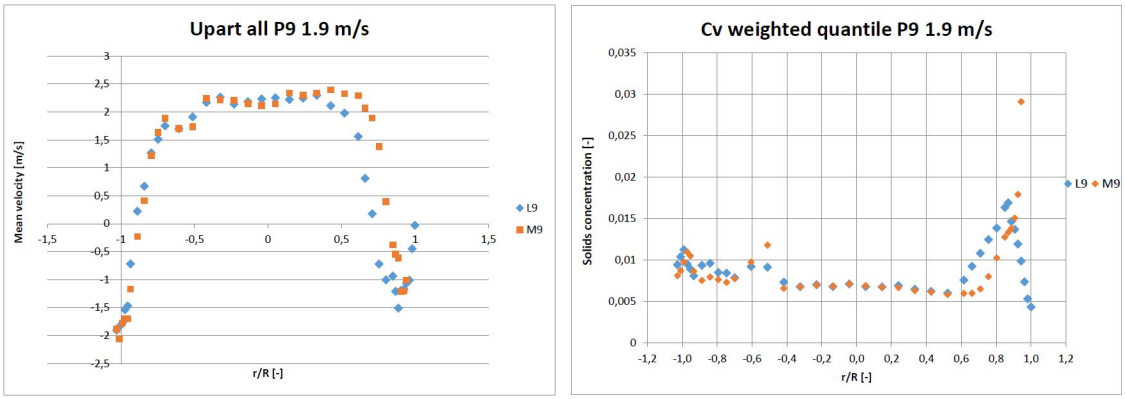

(a) Particle velocity. (b) Particle concentration.

Figure 51: Profile measurements at port nine with 1.9 m/s superficial gas velocity.

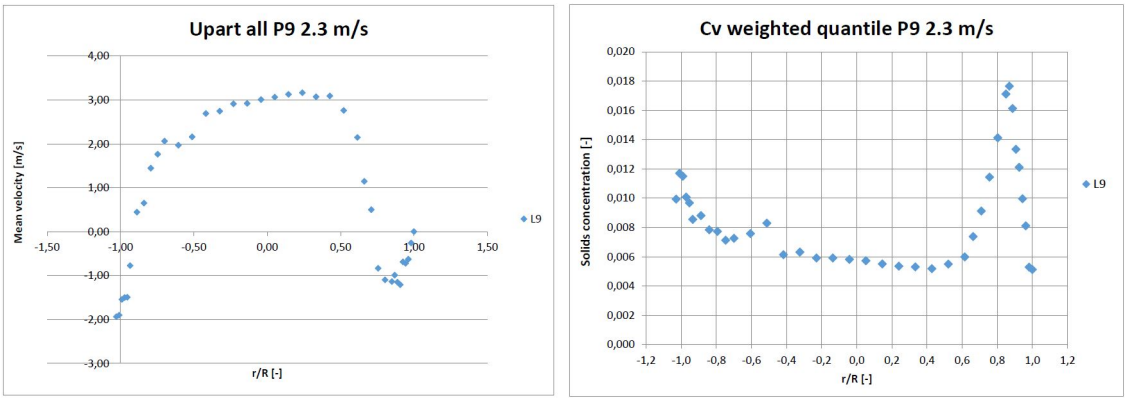

(a) Particle velocity. (b) Particle concentration.

Figure 52: Profile measurements at port nine with 1.9 m/s superficial gas velocity.

8.7 Port eleven

Following profile measurements are from port eleven at a height of 2262 mm.

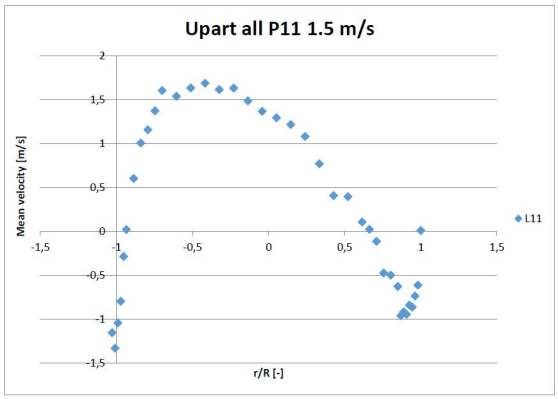

(a) Particle velocity.

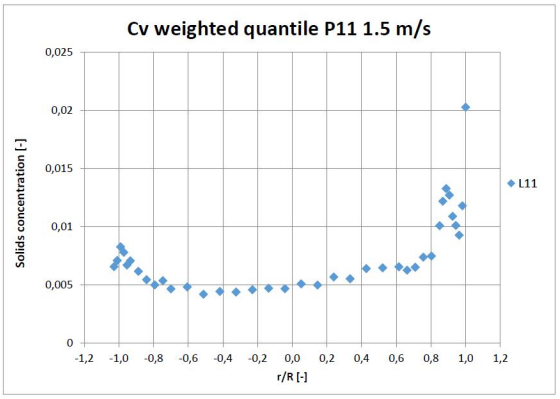

(b) Particle concentration.

Figure 53: Profile measurements at port eleven with 1.5 m/s superficial gas velocity.

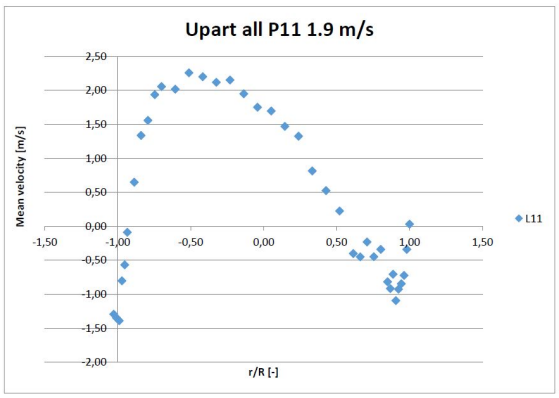

(a) Particle velocity.

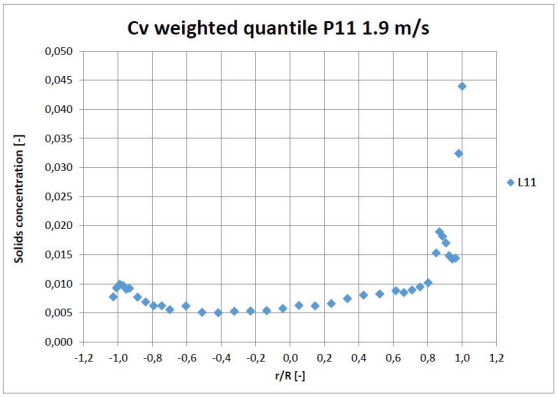

(b) Particle concentration.

Figure 54: Profile measurements at port eleven with 1.9 m/s superficial gas velocity.

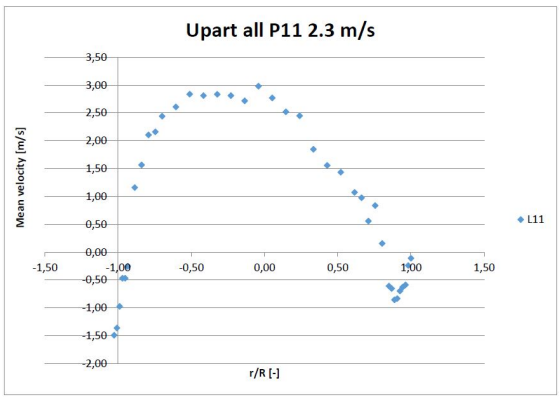

(a) Particle velocity.

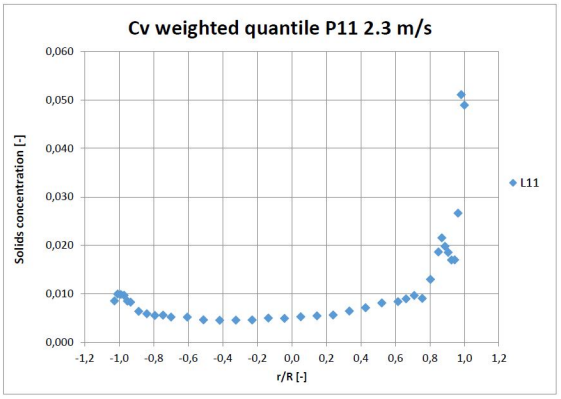

(b) Particle concentration.

Figure 55: Profile measurements at port eleven with 1.9 m/s superficial gas velocity.

9 Appendix 100-200 μm PSD probe results

Evaluated results from capacitance probe measurements inside a scaled, cold flow CFB model at Darmstadt Technical University. Figures showing profiles of glass microbeads with a size distribution of 100-200 μm for mean particle velocity and, for the two lowest measurement heights, constant weighted particle concentration. Figures for port four and higher shows the weighted quantile of particle concentrations instead. Measurement heights are according to table 25, with a total riser height of approximately 3.1 meters.

Table 25: Heights of the ports on the scaled cold flow CFB model.

Port	**P1**	**P2**	**P4**	**P7**	**P9**	**P11**
Height [mm]	124	248	496	992	1580	2262
h/H [-]	0.04	0.08	0.16	0.32	0.51	0.73

9.1 Compiled data

Results from glass microbeads with a size distribution of 100-200 μm compiled into figures of velocity, concentration and mass flux development across the riser. Note that the shown results are from port one to eleven. That is, from 124 mm to 2262 mm height and not the complete 3.1 m riser height.

9.1.1 Superficial gas velocity 1.9 m/s

Figures of velocity, concentration and mass flux development across the riser operating at 1.9 m/s superficial gas velocity.

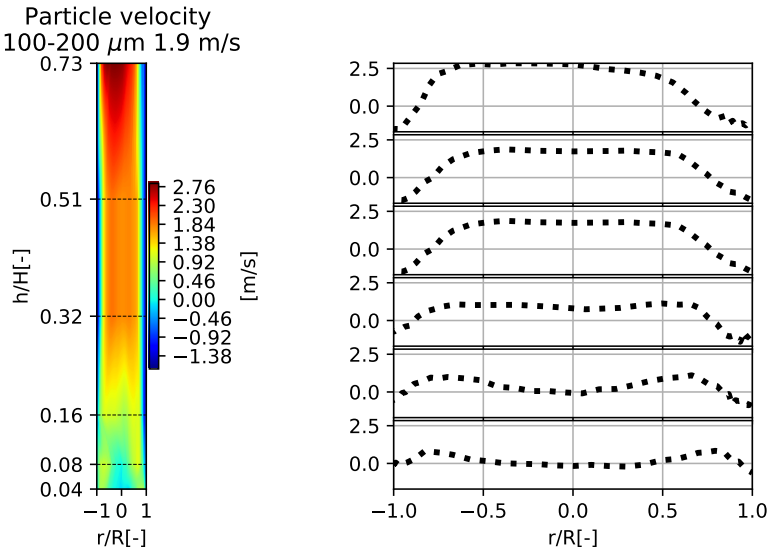

Figure 56: Particle velocity development across the riser.

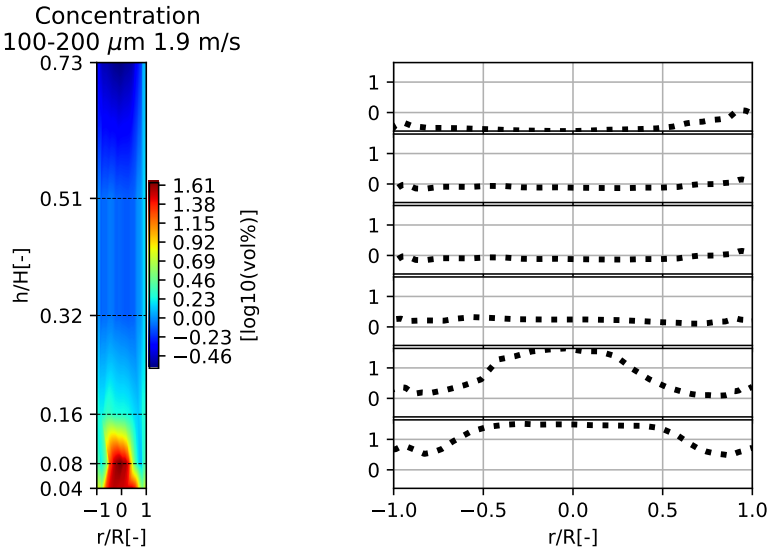

Figure 57: Particle volumetric concentration development across the riser.

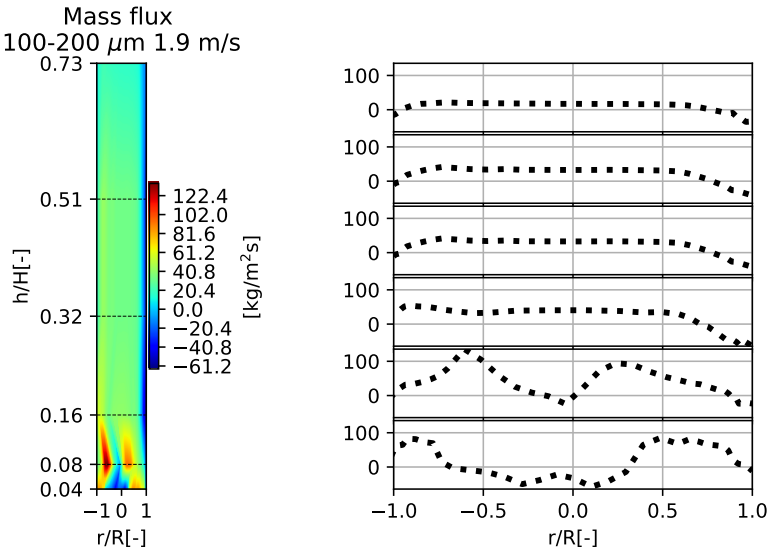

Figure 58: Particle mass flux development across the riser.

9.1.2 Superficial gas velocity 2.3 m/s

Figures of velocity, concentration and mass flux development across the riser operating at 2.3 m/s superficial gas velocity.

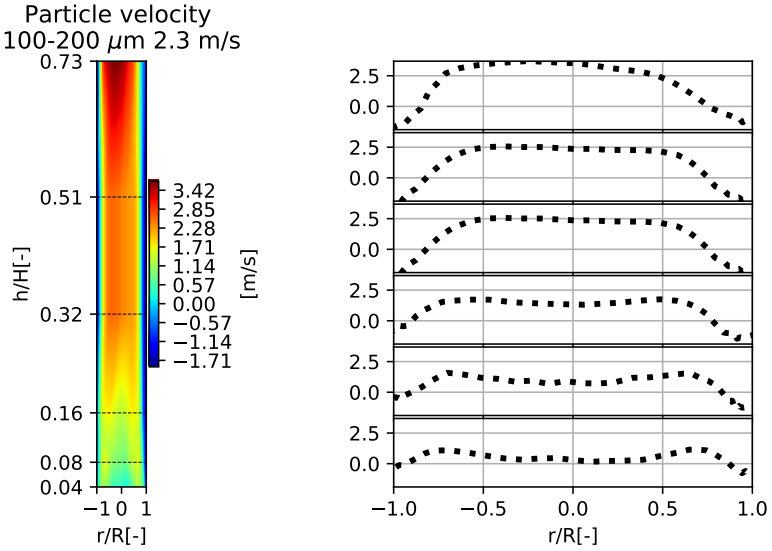

Figure 59: Particle velocity development across the riser.

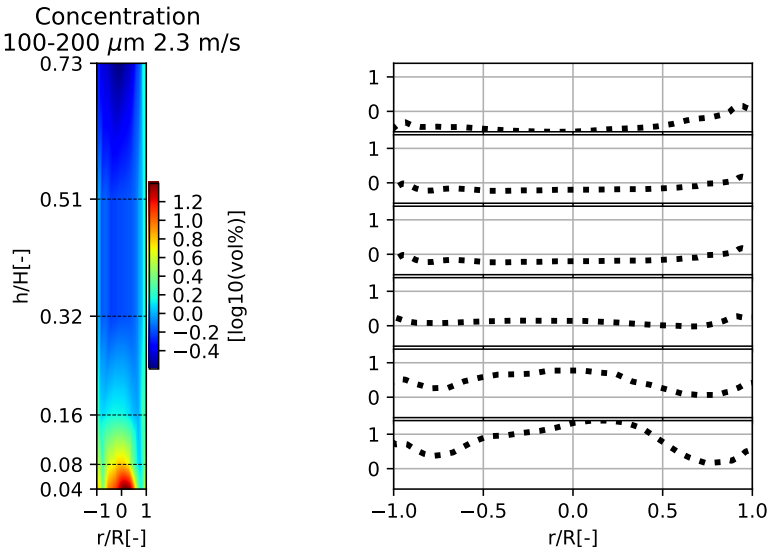

Figure 60: Particle volumetric concentration development across the riser.

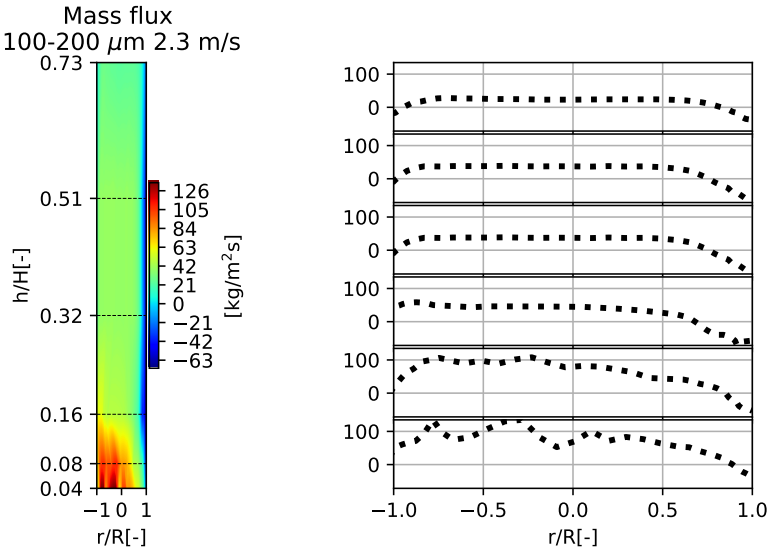

Figure 61: Particle mass flux development across the riser.

9.1.3 Superficial gas velocity 2.7 m/s

Figures of velocity, concentration and mass flux development across the riser operating at 2.7 m/s superficial gas velocity.

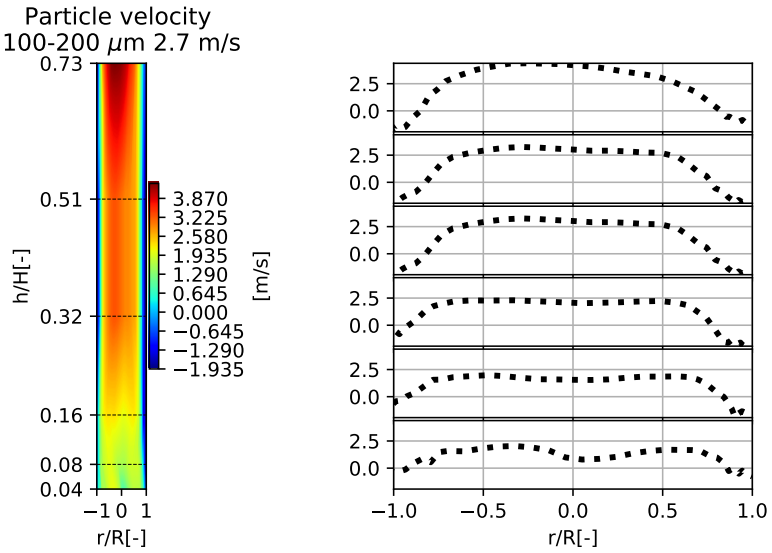

Figure 62: Particle velocity development across the riser.

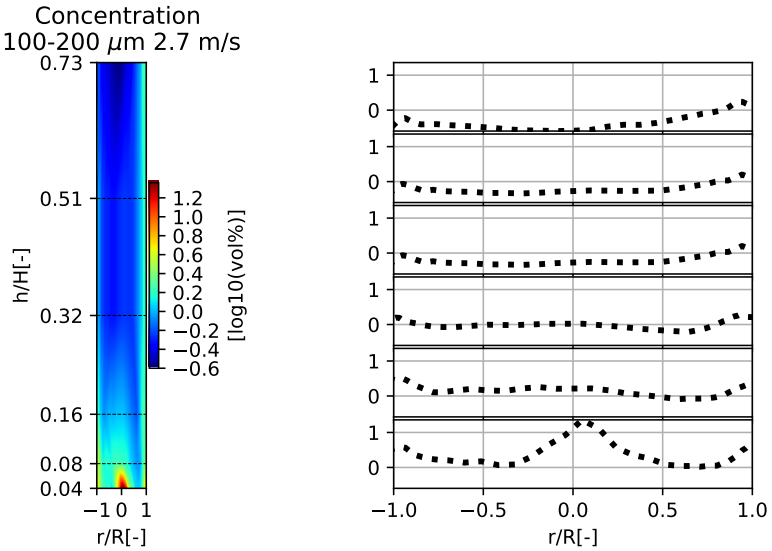

Figure 63: Particle volumetric concentration development across the riser.

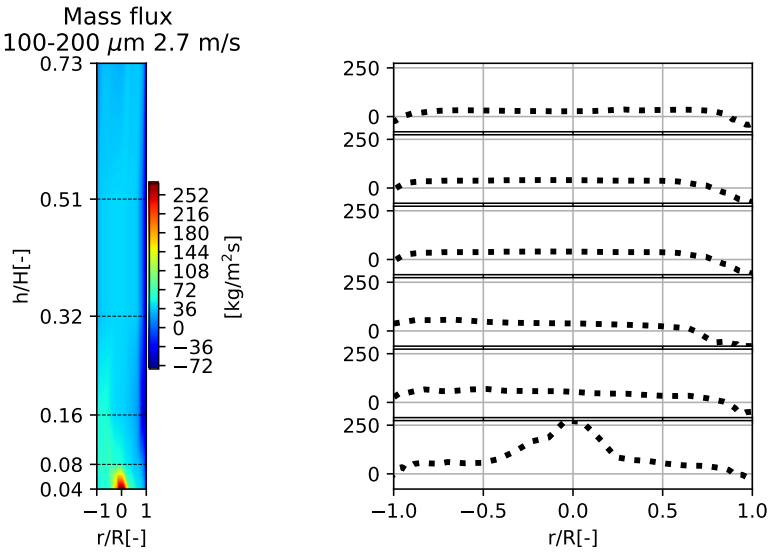

Figure 64: Particle mass flux development across the riser.

9.2 Port one

Following profile measurements are from port one at a height of 124 mm.

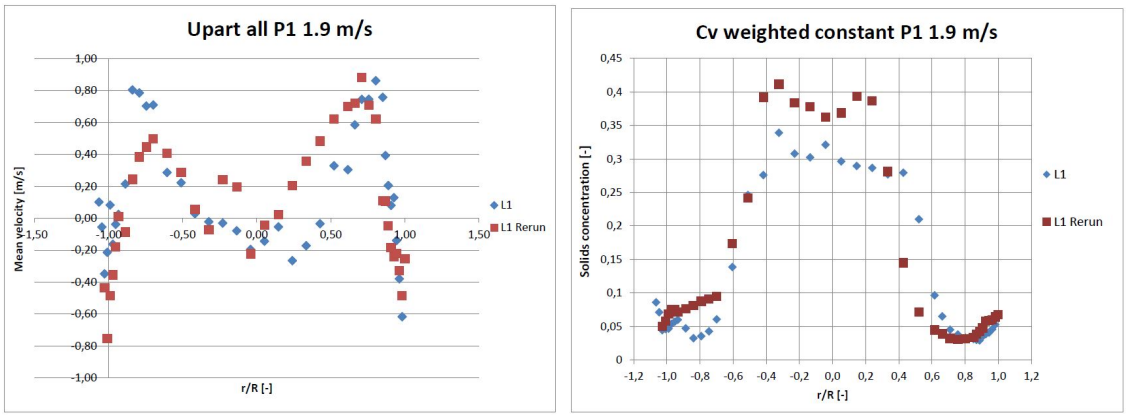

(a) Particle velocity.

(b) Particle concentration.

Figure 65: Profile measurements at port one with 1.9 m/s superficial gas velocity.

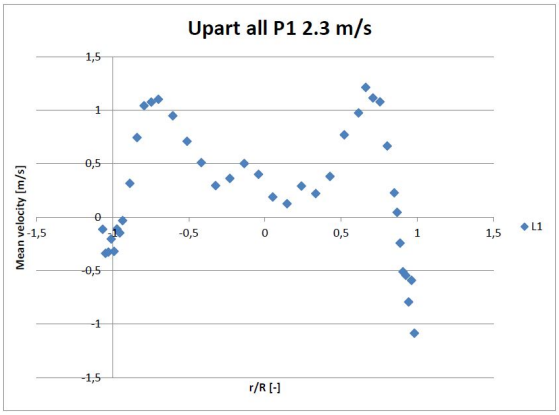

(a) Particle velocity.

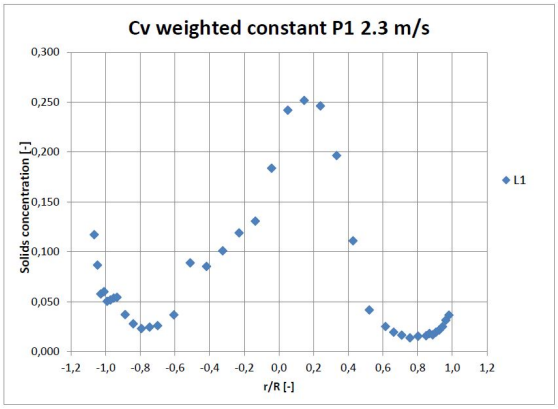

(b) Particle concentration.

Figure 66: Profile measurements at port one with 2,3 m/s superficial gas velocity.

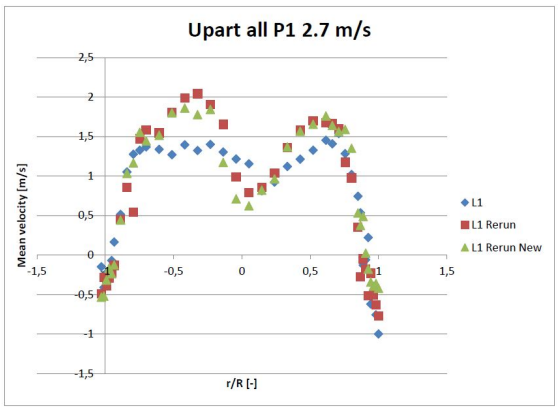

(a) Particle velocity.

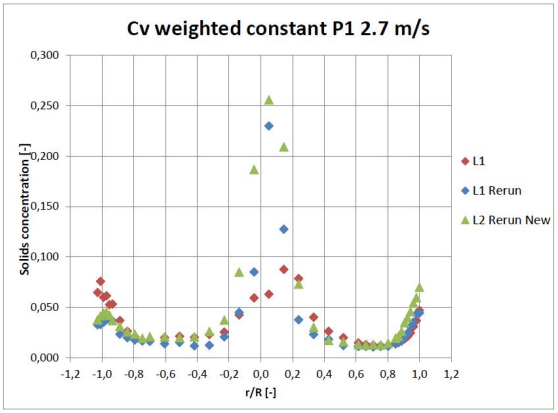

(b) Particle concentration.

Figure 67: Profile measurements at port one with 2,7 m/s superficial gas velocity.

9.3 Port two

Following profile measurements are from port two at a height of 248 mm.

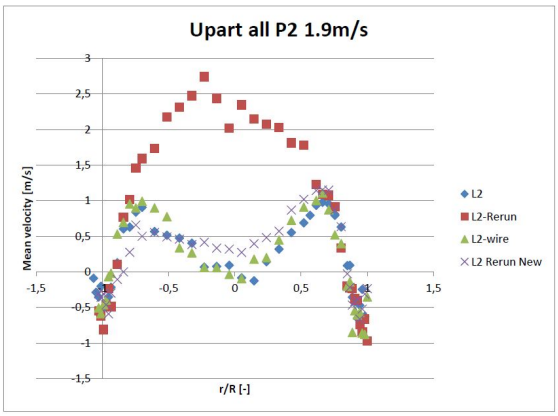

(a) Particle velocity.

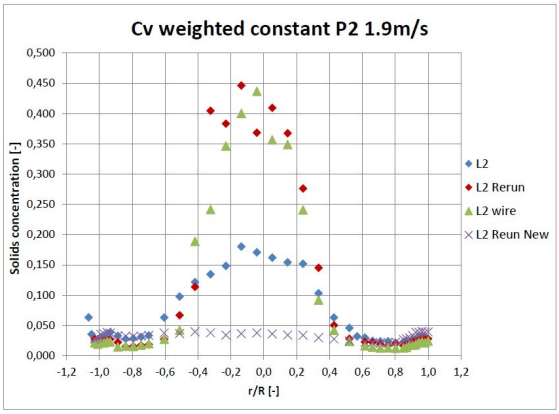

(b) Particle concentration.

Figure 68: Profile measurements at port two with 1.9 m/s superficial gas velocity.

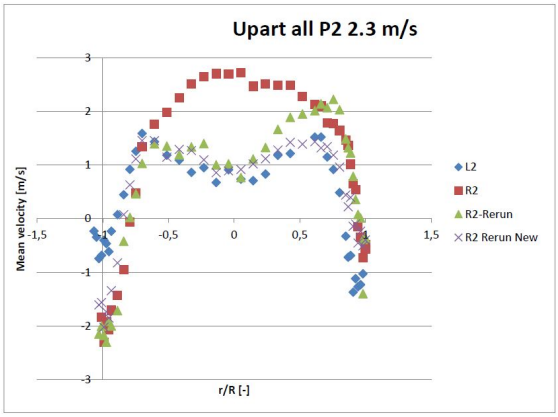

(a) Particle velocity.

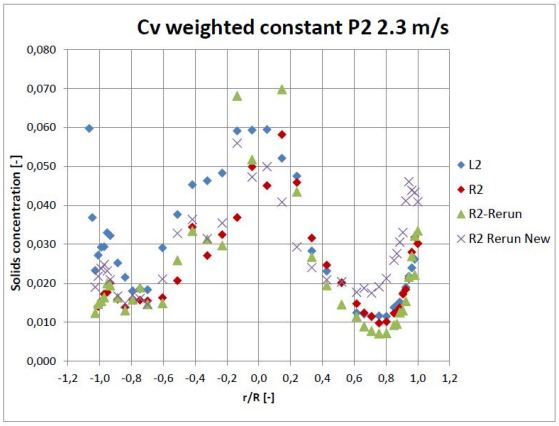

(b) Particle concentration.

Figure 69: Profile measurements at port two with 2,3 m/s superficial gas velocity.

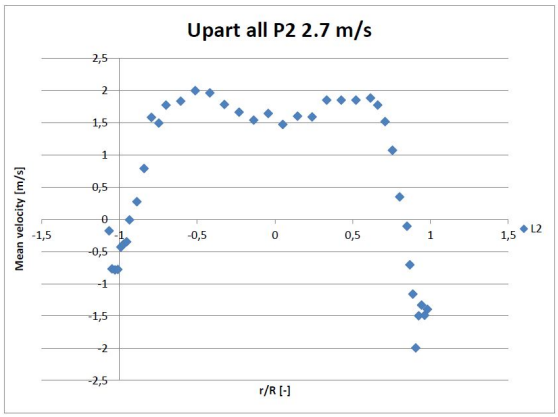

(a) Particle velocity.

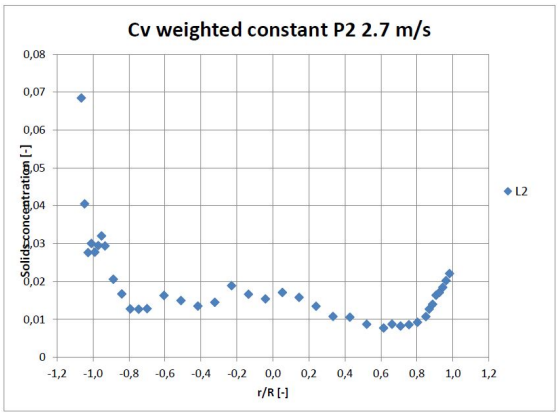

(b) Particle concentration.

Figure 70: Profile measurements at port two with 2,7 m/s superficial gas velocity.

9.4 Port four

Following profile measurements are from port four at a height of 496 mm.

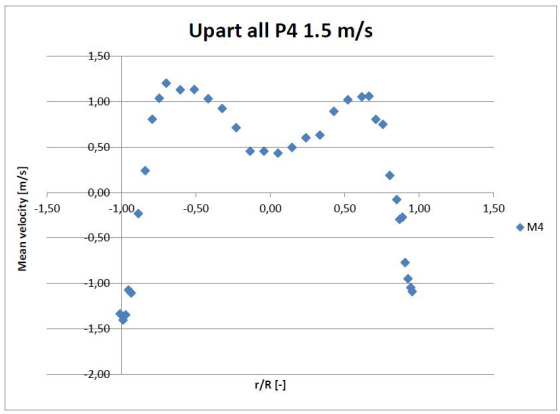

(a) Particle velocity.

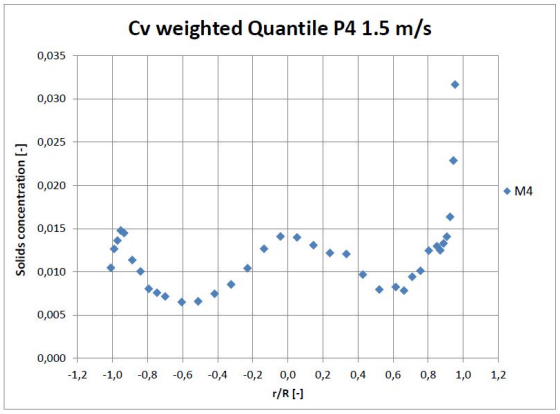

(b) Particle concentration.

Figure 71: Profile measurements at port four with 1.5 m/s superficial gas velocity.

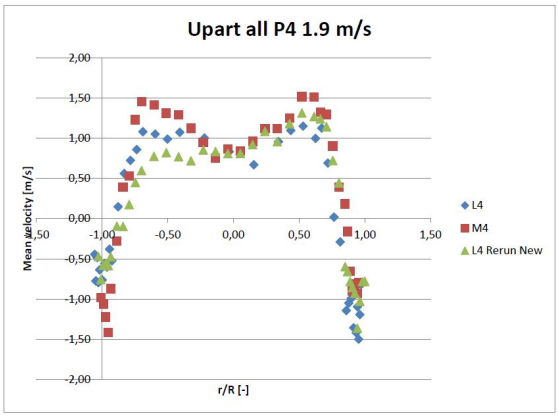

(a) Particle velocity.

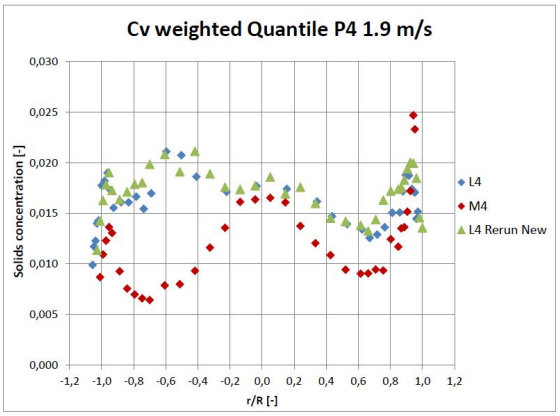

(b) Particle concentration.

Figure 72: Profile measurements at port four with 1.9 m/s superficial gas velocity.

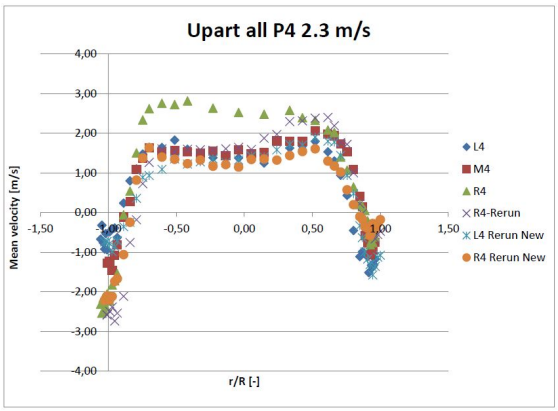

(a) Particle velocity.

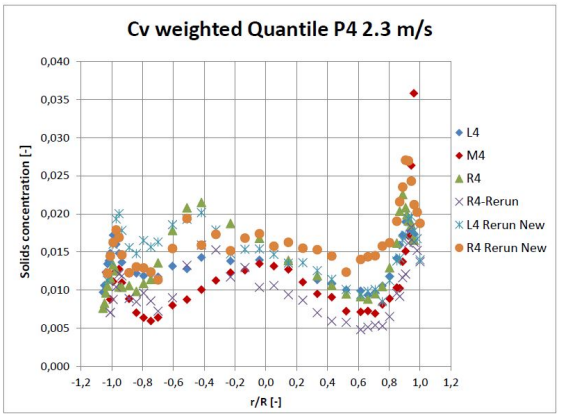

(b) Particle concentration.

Figure 73: Profile measurements at port four with 2,3 m/s superficial gas velocity.

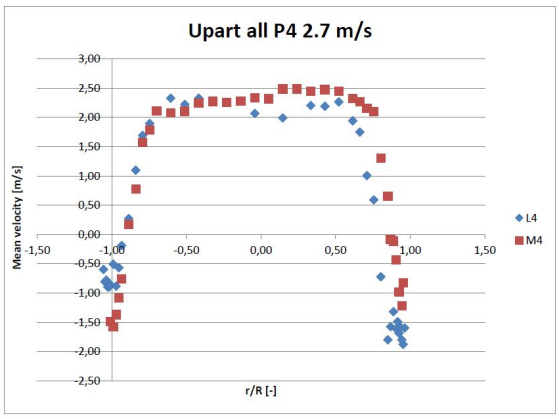

(a) Particle velocity.

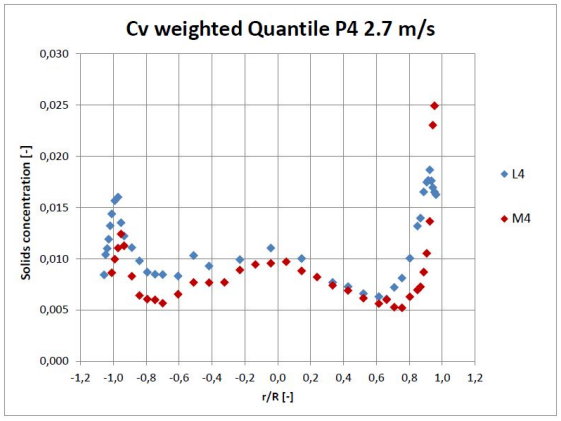

(b) Particle concentration.

Figure 74: Profile measurements at port four with 2,7 m/s superficial gas velocity.

9.5 Port seven

Following profile measurements are from port seven at a height of 992 mm.

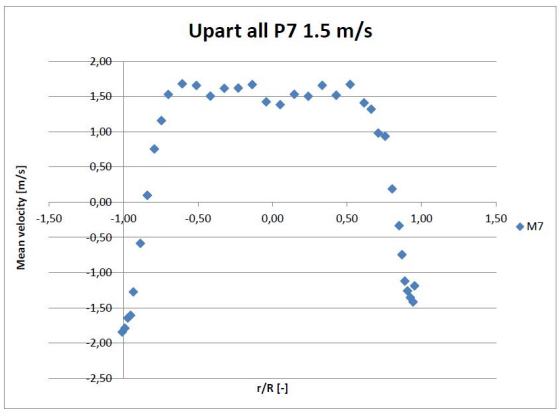

(a) Particle velocity.

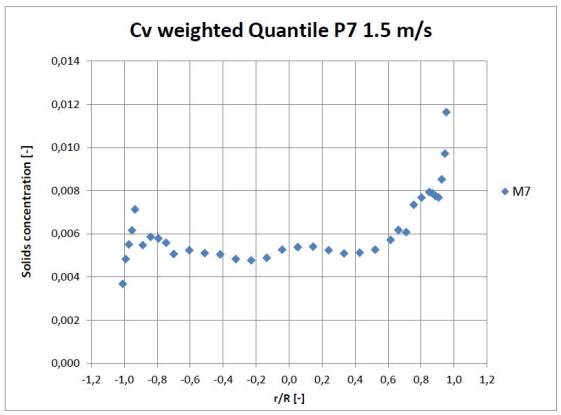

(b) Particle concentration.

Figure 75: Profile measurements at port seven with 1.5 m/s superficial gas velocity.

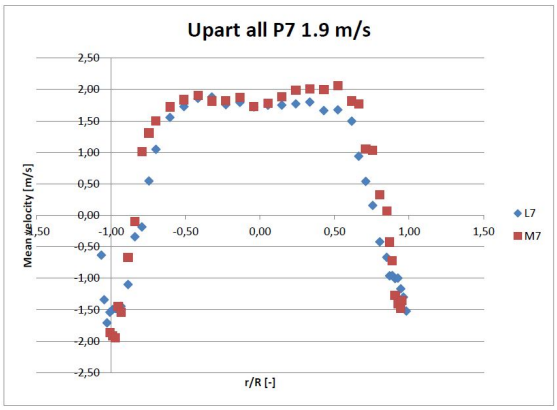

(a) Particle velocity.

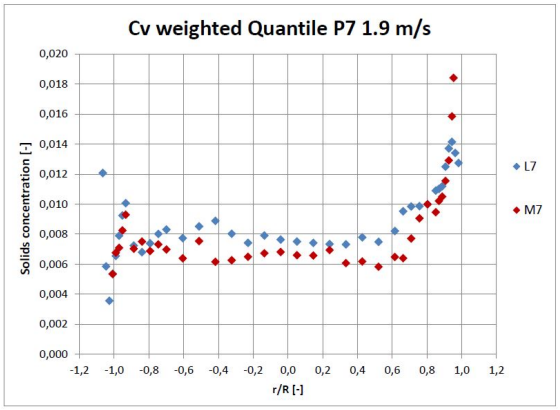

(b) Particle concentration.

Figure 76: Profile measurements at port seven with 1.9 m/s superficial gas velocity.

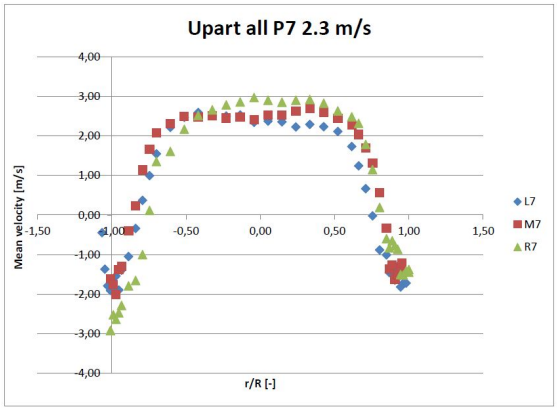

(a) Particle velocity.

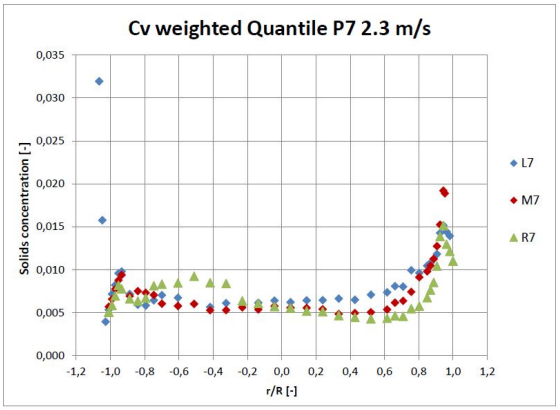

(b) Particle concentration.

Figure 77: Profile measurements at port seven with 2,3 m/s superficial gas velocity.

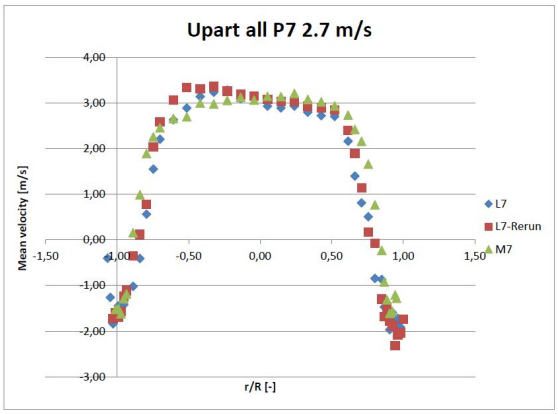

(a) Particle velocity.

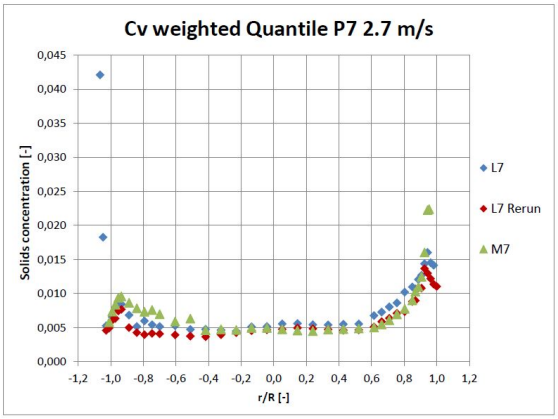

(b) Particle concentration.

Figure 78: Profile measurements at port seven with 2,7 m/s superficial gas velocity.

9.6 Port nine

Following profile measurements are from port nine at a height of 1580 mm.

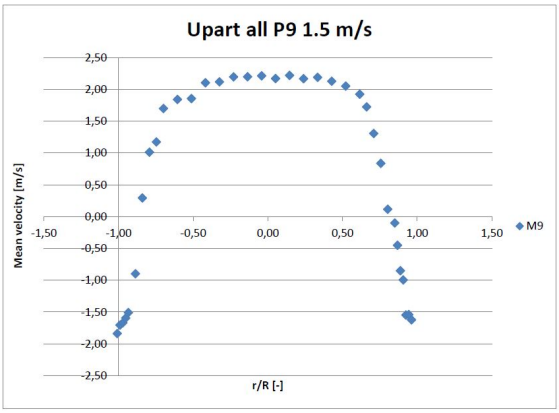

(a) Particle velocity.

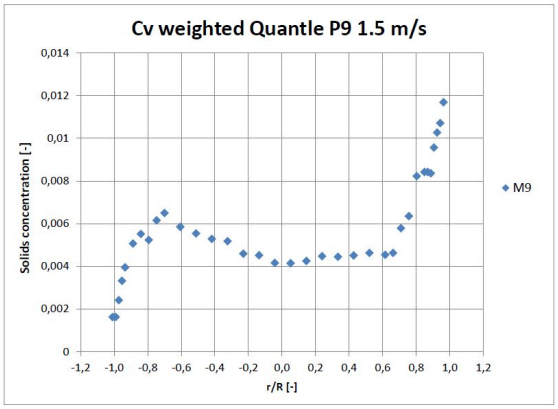

(b) Particle concentration.

Figure 79: Profile measurements at port nine with 1.5 m/s superficial gas velocity.

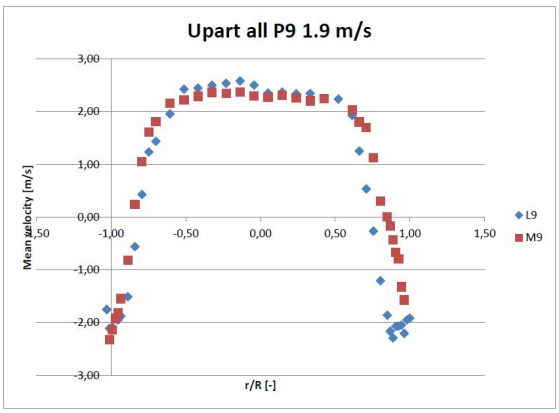

(a) Particle velocity.

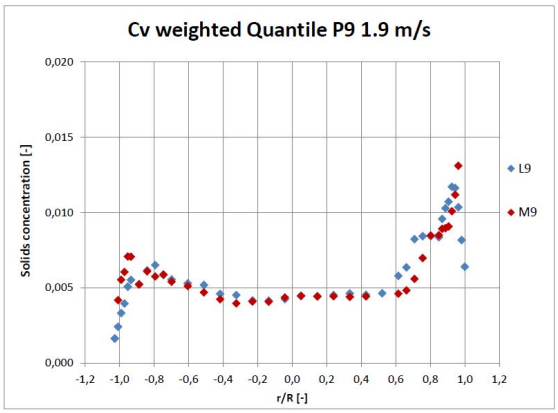

(b) Particle concentration.

Figure 80: Profile measurements at port nine with 1.9 m/s superficial gas velocity.

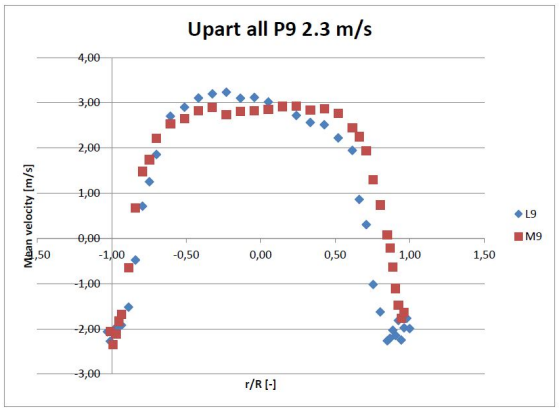

(a) Particle velocity.

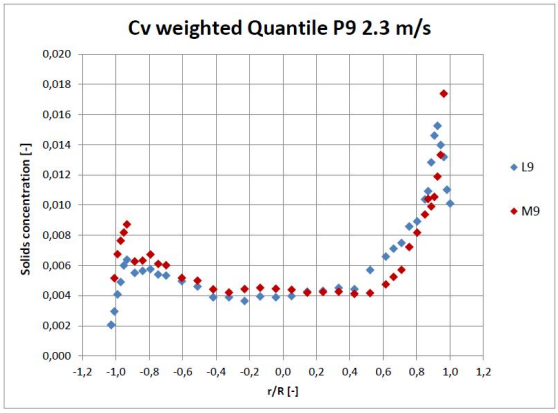

(b) Particle concentration.

Figure 81: Profile measurements at port nine with 2,3 m/s superficial gas velocity.

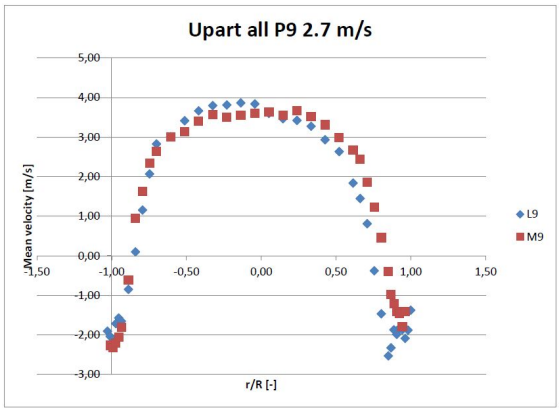

(a) Particle velocity.

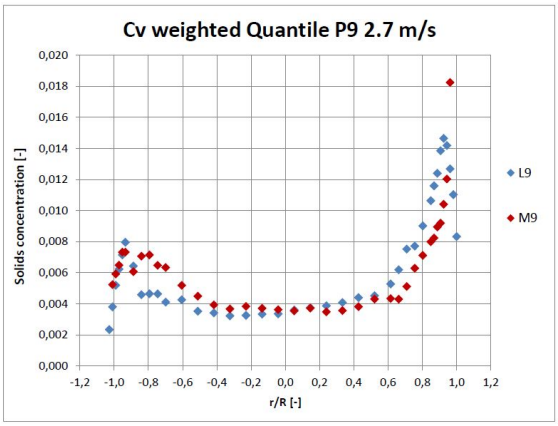

(b) Particle concentration.

Figure 82: Profile measurements at port nine with 2,7 m/s superficial gas velocity.

9.7 Port eleven

Following profile measurements are from port eleven at a height of 2262 mm.

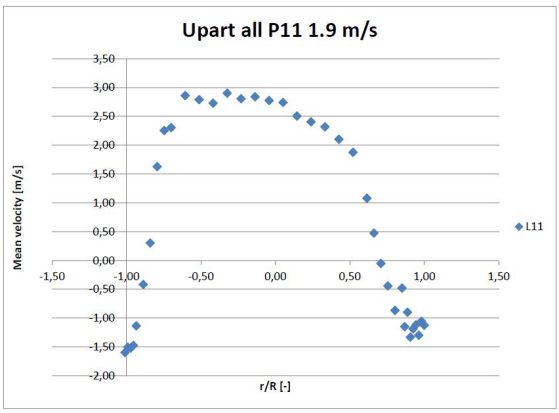

(a) Particle velocity.

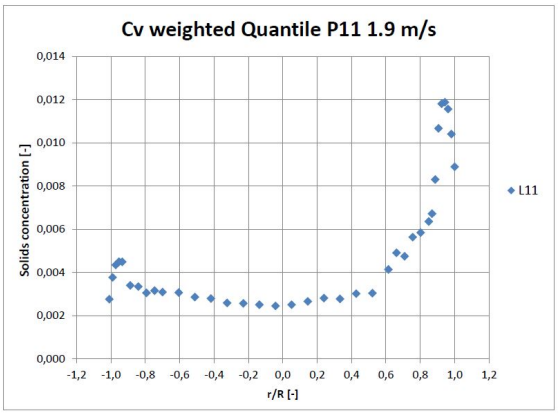

(b) Particle concentration.

Figure 83: Profile measurements at port eleven with 1.9 m/s superficial gas velocity.

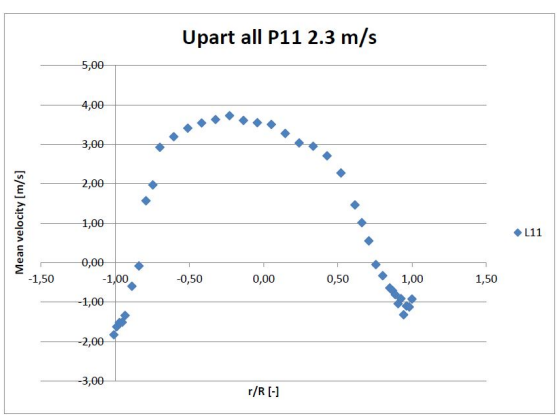

(a) Particle velocity.

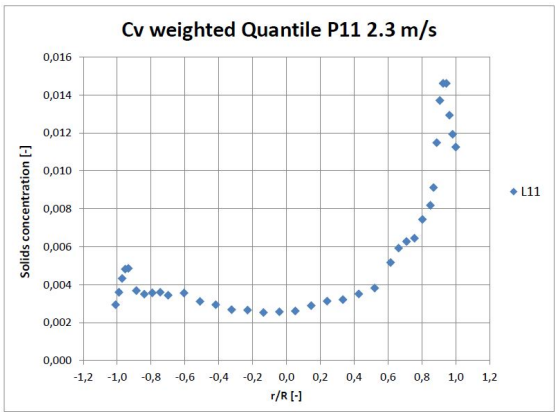

(b) Particle concentration.

Figure 84: Profile measurements at port eleven with 2,3 m/s superficial gas velocity.

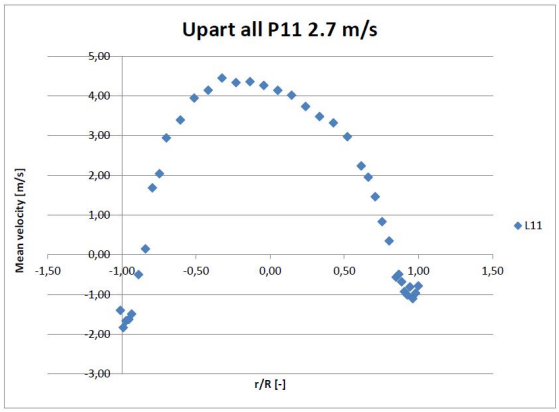

(a) Particle velocity.

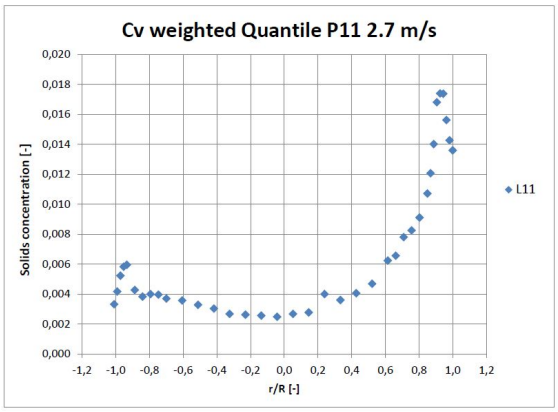

(b) Particle concentration.

Figure 85: Profile measurements at port eleven with 2,7 m/s superficial gas velocity.

10 Appendix 200-300 μm PSD probe results

Evaluated results from capacitance probe measurements inside a scaled, cold flow CFB model at Darmstadt Technical University. Figures showing profiles of glass microbeads with a size distribution of 200-300 μm for mean particle velocity and, for the two lowest measurement heights, constant weighted particle concentration. Figures for port four and higher shows the weighted quantile of particle concentrations instead. Measurement heights are according to table 26, with a total riser height of approximately 3.1 meters.

Table 26: Heights of the ports on the scaled cold flow CFB model.

Port	**P1**	**P2**	**P4**	**P7**	**P9**	**P11**
Height [mm]	124	248	496	992	1580	2262
h/H [-]	0.04	0.08	0.16	0.32	0.51	0.73

10.1 Compiled data

Results from glass microbeads with a size distribution of 200-300 μm compiled into figures of velocity, concentration and mass flux development across the riser. Note that the shown results are from port one to eleven. That is, from 124 mm to 2262 mm height and not the complete 3.1 m riser height.

10.1.1 Superficial gas velocity 1.9 m/s

Figures of velocity, concentration and mass flux development across the riser operating at 1.9 m/s superficial gas velocity.

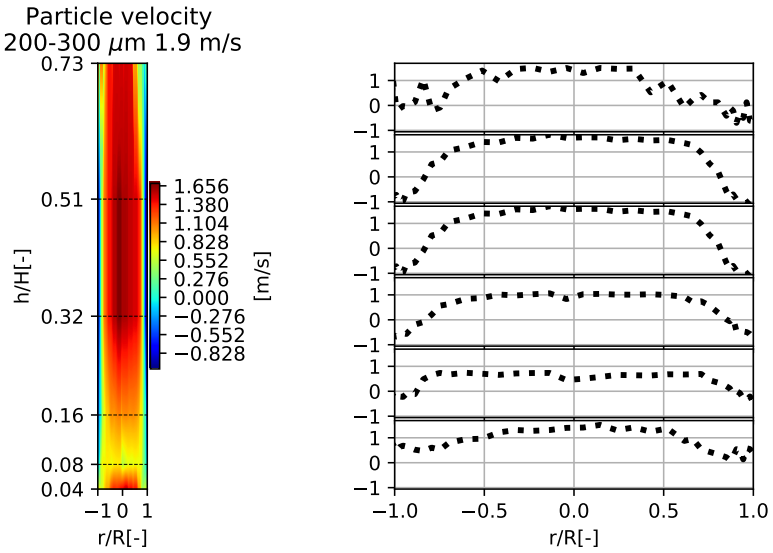

Figure 86: Particle velocity development across the riser.

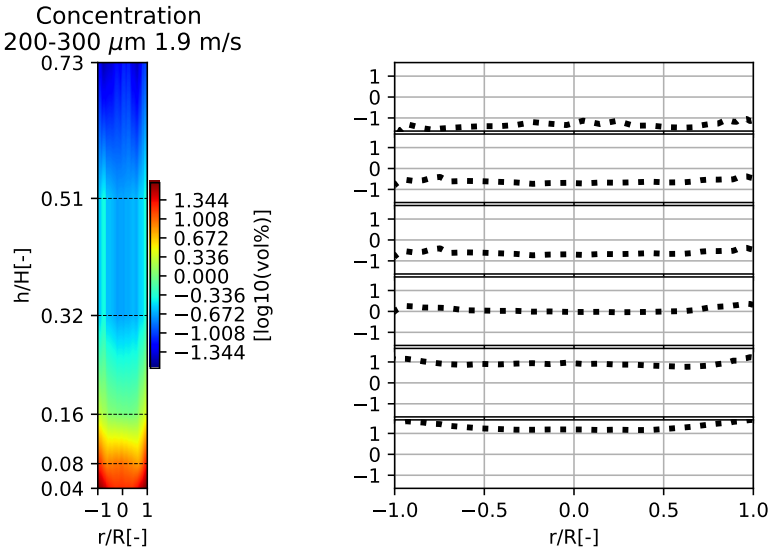

Figure 87: Particle volumetric concentration development across the riser.

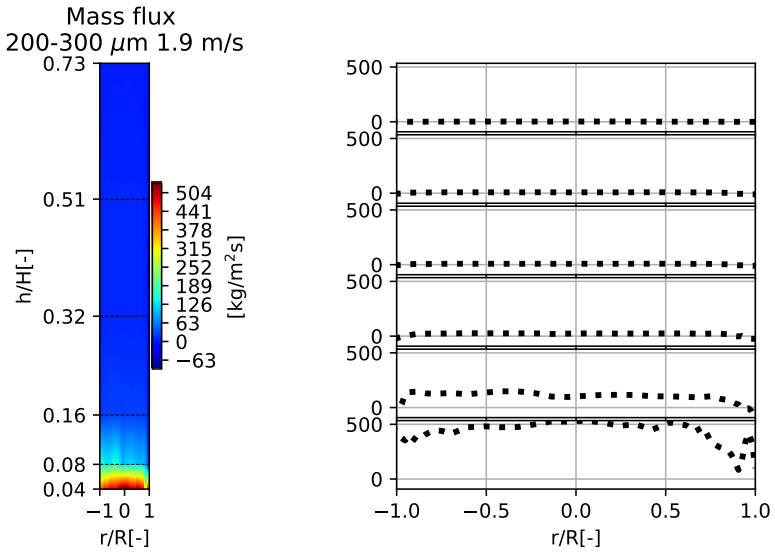

Figure 88: Particle mass flux development across the riser.

10.1.2 Superficial gas velocity 2.3 m/s

Figures of velocity, concentration and mass flux development across the riser operating at 2.3 m/s superficial gas velocity.

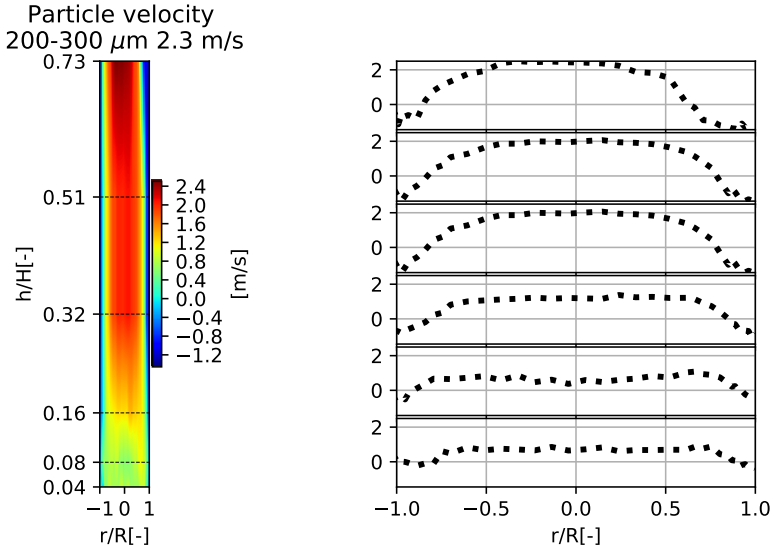

Figure 89: Particle velocity development across the riser.

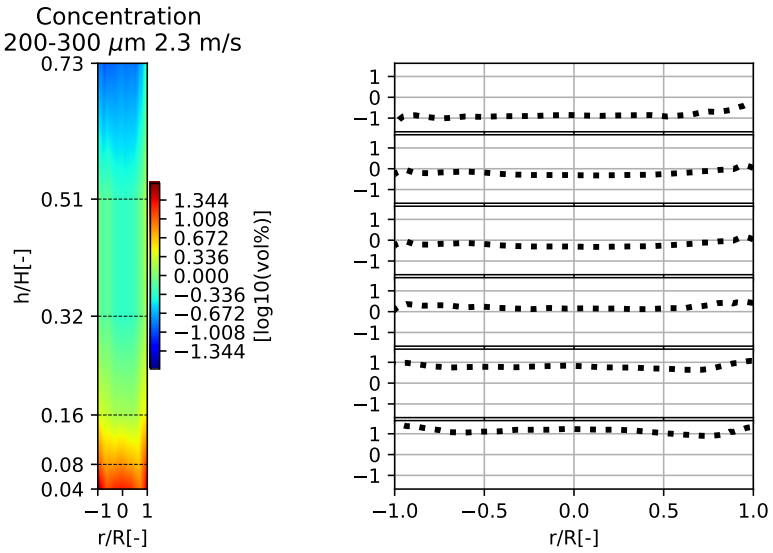

Figure 90: Particle volumetric concentration development across the riser.

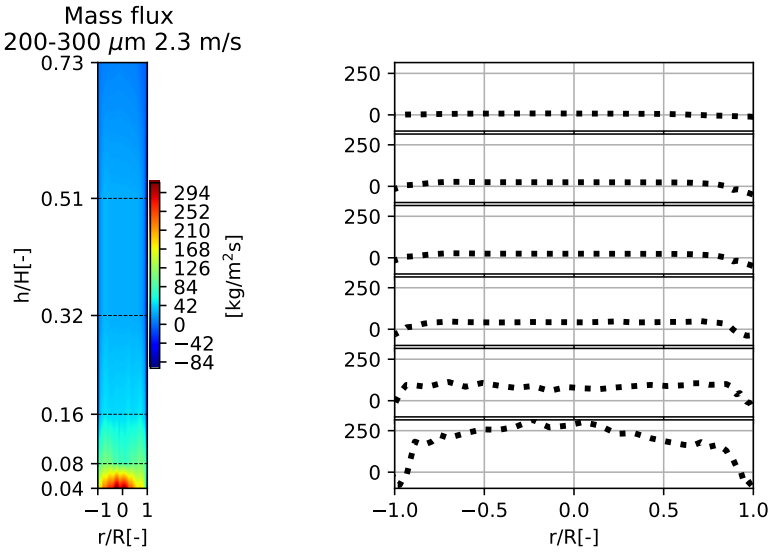

Figure 91: Particle mass flux development across the riser.

10.1.3 Superficial gas velocity 2.7 m/s

Figures of velocity, concentration and mass flux development across the riser operating at 2.7 m/s superficial gas velocity.

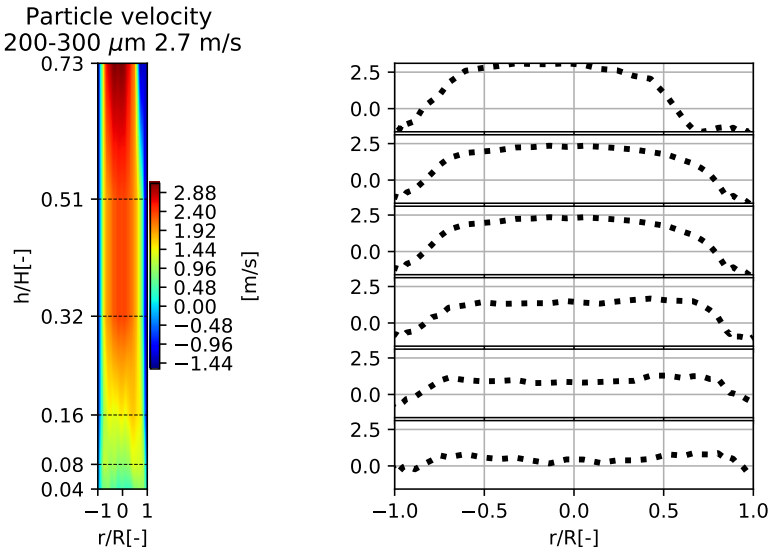

Figure 92: Particle velocity development across the riser.

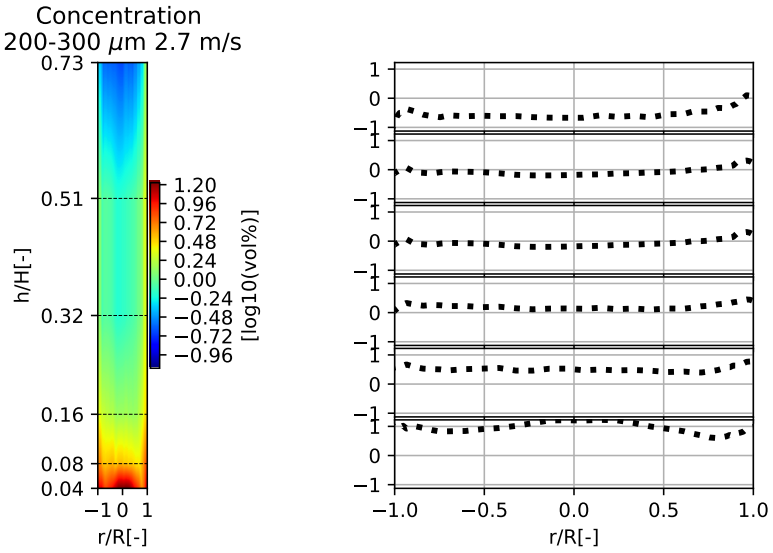

Figure 93: Particle volumetric concentration development across the riser.

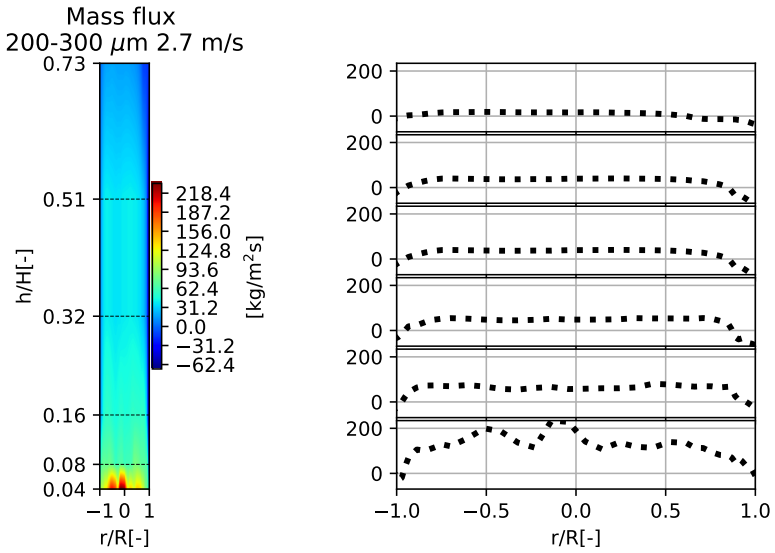

Figure 94: Particle mass flux development across the riser.

10.2 Port one

Following profile measurements are from port one at a height of 124 mm.

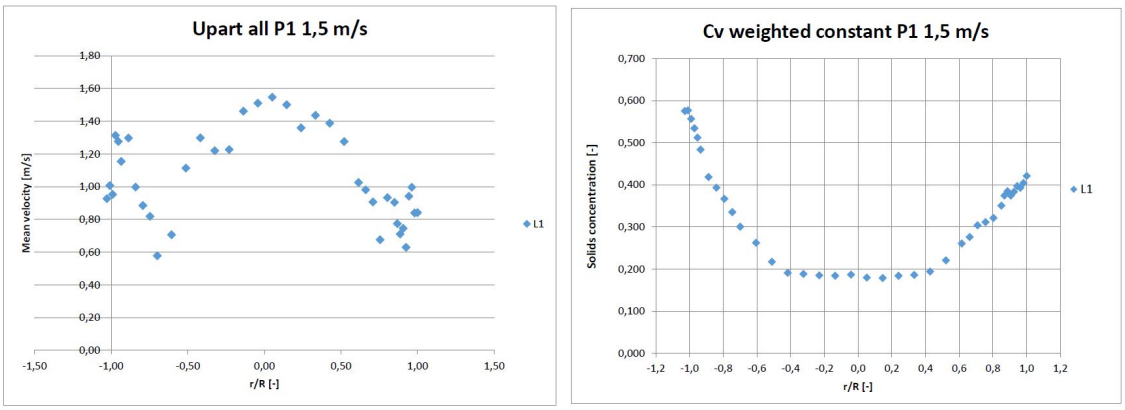

(a) Particle velocity.

(b) Particle concentration.

Figure 95: Profile measurements at port one with 1.5 m/s superficial gas velocity.

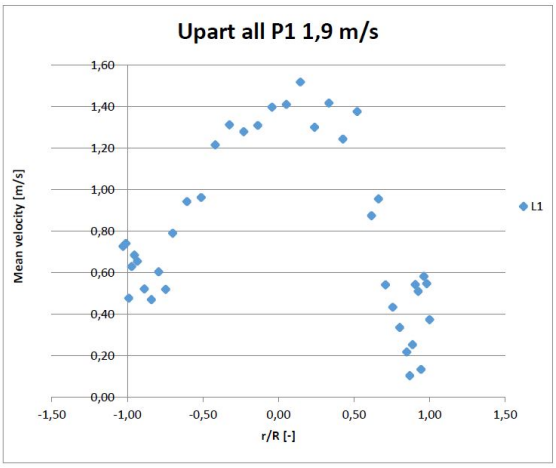

(a) Particle velocity.

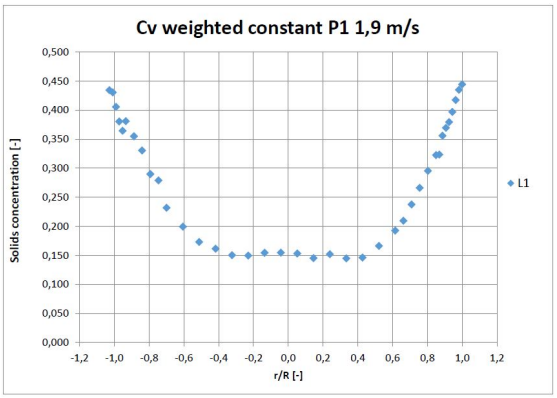

(b) Particle concentration.

Figure 96: Profile measurements at port one with 1.9 m/s superficial gas velocity.

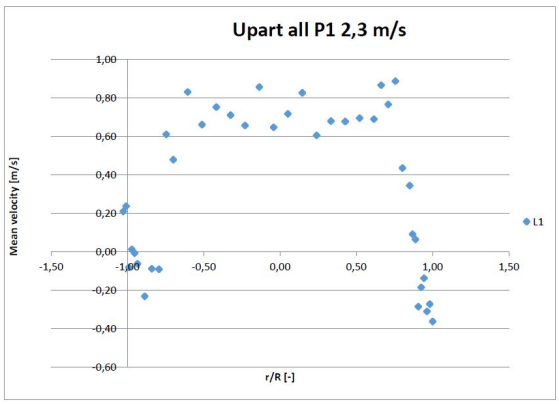

(a) Particle velocity.

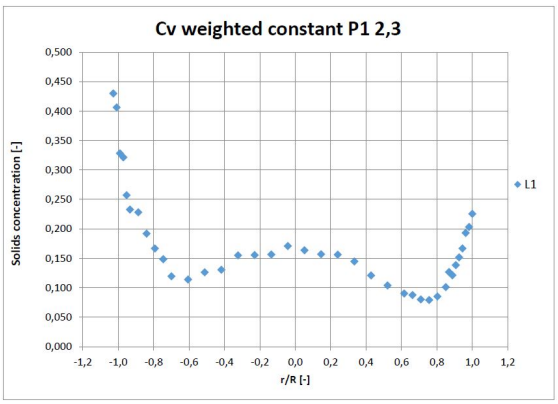

(b) Particle concentration.

Figure 97: Profile measurements at port one with 2.3 m/s superficial gas velocity.

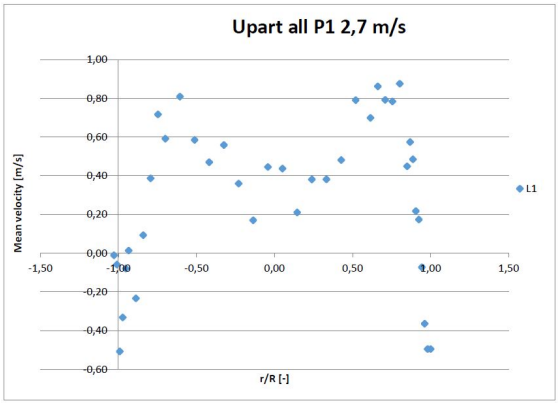

(a) Particle velocity.

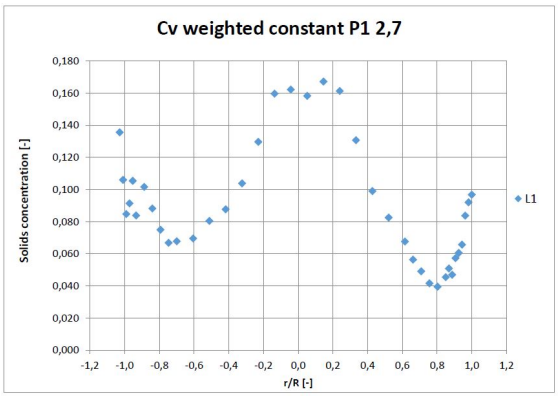

(b) Particle concentration.

Figure 98: Profile measurements at port one with 2.7 m/s superficial gas velocity.

10.3 Port two

Following profile measurements are from port two at a height of 248 mm.

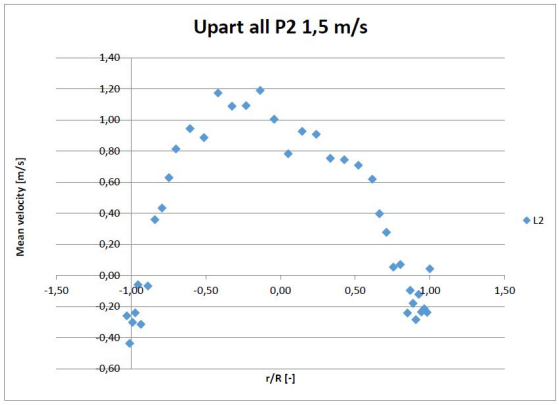

(a) Particle velocity.

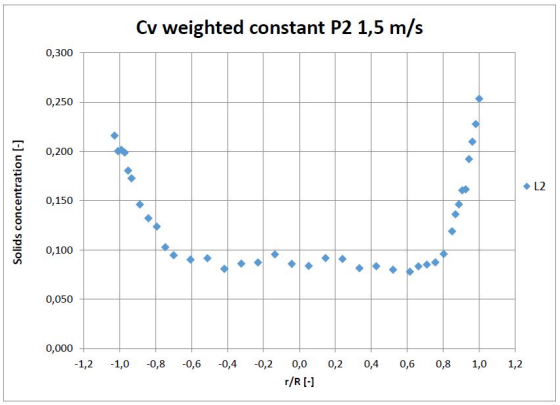

(b) Particle concentration.

Figure 99: Profile measurements at port two with 1.5 m/s superficial gas velocity.

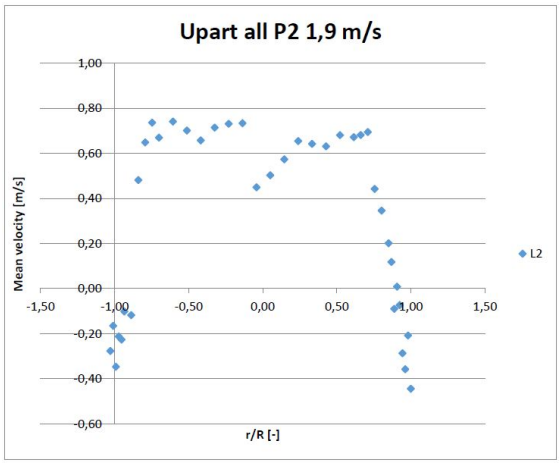

(a) Particle velocity.

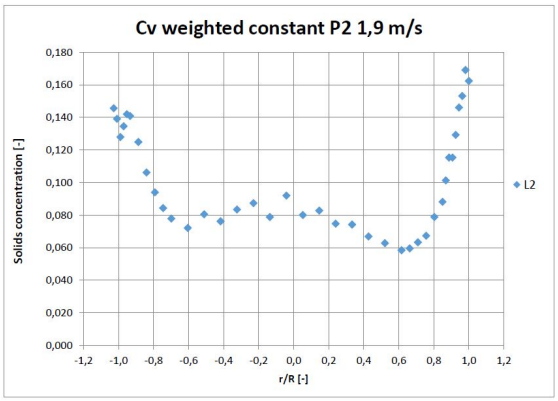

(b) Particle concentration.

Figure 100: Profile measurements at port two with 1.9 m/s superficial gas velocity.

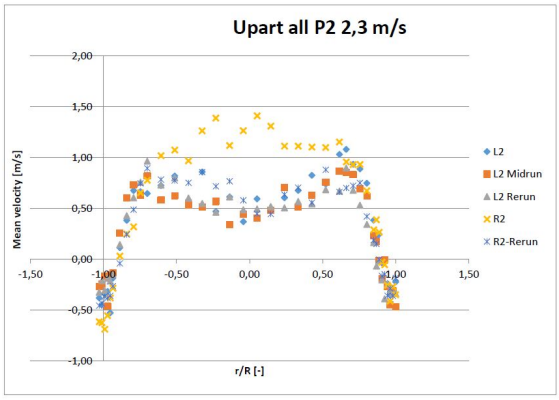

(a) Particle velocity.

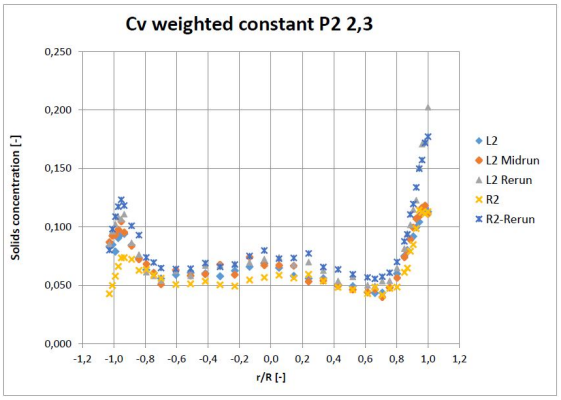

(b) Particle concentration.

Figure 101: Profile measurements at port two with 2.3 m/s superficial gas velocity.

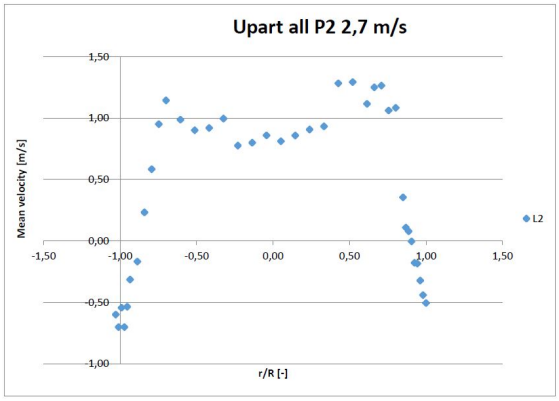

(a) Particle velocity.

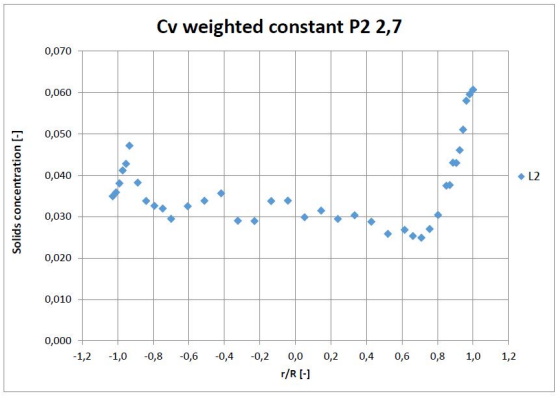

(b) Particle concentration.

Figure 102: Profile measurements at port two with 2.7 m/s superficial gas velocity.

10.4 Port four

Following profile measurements are from port four at a height of 496 mm.

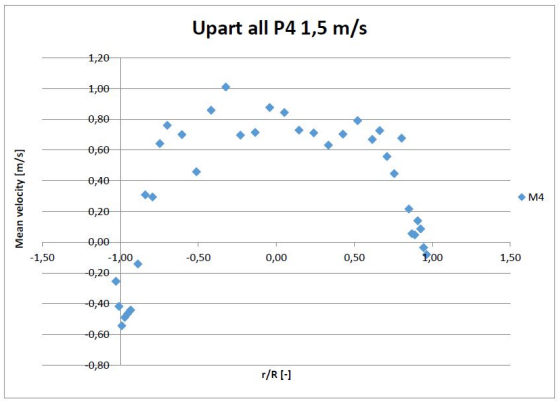

(a) Particle velocity.

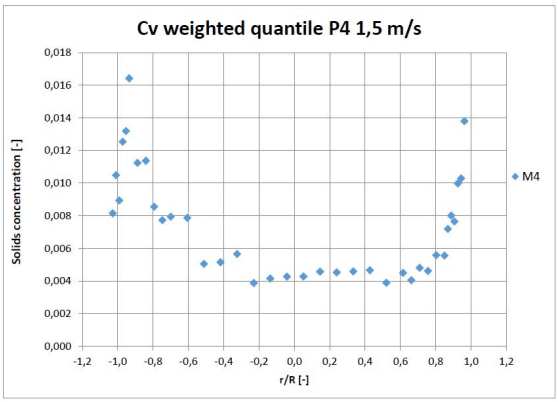

(b) Particle concentration.

Figure 103: Profile measurements at port four with 1.5 m/s superficial gas velocity.

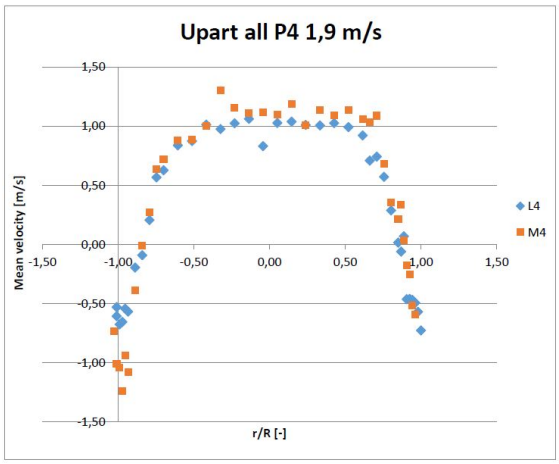

(a) Particle velocity.

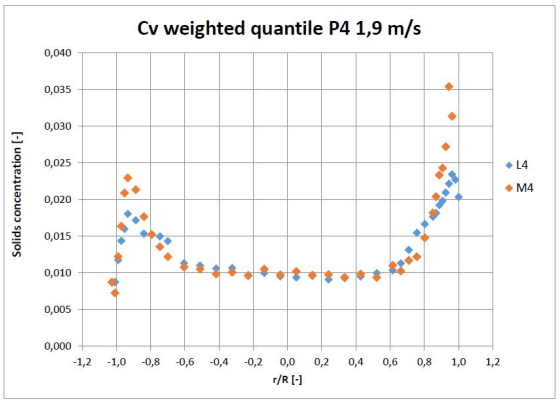

(b) Particle concentration.

Figure 104: Profile measurements at port four with 1.9 m/s superficial gas velocity.

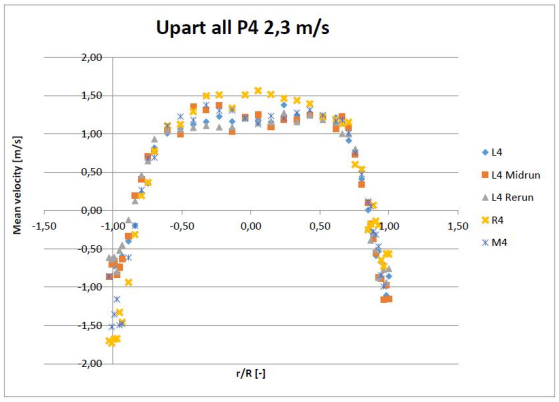

(a) Particle velocity.

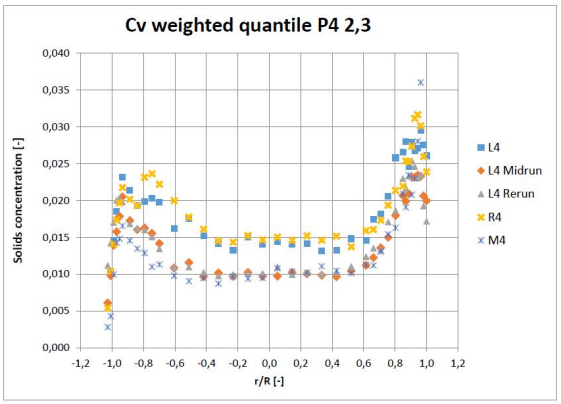

(b) Particle concentration.

Figure 105: Profile measurements at port four with 2.3 m/s superficial gas velocity.

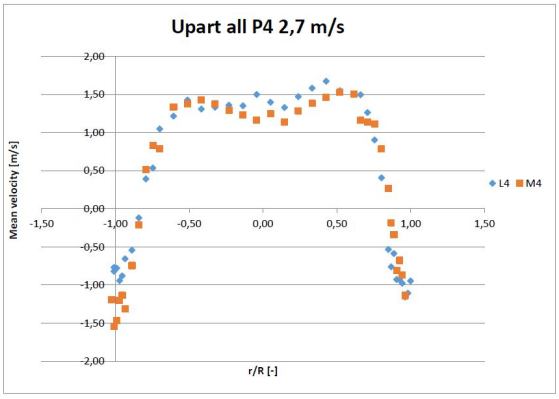

(a) Particle velocity.

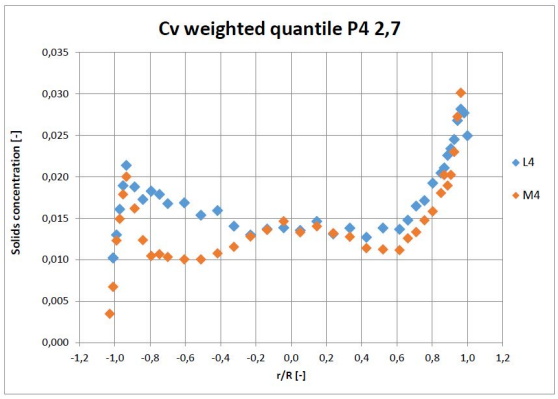

(b) Particle concentration.

Figure 106: Profile measurements at port four with 2.7 m/s superficial gas velocity.

10.5 Port seven

Following profile measurements are from port seven at a height of 992 mm.

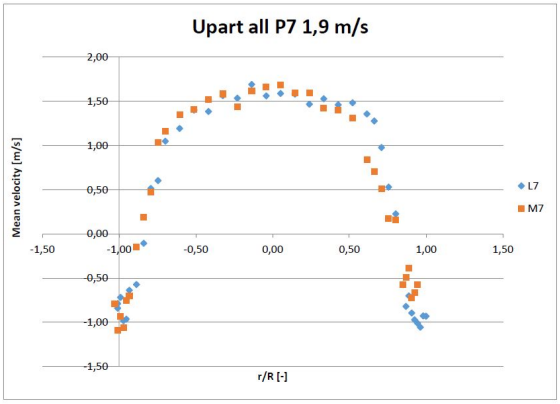

(a) Particle velocity.

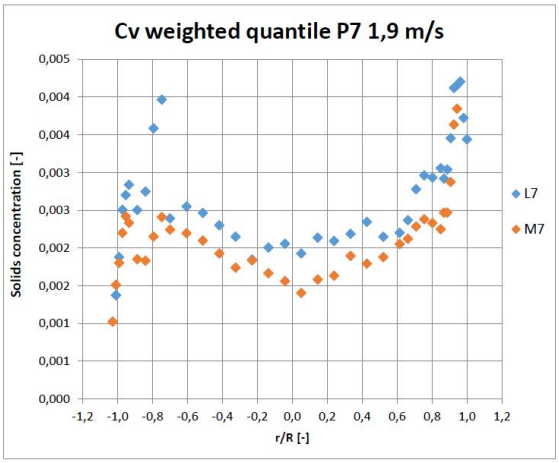

(b) Particle concentration.

Figure 107: Profile measurements at port seven with 1.9 m/s superficial gas velocity.

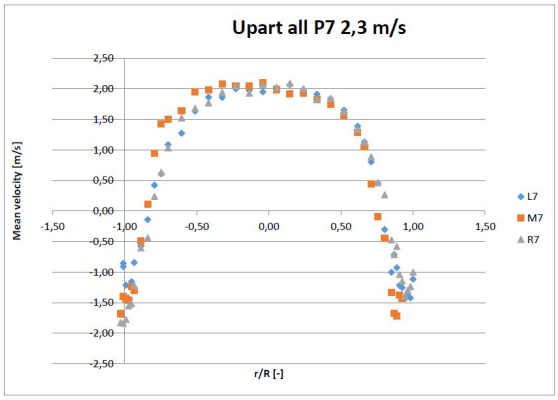

(a) Particle velocity.

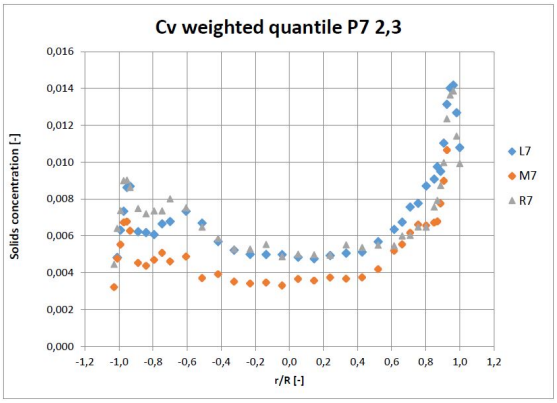

(b) Particle concentration.

Figure 108: Profile measurements at port seven with 2.3 m/s superficial gas velocity.

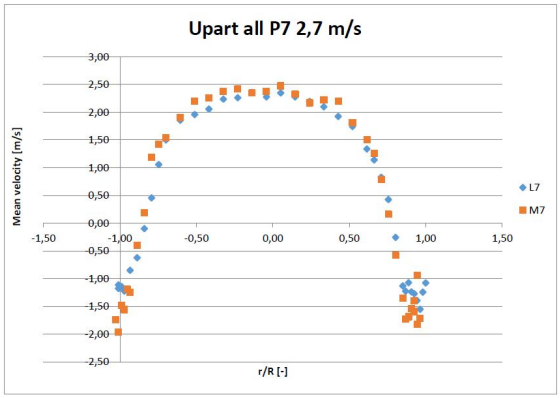

(a) Particle velocity.

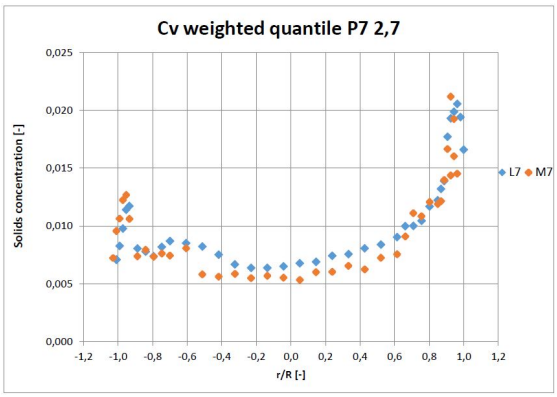

(b) Particle concentration.

Figure 109: Profile measurements at port seven with 2.7 m/s superficial gas velocity.

10.6 Port nine

Following profile measurements are from port nine at a height of 1580 mm.

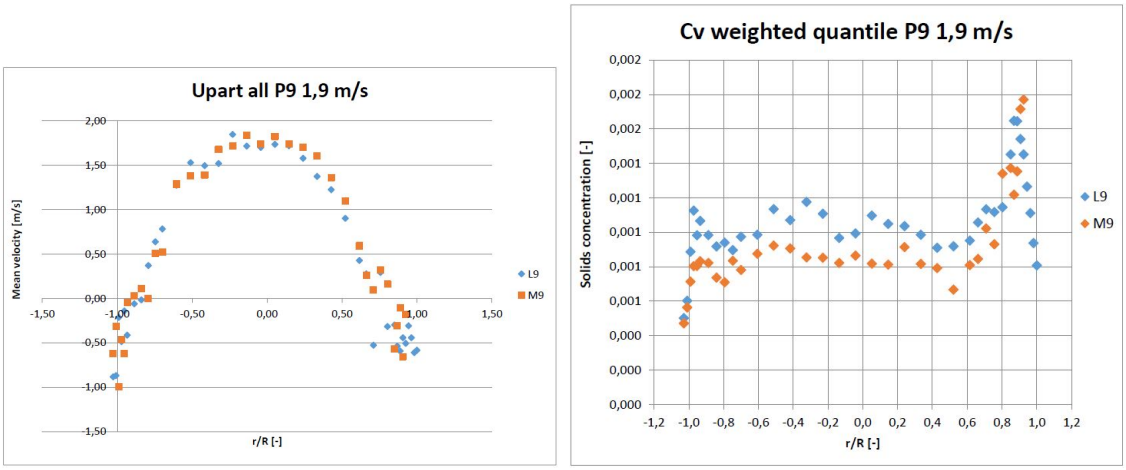

(a) Particle velocity. (b) Particle concentration.

Figure 110: Profile measurements at port nine with 1.9 m/s superficial gas velocity.

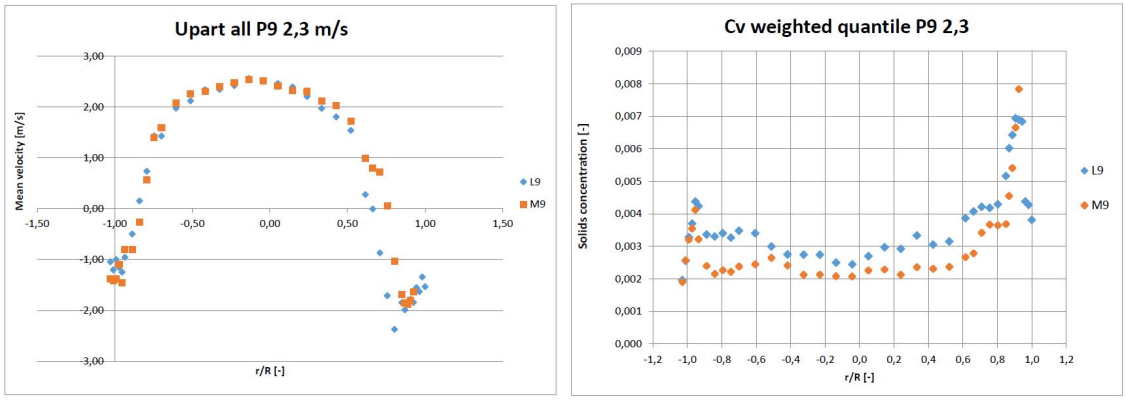

(a) Particle velocity. (b) Particle concentration.

Figure 111: Profile measurements at port nine with 2.3 m/s superficial gas velocity.

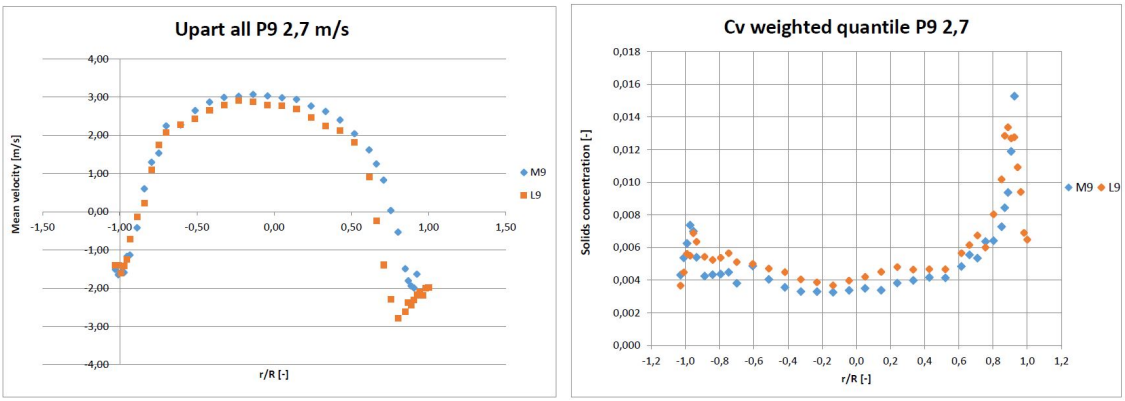

(a) Particle velocity. (b) Particle concentration.

Figure 112: Profile measurements at port nine with 2.7 m/s superficial gas velocity.

10.7 Port eleven

Following profile measurements are from port eleven at a height of 2262 mm.

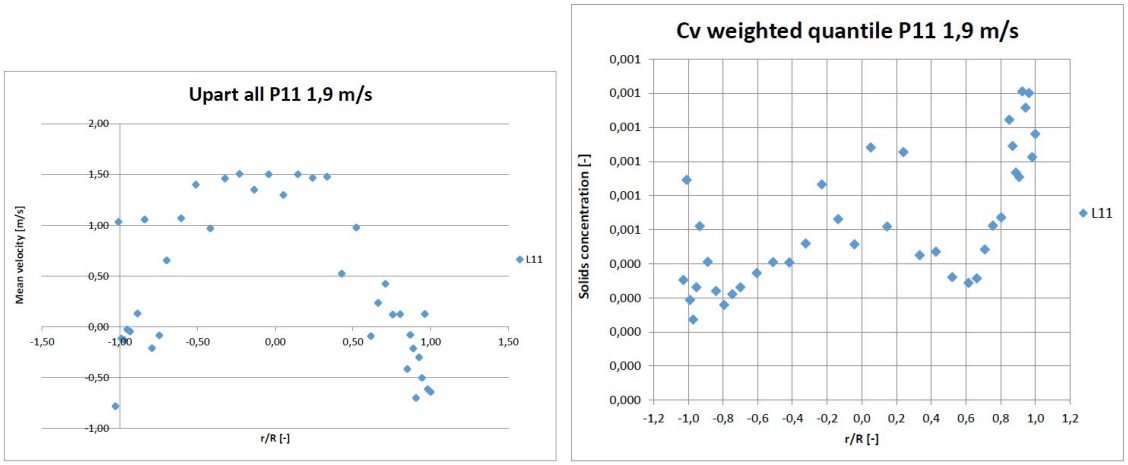

(a) Particle velocity. (b) Particle concentration.

Figure 113: Profile measurements at port eleven with 1.9 m/s superficial gas velocity.

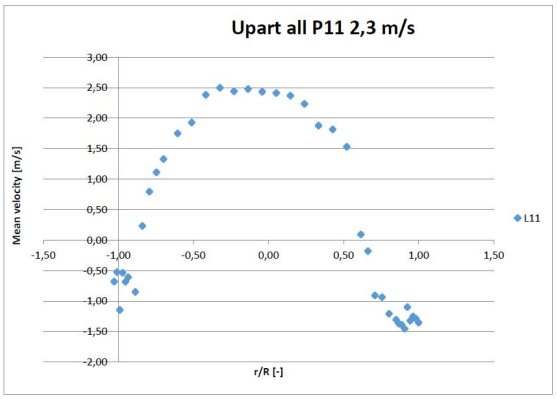

(a) Particle velocity.

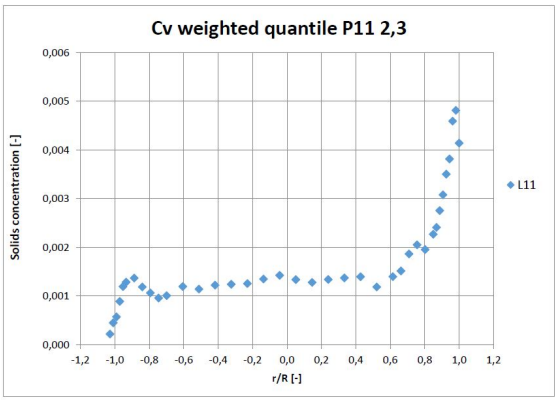

(b) Particle concentration.

Figure 114: Profile measurements at port eleven with 2.3 m/s superficial gas velocity.

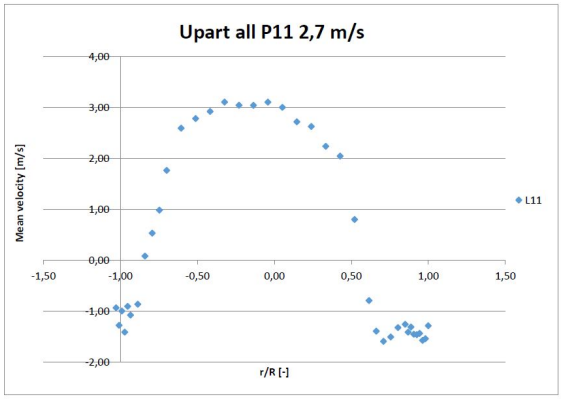

(a) Particle velocity.

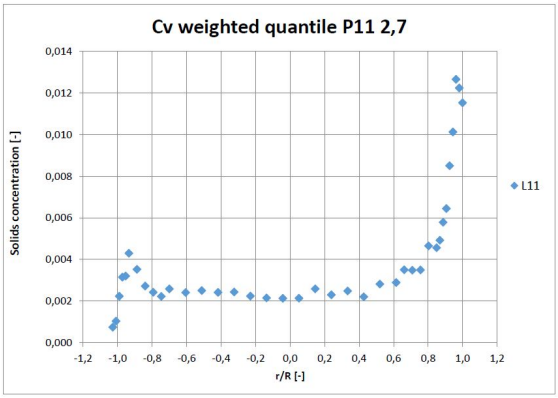

(b) Particle concentration.

Figure 115: Profile measurements at port eleven with 2.7 m/s superficial gas velocity.

11 Appendix compiled results

The following appendix contain evaluated results for all measurements, compared to each other.

11.1 Flow hydrodynamics for varying superficial gas velocities

Figures showing velocity, concentration and mass flux developments for different superficial gas velocities and constant particle size distribution.

11.1.1 Constant PSD of 70-110 μm

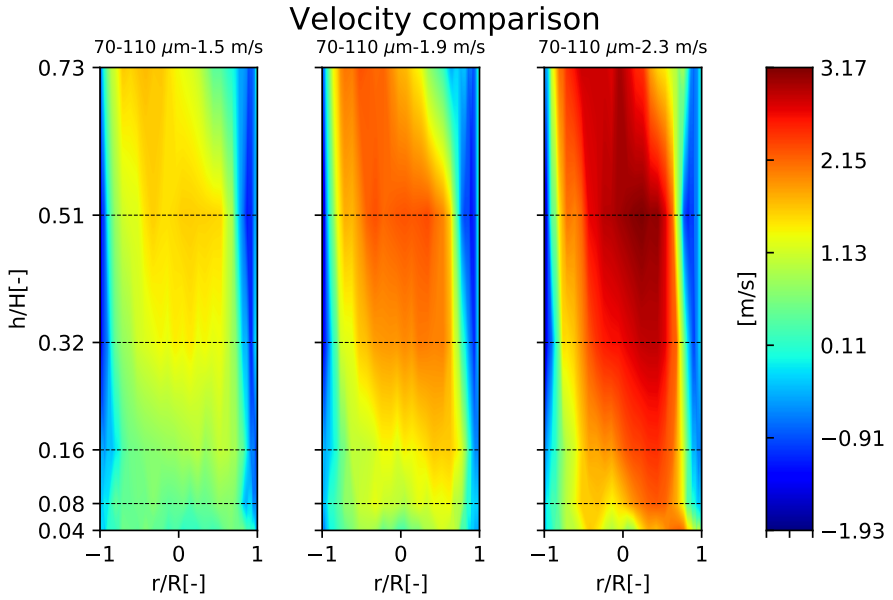

Figure 116: Particle velocity development with varying superficial gas velocity.

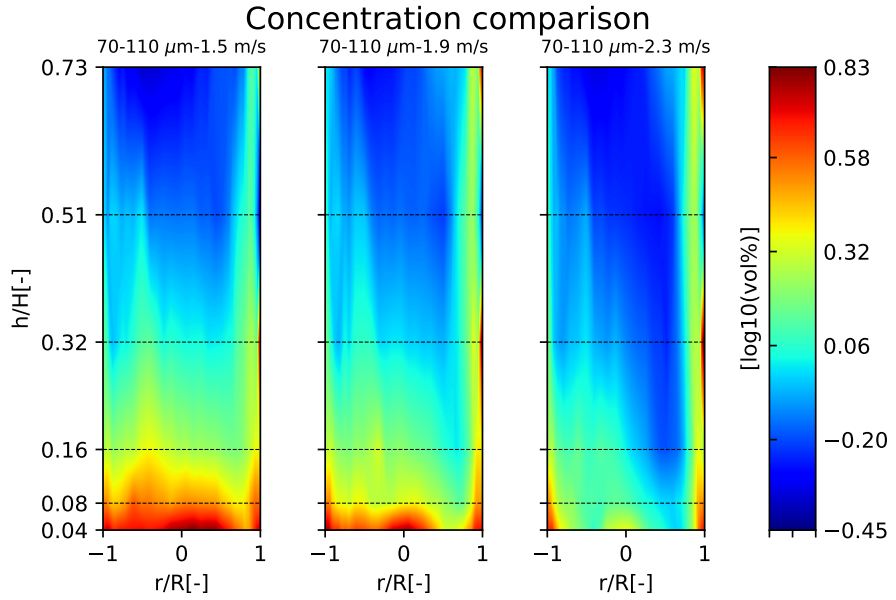

Figure 117: Particle volumetric concentration development with varying superficial gas velocity.

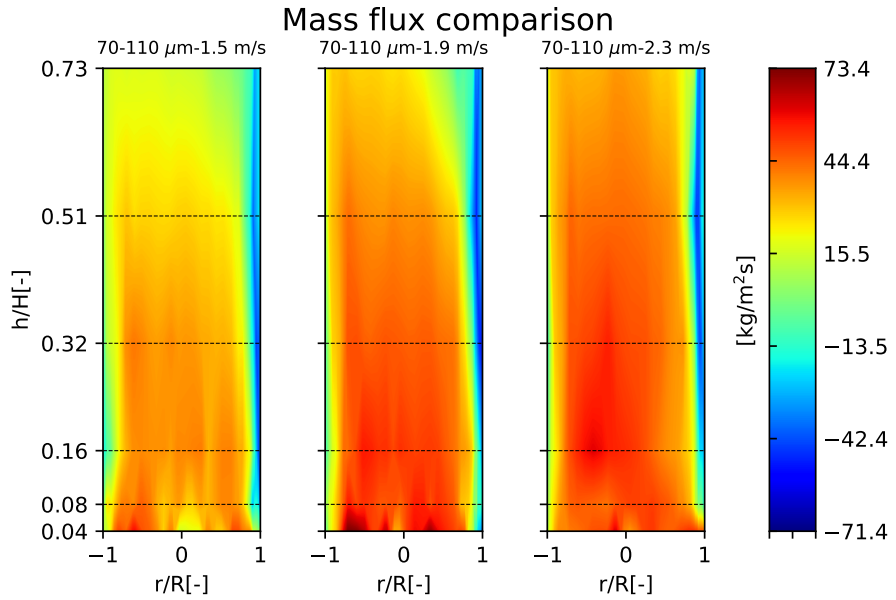

Figure 118: Particle mass flux development with varying superficial gas velocity.

11.1.2 Constant PSD of 100-200 μm

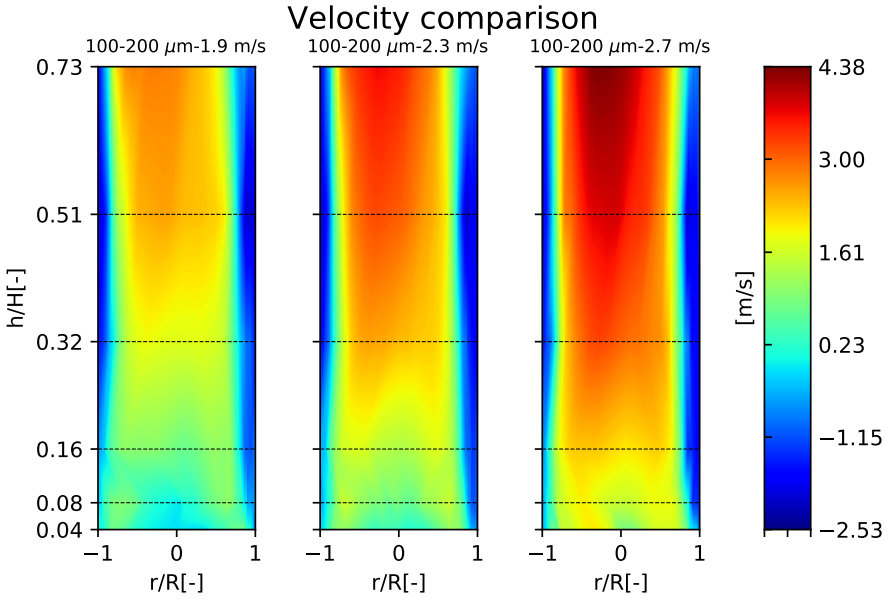

Figure 119: Particle velocity development with varying superficial gas velocity.

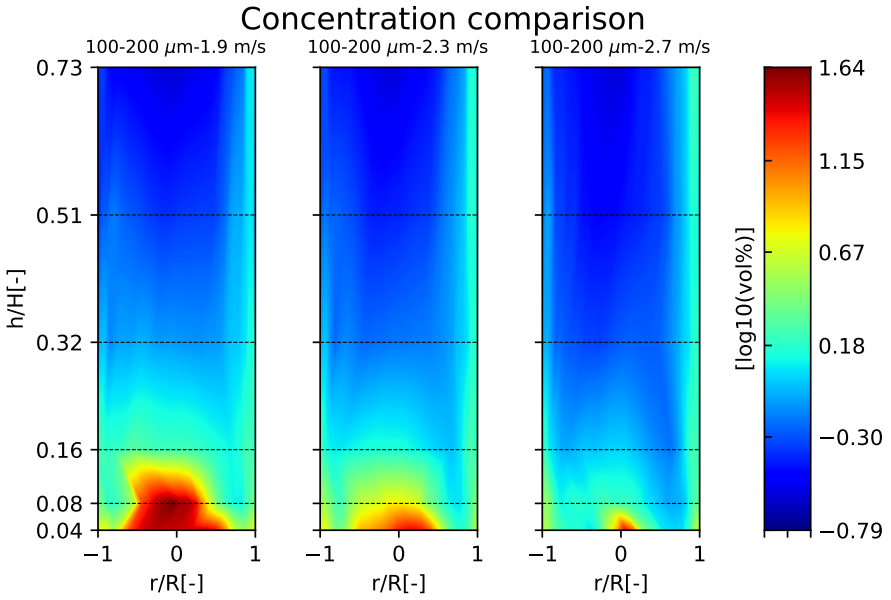

Figure 120: Particle volumetric concentration development with varying superficial gas velocity.

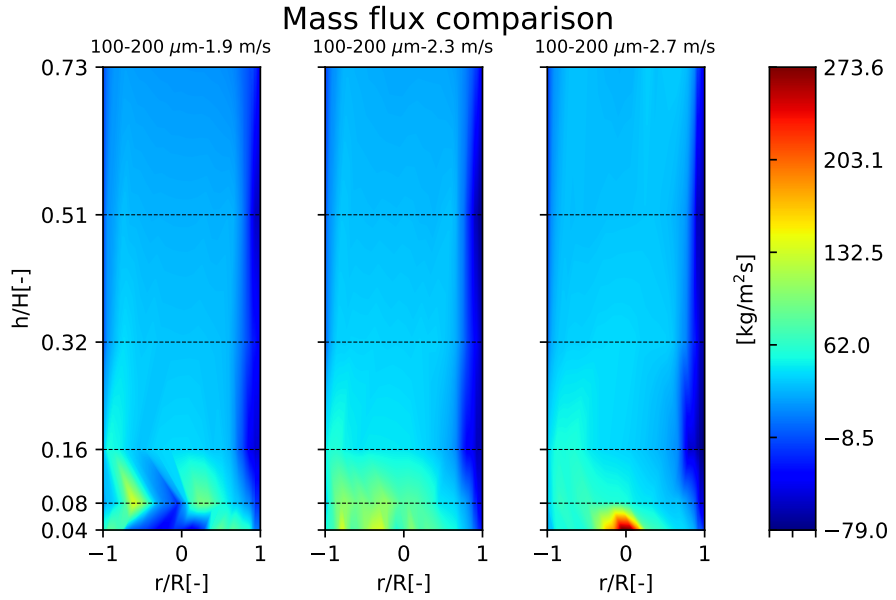

Figure 121: Particle mass flux development with varying superficial gas velocity.

11.1.3 Constant PSD of 200-300 μm

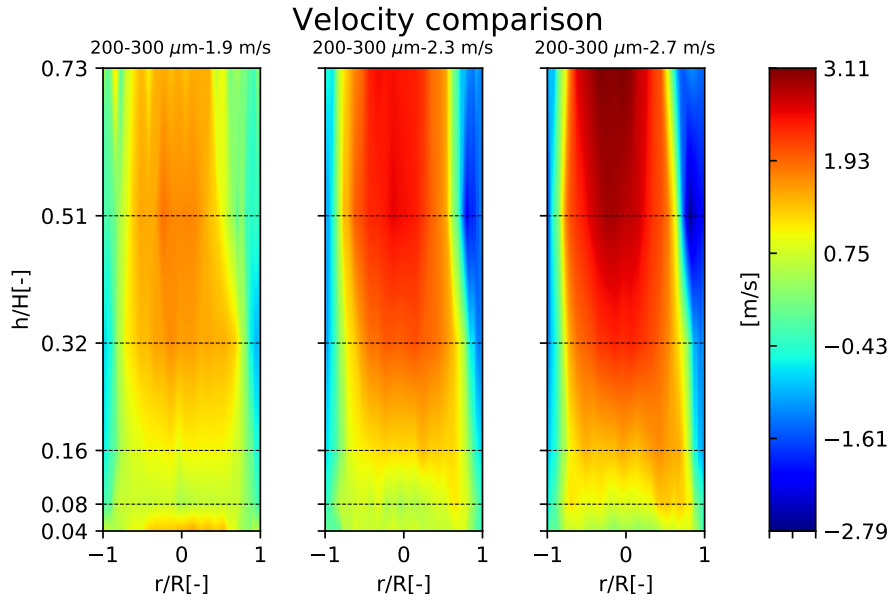

Figure 122: Particle velocity development with varying superficial gas velocity.

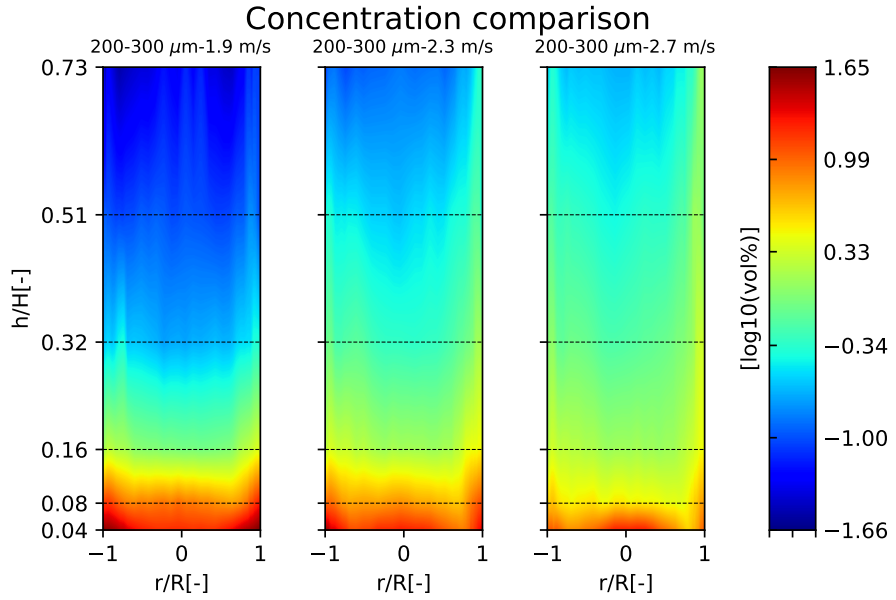

Figure 123: Particle volumetric concentration development with varying superficial gas velocity.

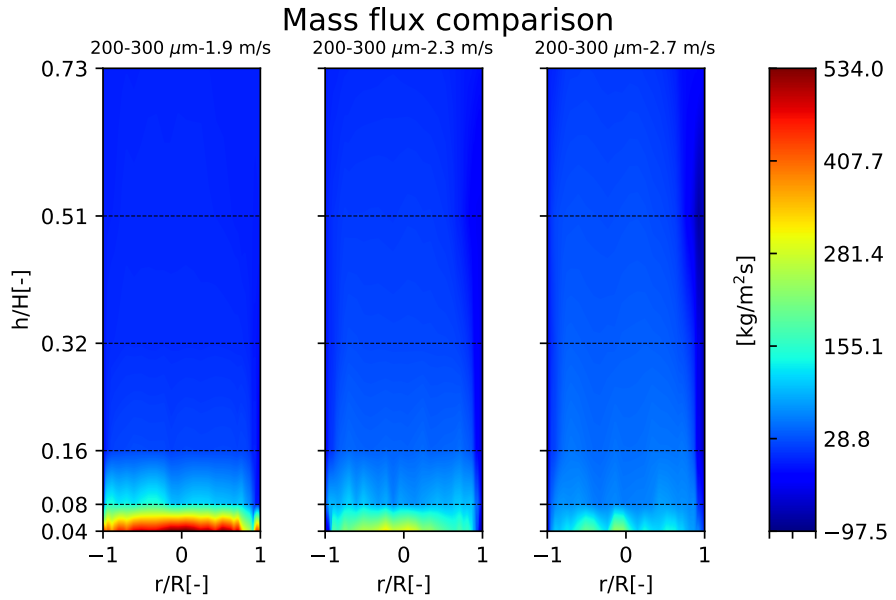

Figure 124: Particle mass flux development with varying superficial gas velocity.

11.2 Flow hydrodynamics for varying particle size distribution

Figures showing velocity, concentration and mass flux developments for different particle size distributions and constant superficial gas velocity.

11.2.1 Superficial gas velocity 1.9 m/s

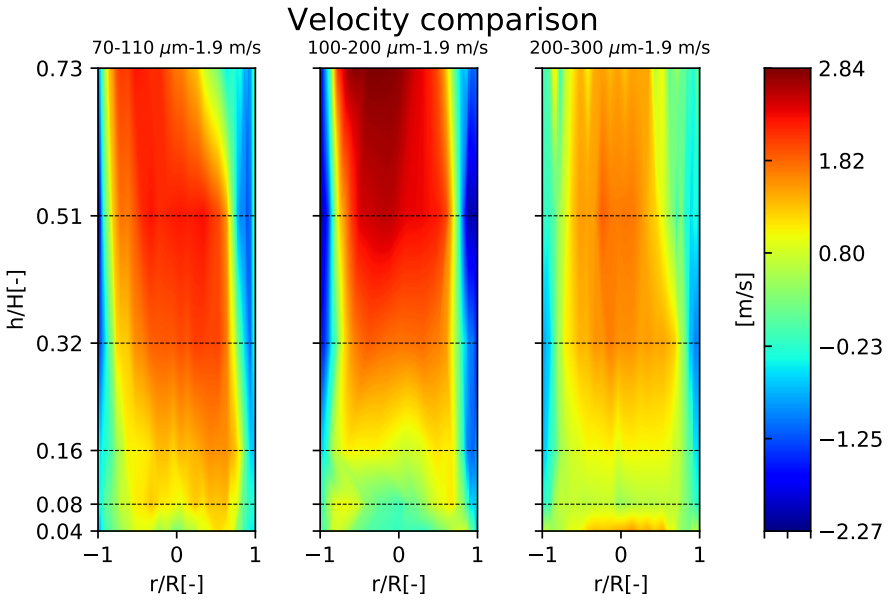

Figure 125: Particle velocity development with varying PSD.

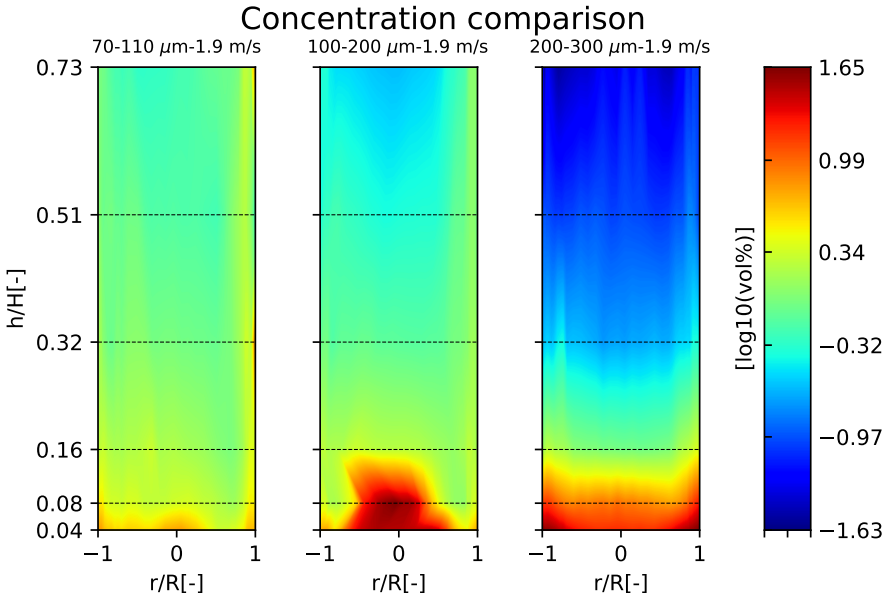

Figure 126: Particle volumetric concentration development with varying PSD.

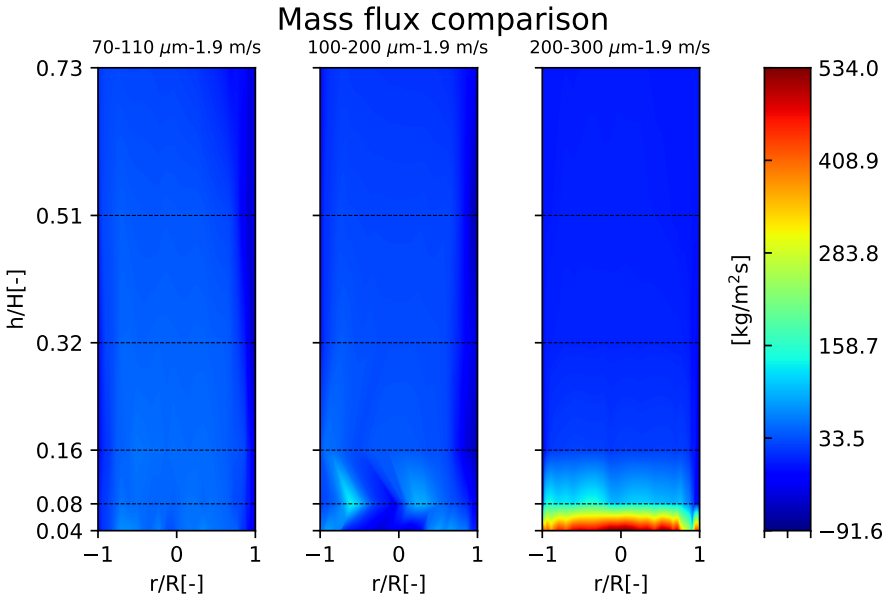

Figure 127: Particle mass flux development with varying PSD.

11.2.2 Superficial gas velocity 2.3 m/s

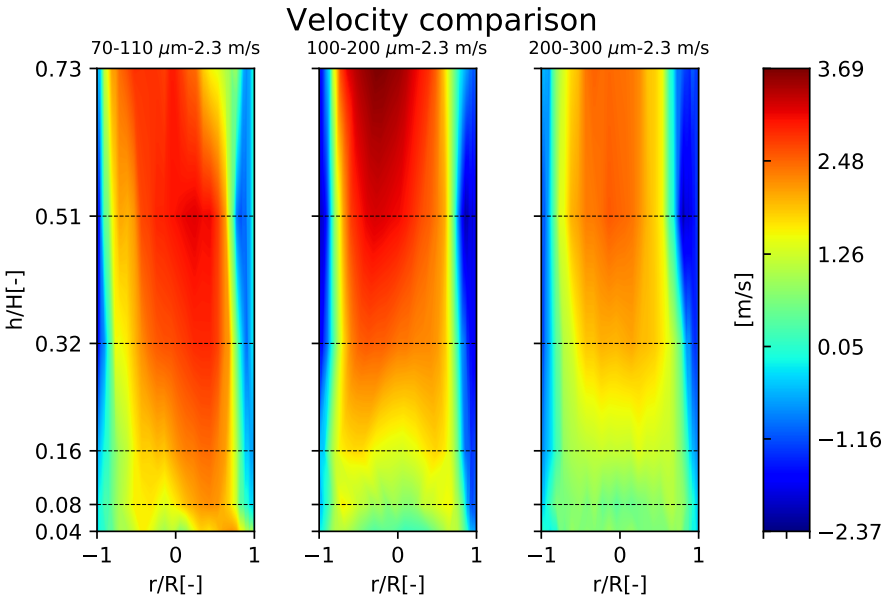

Figure 128: Particle velocity development with varying PSD.

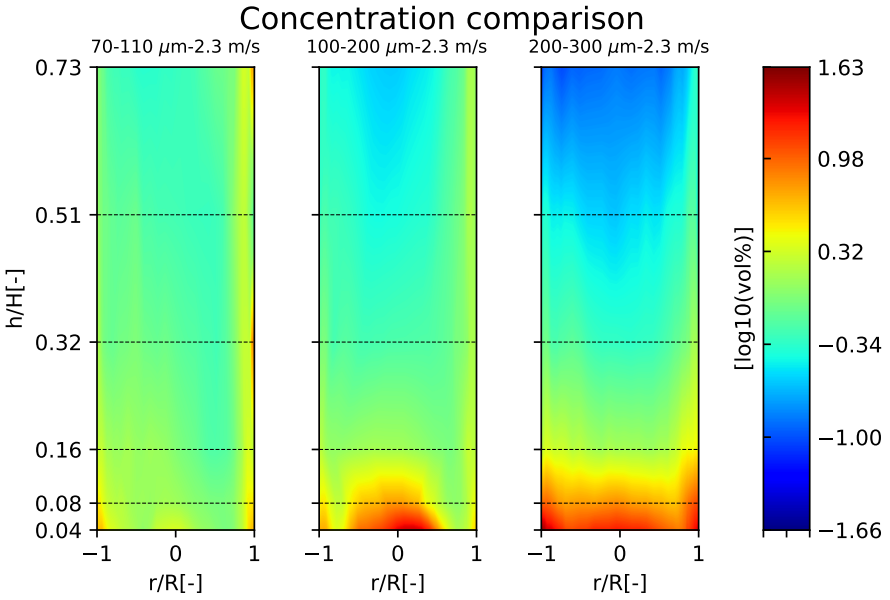

Figure 129: Particle volumetric concentration development with varying PSD.

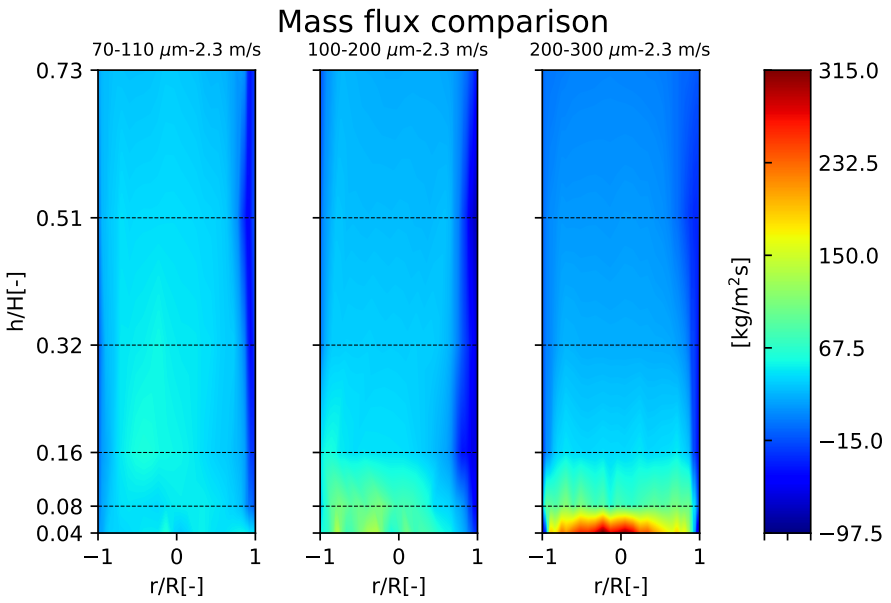

Figure 130: Particle mass flux development with varying PSD.

12 Appendix particle filter dependence

Evaluated results from capacitance probe measurements inside a scaled, cold flow CFB model at Darmstadt Technical University. Figures showing profiles of particle velocity and, for the two lowest measurement heights, constant weighted particle concentration. Figures for port four shows the weighted quantile of particle concentrations instead. Measurement heights are according to table 27, with a total riser height of approximately 3.1 meters.

Table 27: Heights of the ports on the scaled cold flow CFB model.

Port	**P1**	**P2**	**P4**
Height [mm]	124	248	496
h/H [-]	0.04	0.08	0.16

The presented figures contain measurements from;

- Glass microbeads with 100-200 μm size distribution. Operated with 25 μm mesh size in the bottom of the riser.
- Glass microbeads with 100-200 μm size distribution. Operated with >300 μm mesh size in the bottom of the riser.
- Old measurements of sand particles with 100-200 μm size distribution. Operated with >300 μm mesh size in the bottom of the riser.

12.1 Port one

Following profile measurements are from port one at a height of 124 mm.

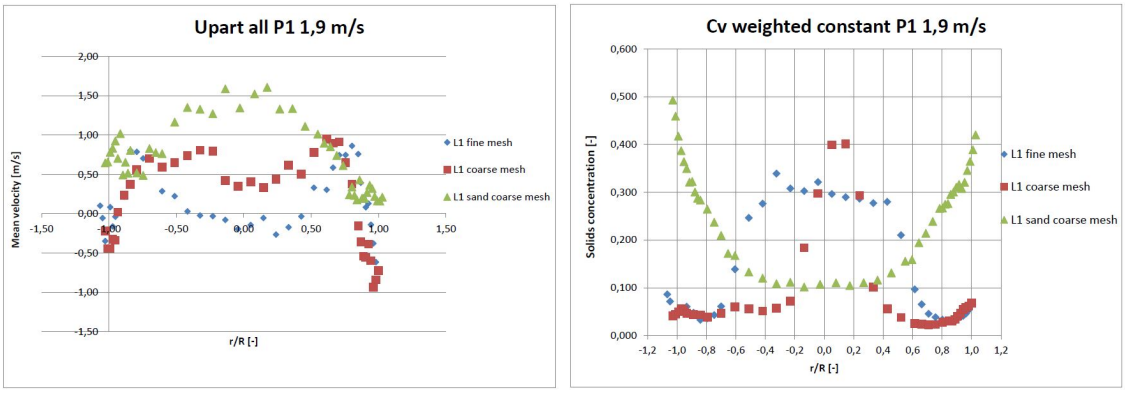

(a) Particle velocity.

(b) Particle concentration.

Figure 131: Profile measurements at port one with 1.9 m/s superficial gas velocity.

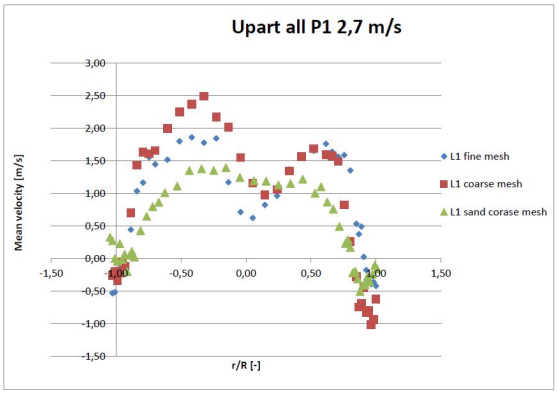

(a) Particle velocity.

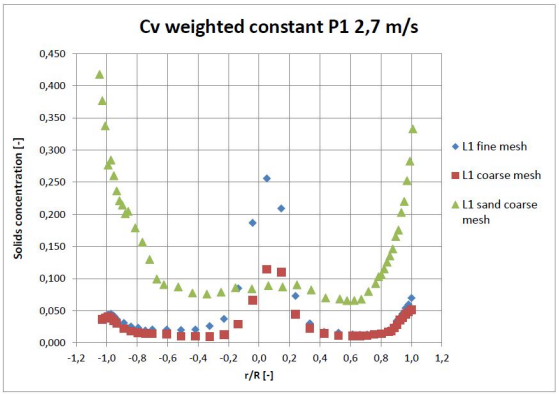

(b) Particle concentration.

Figure 132: Profile measurements at port one with 2.7 m/s superficial gas velocity.

12.2 Port two

Following profile measurements are from port two at a height of 248 mm.

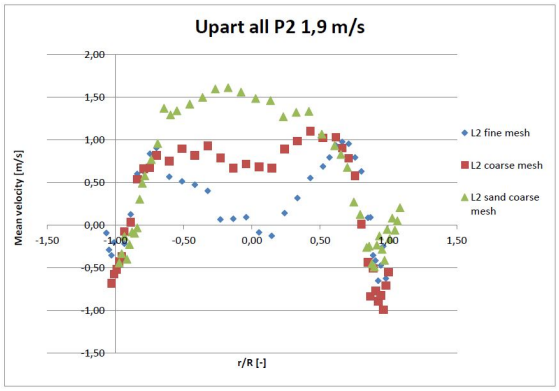

(a) Particle velocity.

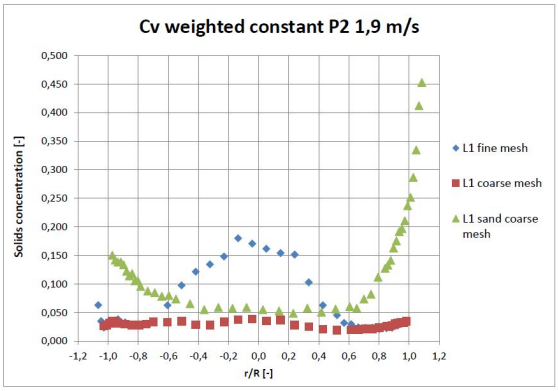

(b) Particle concentration.

Figure 133: Profile measurements at port two with 1.9 m/s superficial gas velocity.

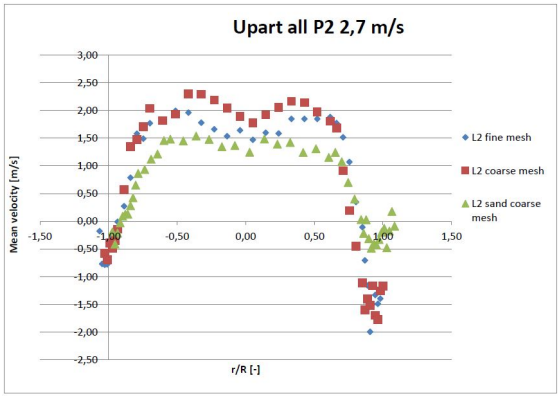

(a) Particle velocity.

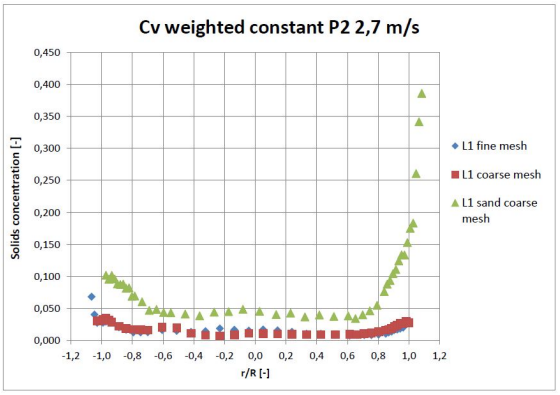

(b) Particle concentration.

Figure 134: Profile measurements at port two with 2.7 m/s superficial gas velocity.

12.3 Port four

Following profile measurements are from port four at a height of 496 mm.

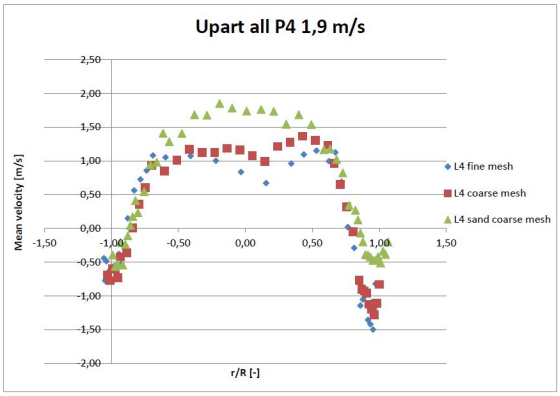

(a) Particle velocity.

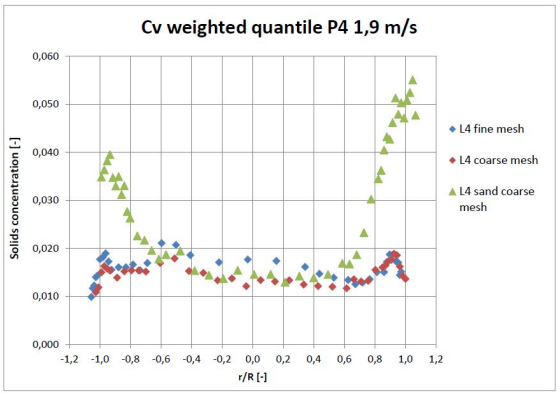

(b) Particle concentration.

Figure 135: Profile measurements at port four with 1.9 m/s superficial gas velocity.

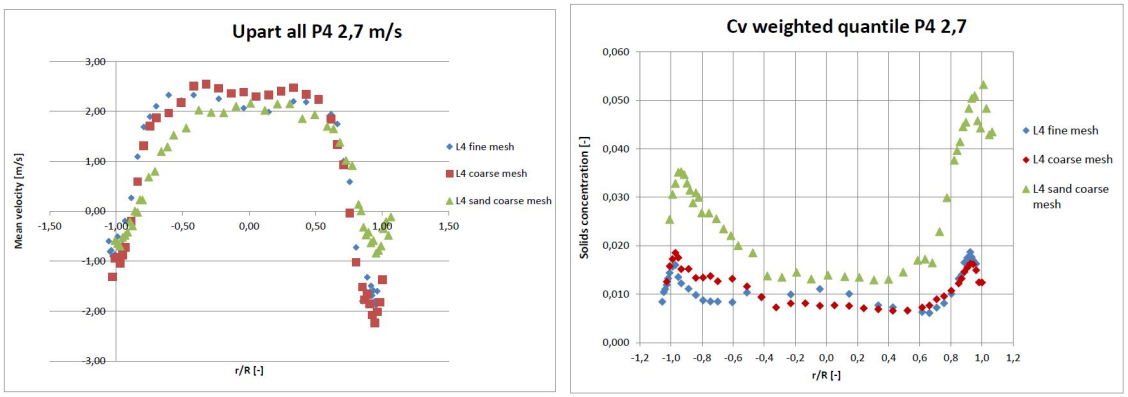

(a) Particle velocity.

(b) Particle concentration.

Figure 136: Profile measurements at port four with 2.7 m/s superficial gas velocity.

13 Appendix pressure profiles

Pressure profiles, inventory approximations and temperature development for glass beads with different size distributions and superficial gas velocities..

13.1 Material 70-110 μm PSD

Following pressure data are received from measurements on glass beads with a size distribution of 70-110 μm at different superficial gas velocities.

13.1.1 Superficial gas velocity 1.5 m/s

Figures below showing pressure- and temperature data during measurements with 1.5 m/s superficial gas velocity.

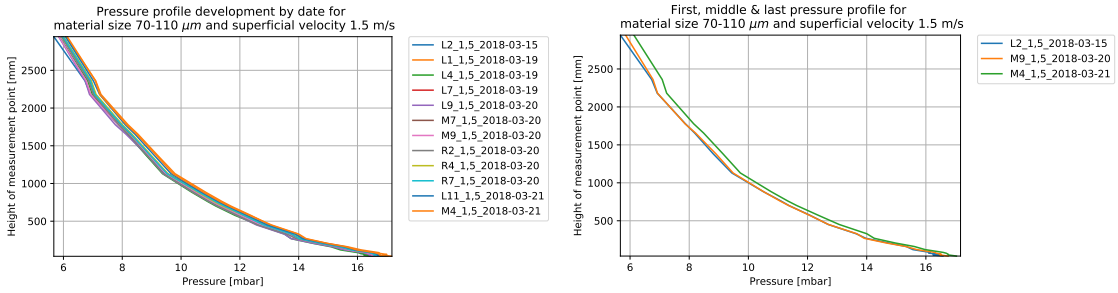

(a) All runs.

(b) First, middle and end run.

Figure 137: Pressure profile development for all measurements and for first, middle and end measurement with 1.5 m/s superficial gas velocity.

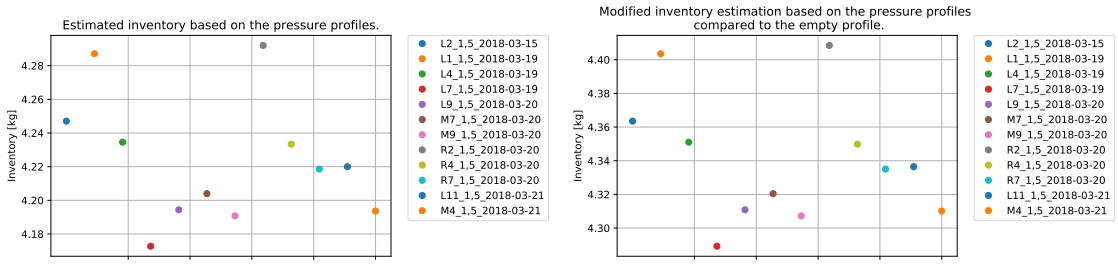

(a) Inventory approximation.

(b) Modified inventory approximation.

Figure 138: Inventory approximation and modified inventory approximation during measurements with 1.5 m/s superficial gas velocity.

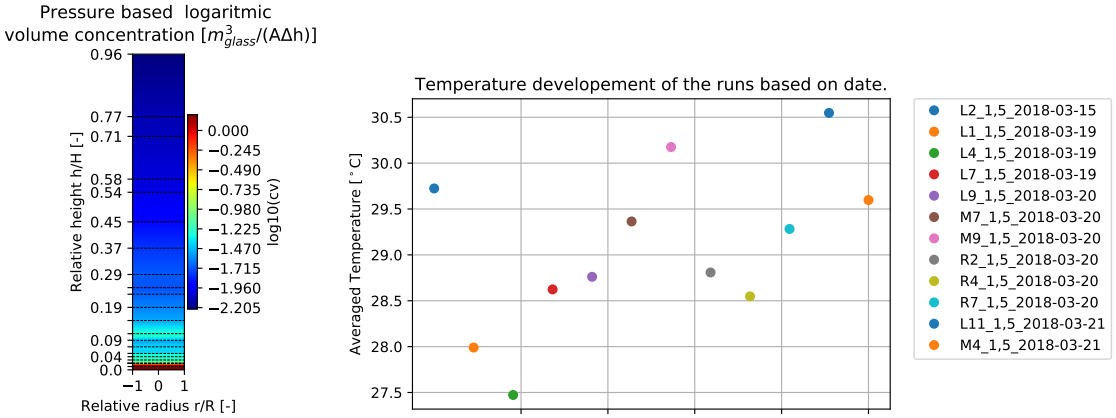

(a) Vol. concentration. (b) Operation temperature.

Figure 139: Concentration approximation and operation temperature during measurements with 1.5 m/s superficial gas velocity.

13.1.2 Superficial gas velocity 1.9 m/s

Figures below showing pressure- and temperature data during measurements with 1.9 m/s superficial gas velocity.

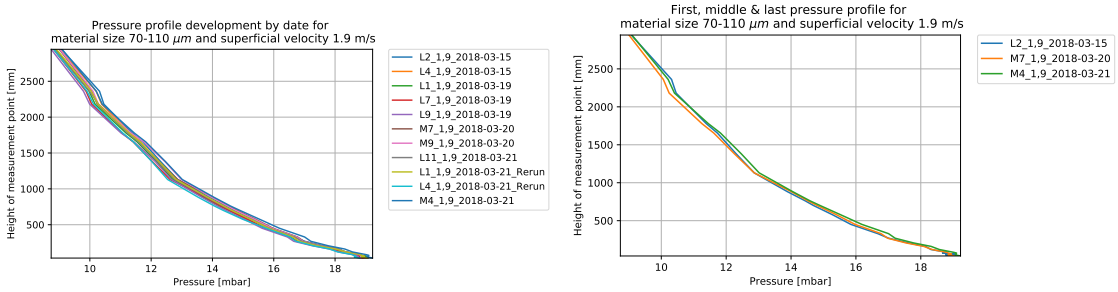

(a) All runs. (b) First, middle and end run.

Figure 140: Pressure profile development for all measurements and for first, middle and end measurement with 1.9 m/s superficial gas velocity.

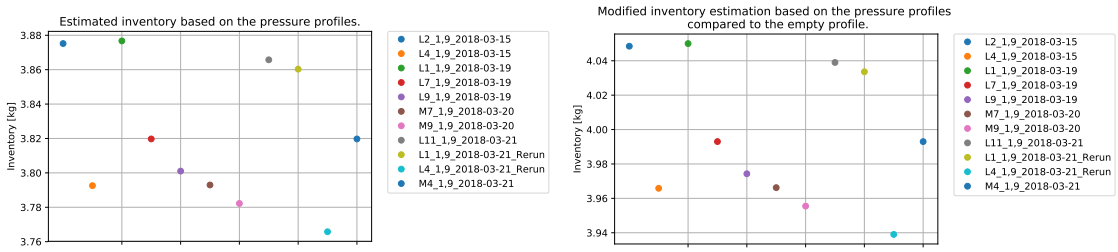

(a) Inventory approximation. (b) Modified inventory approximation.

Figure 141: Inventory approximation and modified inventory approximation during measurements with 1.9 m/s superficial gas velocity.

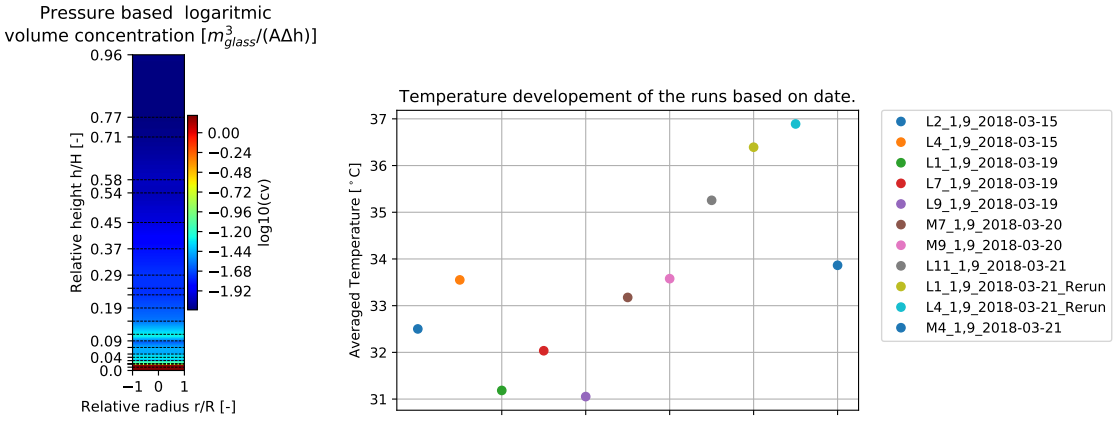

(a) Vol. concentration. (b) Operation temperature.

Figure 142: Concentration approximation and operation temperature during measurements with 1.9 m/s superficial gas velocity.

13.1.3 Superficial gas velocity 2.3 m/s

Figures below showing pressure- and temperature data during measurements with 2.3 m/s superficial gas velocity.

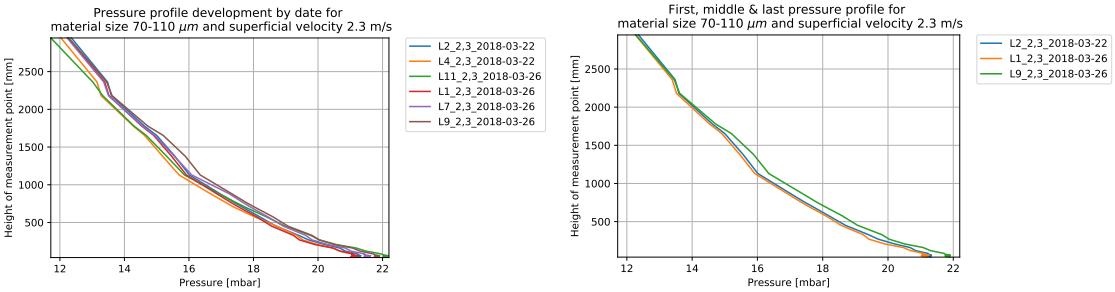

(a) All runs. (b) First, middle and end run.

Figure 143: Pressure profile development for all measurements and for first, middle and end measurement with 2.3 m/s superficial gas velocity.

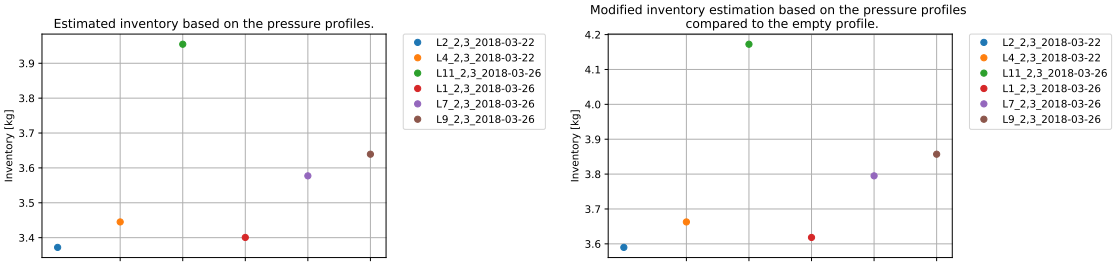

(a) Inventory approximation. (b) Modified inventory approximation.

Figure 144: Inventory approximation and modified inventory approximation during measurements with 2.3 m/s superficial gas velocity.

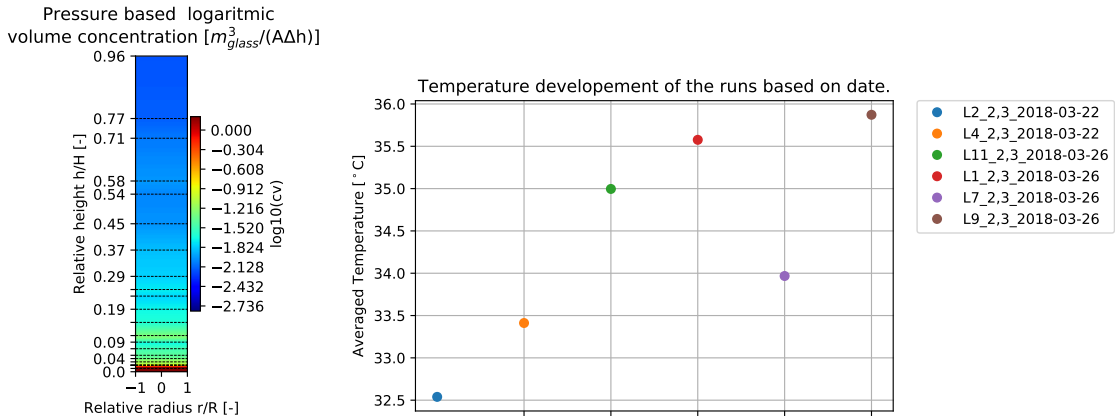

(a) Vol. concentration. (b) Operation temperature.

Figure 145: Concentration approximation and operation temperature during measurements with 2.3 m/s superficial gas velocity.

13.2 Material 100-200 μm PSD

Following pressure data are received from measurements on glass beads with a size distribution of 100-200 μm at different superficial gas velocities.

13.2.1 Superficial gas velocity 1.5 m/s

Figures below showing pressure- and temperature data during measurements with 1.5 m/s superficial gas velocity.

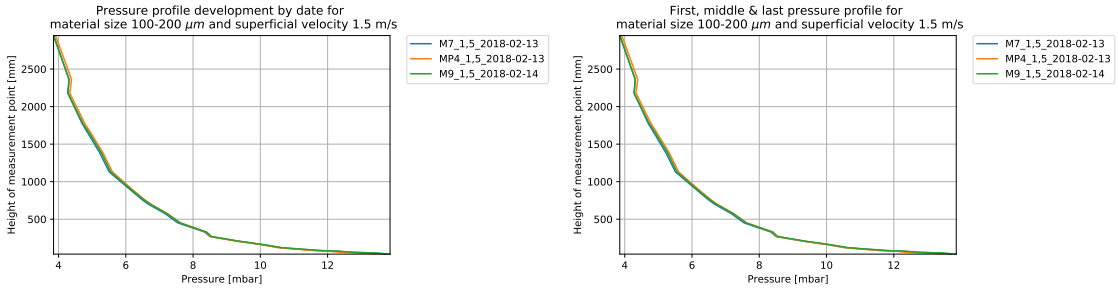

(a) All runs. (b) First, middle and end run.

Figure 146: Pressure profile development for all measurements and for first, middle and end measurement with 1.5 m/s superficial gas velocity.

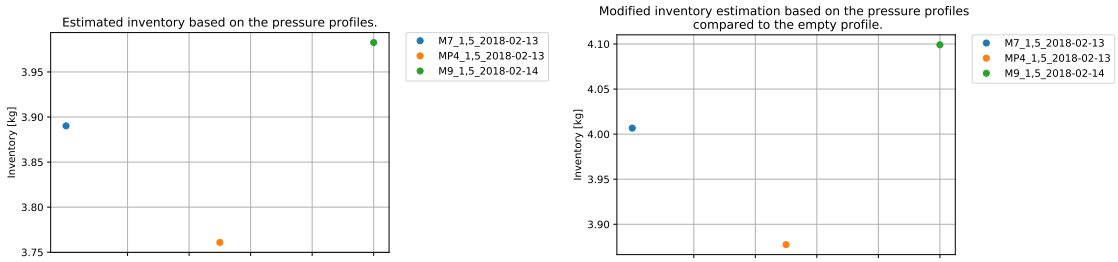

(a) Inventory approximation. (b) Modified inventory approximation.

Figure 147: Inventory approximation and modified inventory approximation during measurements with 1.5 m/s superficial gas velocity.

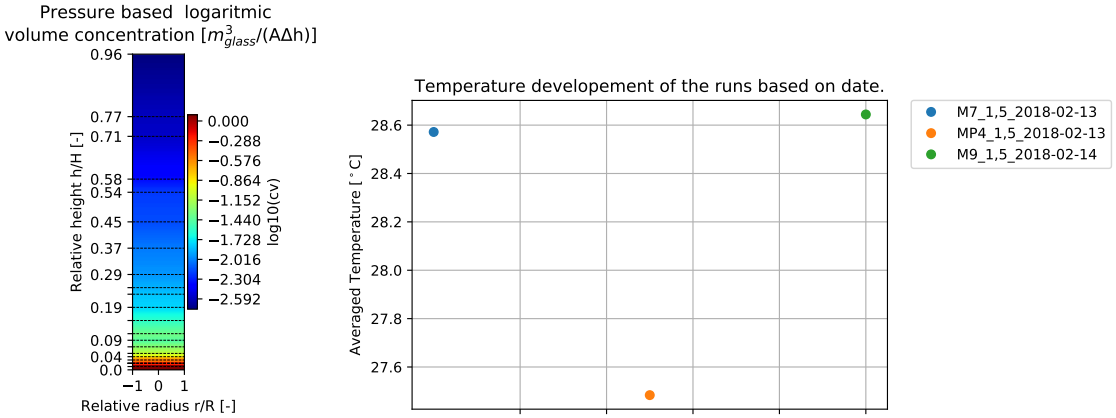

(a) Vol. concentration. (b) Operation temperature.

Figure 148: Concentration approximation and operation temperature during measurements with 1.5 m/s superficial gas velocity.

13.2.2 Superficial gas velocity 1.9 m/s

Figures below showing pressure- and temperature data during measurements with 1.9 m/s superficial gas velocity.

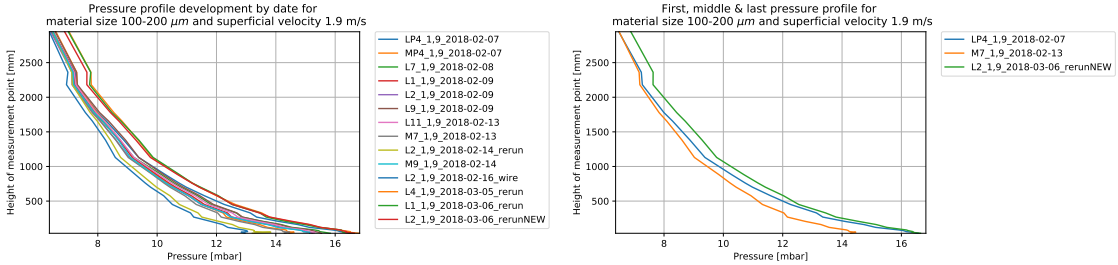

(a) All runs. (b) First, middle and end run.

Figure 149: Pressure profile development for all measurements and for first, middle and end measurement with 1.9 m/s superficial gas velocity.

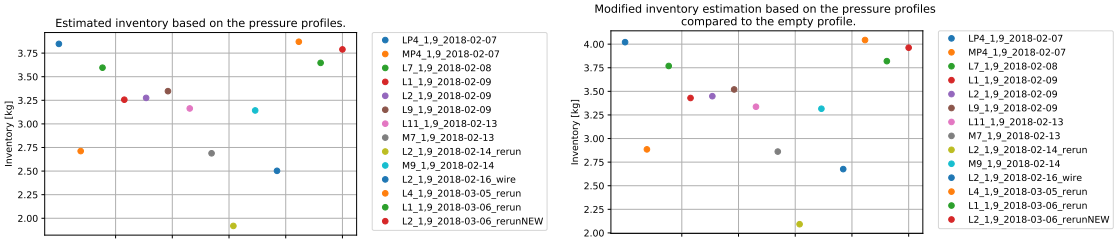

(a) Inventory approximation. (b) Modified inventory approximation.

Figure 150: Inventory approximation and modified inventory approximation during measurements with 1.9 m/s superficial gas velocity.

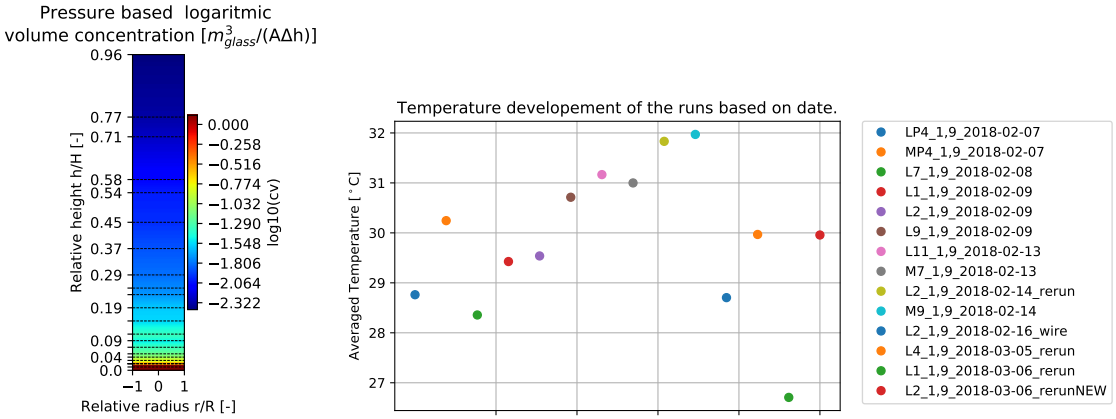

(a) Vol. concentration. (b) Operation temperature.

Figure 151: Concentration approximation and operation temperature during measurements with 1.9 m/s superficial gas velocity.

13.2.3 Superficial gas velocity 2.3 m/s

Figures below showing pressure- and temperature data during measurements with 2.3 m/s superficial gas velocity.

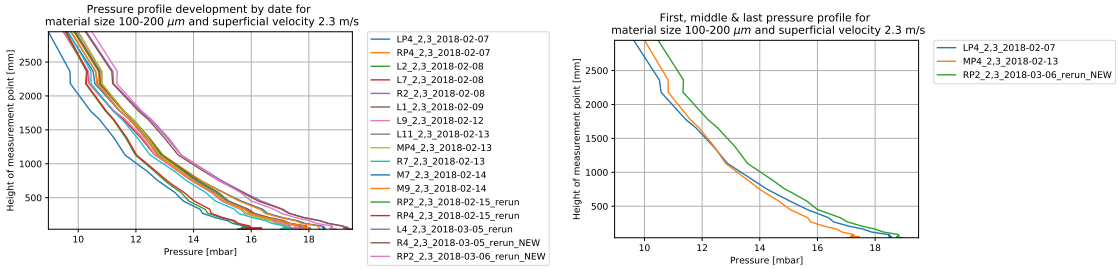

(a) All runs. (b) First, middle and end run.

Figure 152: Pressure profile development for all measurements and for first, middle and end measurement with 2.3 m/s superficial gas velocity.

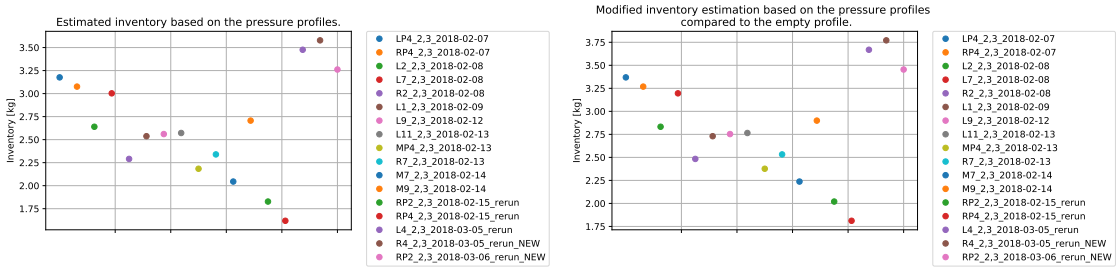

(a) Inventory approximation. (b) Modified inventory approximation.

Figure 153: Inventory approximation and modified inventory approximation during measurements with 2.3 m/s superficial gas velocity.

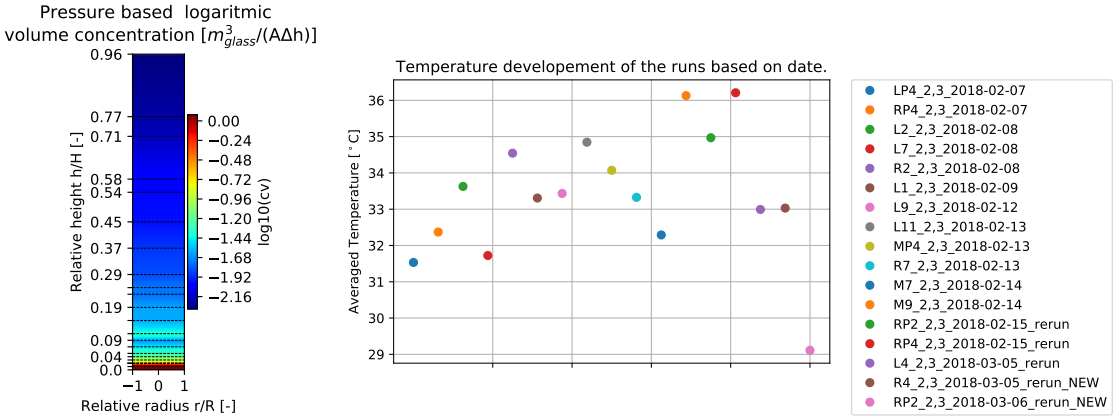

(a) Vol. concentration. (b) Operation temperature.

Figure 154: Concentration approximation and operation temperature during measurements with 2.3 m/s superficial gas velocity.

13.2.4 Superficial gas velocity 2.7 m/s

Figures below showing pressure- and temperature data during measurements with 2.7 m/s superficial gas velocity.

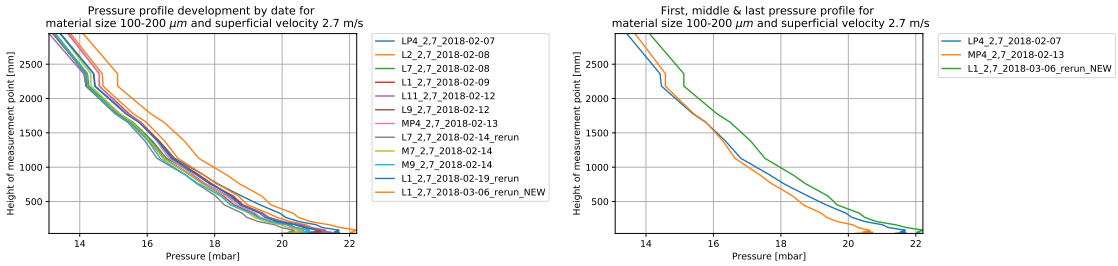

(a) All runs. (b) First, middle and end run.

Figure 155: Pressure profile development for all measurements and for first, middle and end measurement with 2.7 m/s superficial gas velocity.

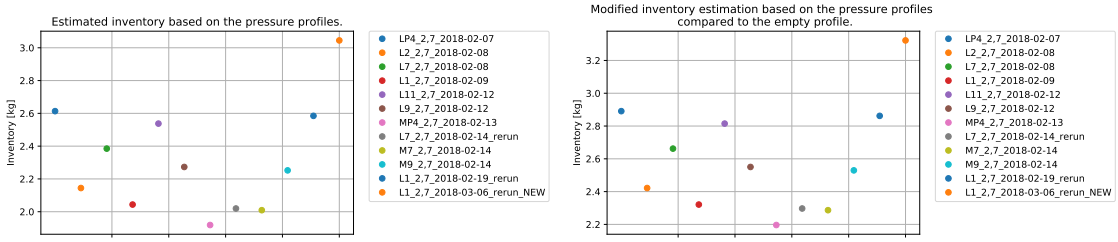

(a) Inventory approximation. (b) Modified inventory approximation.

Figure 156: Inventory approximation and modified inventory approximation during measurements with 2.7 m/s superficial gas velocity.

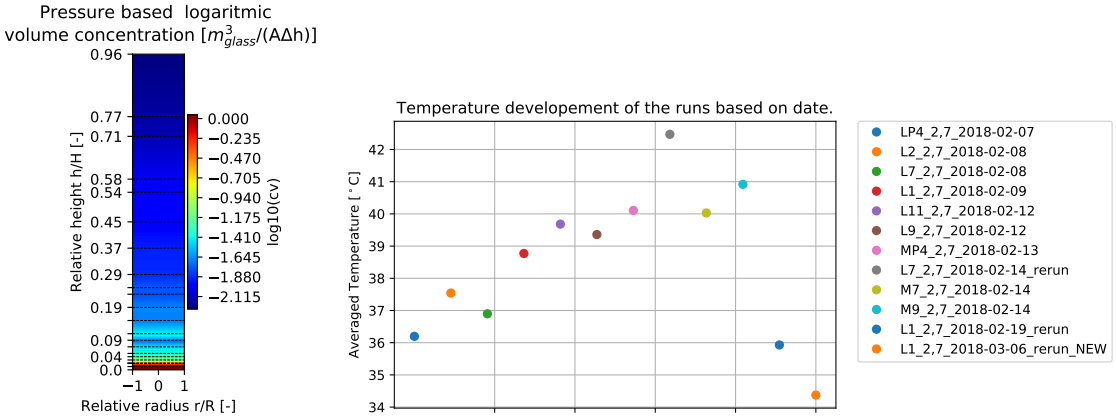

(a) Vol. concentration. (b) Operation temperature.

Figure 157: Concentration approximation and operation temperature during measurements with 2.7 m/s superficial gas velocity.

13.3 Material 200-300 μm PSD

Following pressure data are received from measurements on glass beads with a size distribution of 200-300 μm at different superficial gas velocities.

13.3.1 Superficial gas velocity 1.5 m/s

Figures below showing pressure- and temperature data during measurements with 1.5 m/s superficial gas velocity.

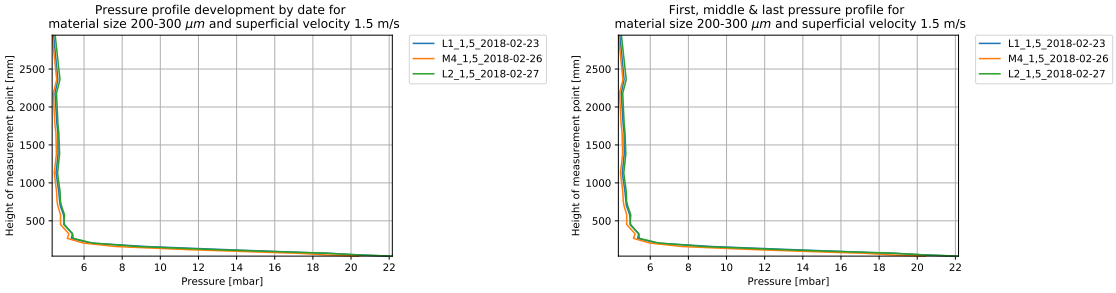

(a) All runs. (b) First, middle and end run.

Figure 158: Pressure profile development for all measurements and for first, middle and end measurement with 1.5 m/s superficial gas velocity.

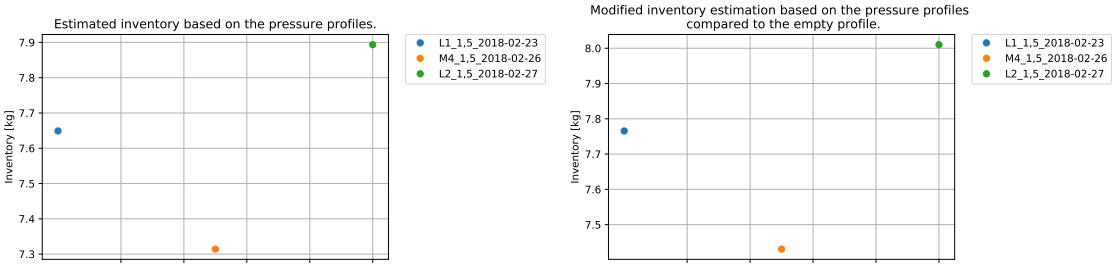

(a) Inventory approximation. (b) Modified inventory approximation.

Figure 159: Inventory approximation and modified inventory approximation during measurements with 1.5 m/s superficial gas velocity.

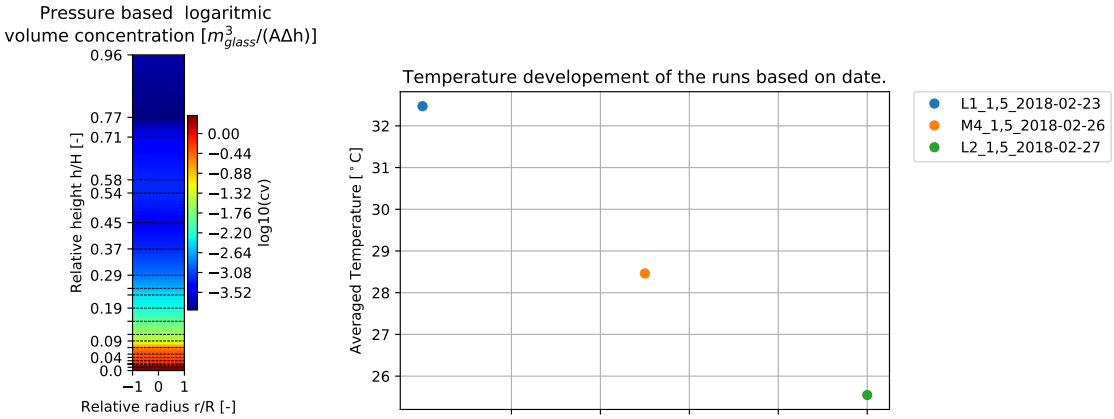

(a) Vol concentration. (b) Operation temperature.

Figure 160: Concentration approximation and operation temperature during measurements with 1.5 m/s superficial gas velocity.

13.3.2 Superficial gas velocity 1.9 m/s

Figures below showing pressure- and temperature data during measurements with 1.9 m/s superficial gas velocity.

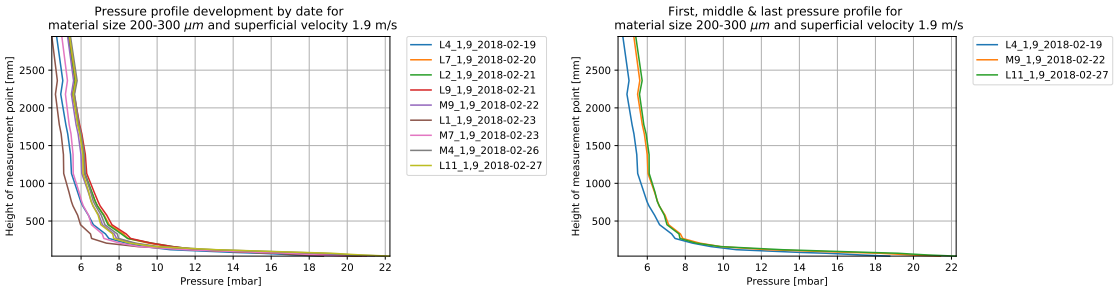

(a) All runs. (b) First, middle and end run.

Figure 161: Pressure profile development for all measurements and for first, middle and end measurement with 1.9 m/s superficial gas velocity.

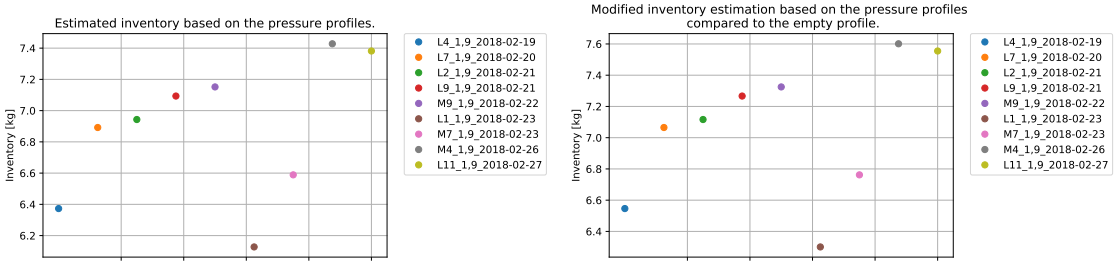

(a) Inventory approximation. (b) Modified inventory approximation.

Figure 162: Inventory approximation and modified inventory approximation during measurements with 1.9 m/s superficial gas velocity.

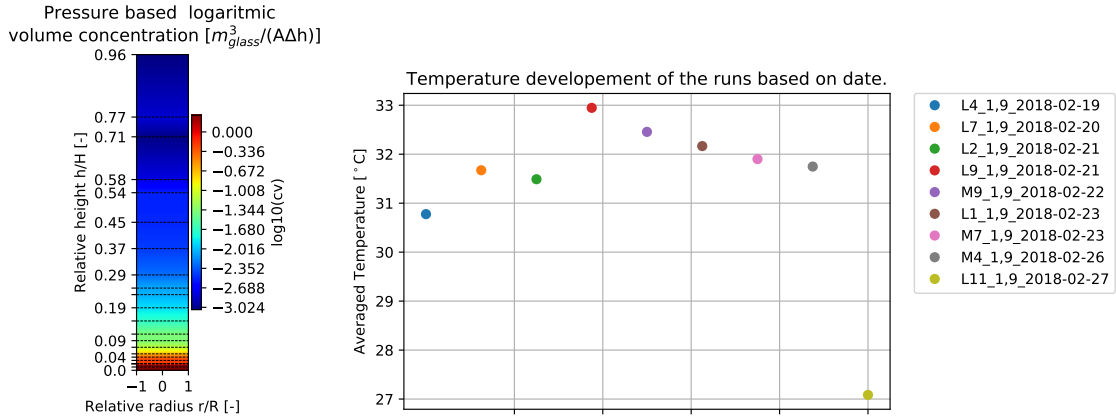

(a) Vol. concentration. (b) Operation temperature.

Figure 163: Concentration approximation and operation temperature during measurements with 1.9 m/s superficial gas velocity.

13.3.3 Superficial gas velocity 2.3 m/s

Figures below showing pressure- and temperature data during measurements with 2.3 m/s superficial gas velocity.

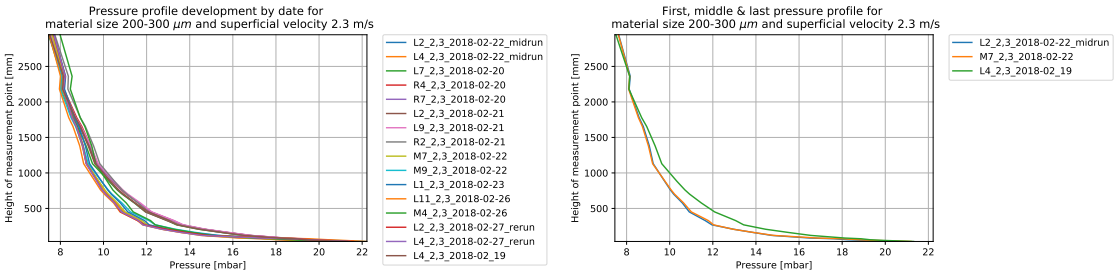

(a) All runs. (b) First, middle and end run.

Figure 164: Pressure profile development for all measurements and for first, middle and end measurement with 2.3 m/s superficial gas velocity.

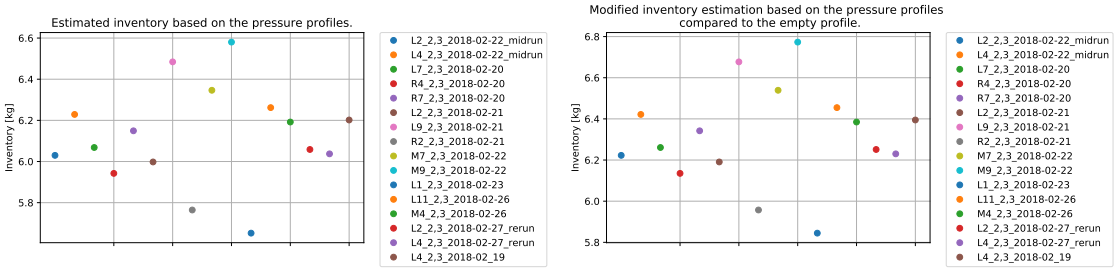

(a) Inventory approximation. (b) Modified inventory approximation.

Figure 165: Inventory approximation and modified inventory approximation during measurements with 2.3 m/s superficial gas velocity.

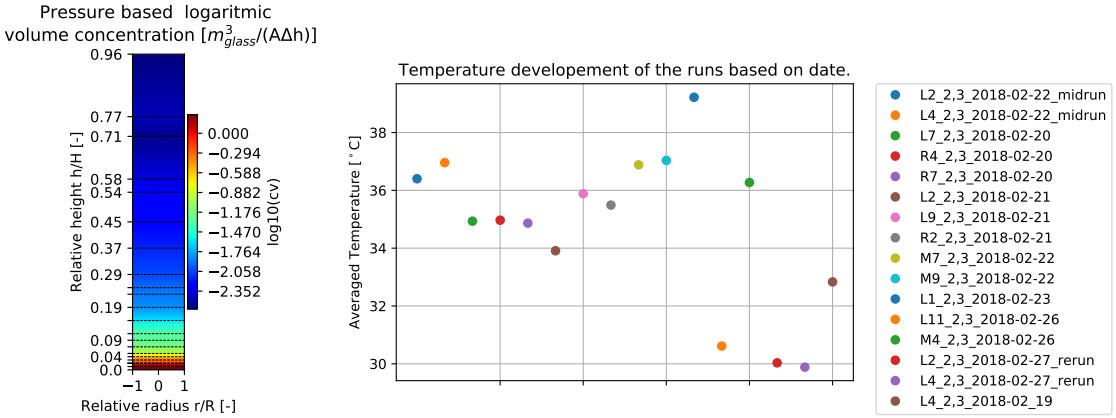

(a) Vol. concentration. (b) Operation temperature.

Figure 166: Concentration approximation and operation temperature during measurements with 2.3 m/s superficial gas velocity.

13.3.4 Superficial gas velocity 2.7 m/s

Figures below showing pressure- and temperature data during measurements with 2.7 m/s superficial gas velocity.

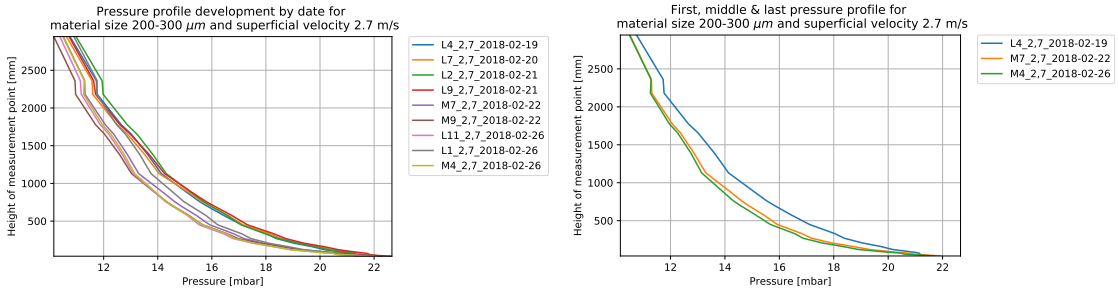

(a) All runs. (b) First, middle and end run.

Figure 167: Pressure profile development for all measurements and for first, middle and end measurement with 2.7 m/s superficial gas velocity.

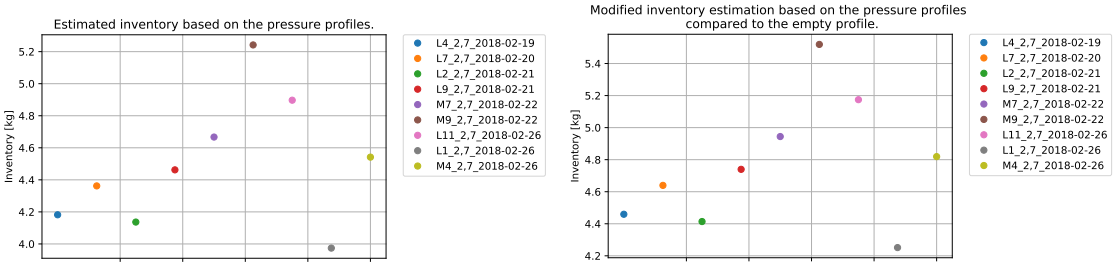

(a) Inventory approximation. (b) Modified inventory approximation.

Figure 168: Inventory approximation and modified inventory approximation during measurements with 2.7 m/s superficial gas velocity.

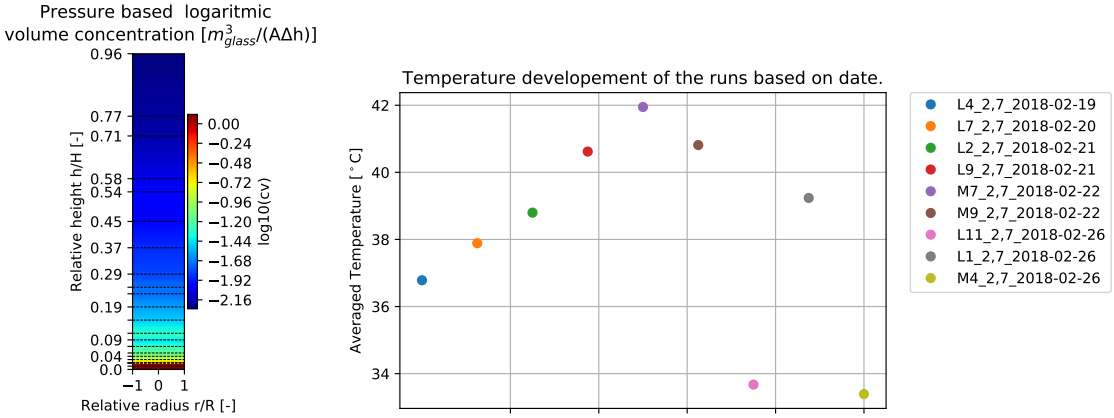

(a) Vol. concentration. (b) Operation temperature.

Figure 169: Concentration approximation and operation temperature during measurements with 2.7 m/s superficial gas velocity.

14 Appendix SEM

Surface topography and composition determined by SEM for all materials.

14.1 Material 70-110 μm

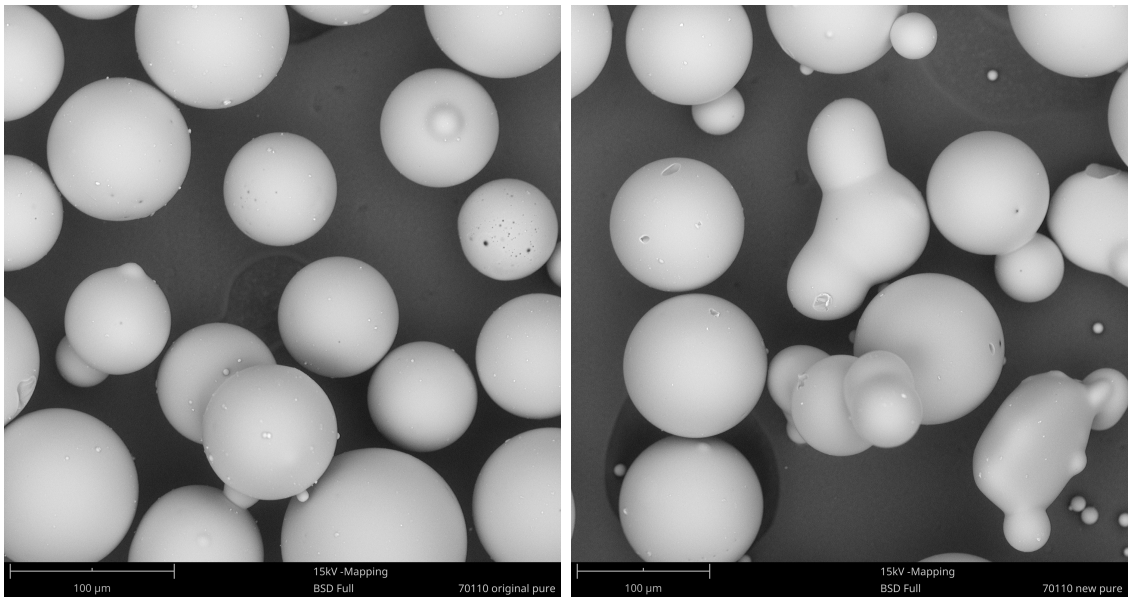

(a) Original material. (b) Newly purchased material.

Figure 170: Original and newly purchased pure 70-110 μm material.

Table 28: Result from point analysis of element identification on 70-110 μm original- and newly purchased material.

Element symbol	**Element name**	**Original material**		**New material**	
		Atomic conc.	**Weight conc.**	**Atomic conc.**	**Weight conc.**
O	Oxygen	66.61	54.56	64.78	52.32
Si	Silicon	16.74	24.07	18.42	26.10
Na	Sodium	11.32	13.32	11.02	12.78
Mg	Magnesium	2.52	3.14	2.63	4.21
Ca	Calcium	1.76	3.61	1.86	3.03
Al	Aluminum	0.70	0.97	0.90	1.22
C	Carbon	0.30	0.18	0.36	0.22
Fe	Iron	0.02	0.07	0.02	0.06
Cr	Chromium	0.04	0.11	0.01	0.03
Mn	Manganese	0.00	0.00	0.02	0.05

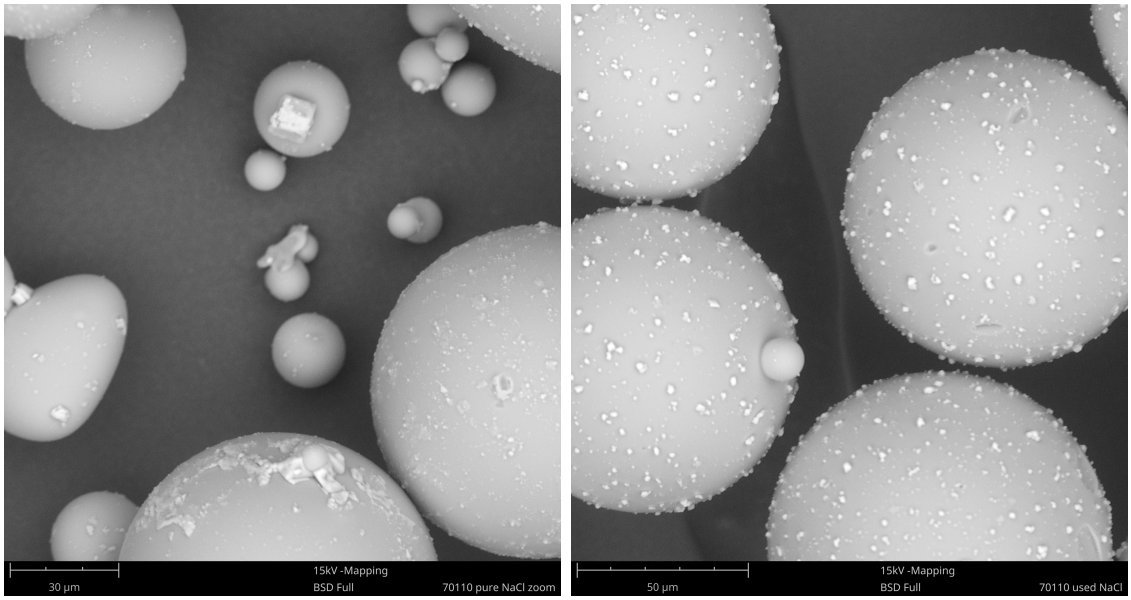

(a) Unused NaCl coated. (b) Used NaCl coated.

Figure 171: Mix of the newly purchased and original 70-110 μm material coated with NaCl, before and after CFB usage.

Table 29: Result from element mapping on 70-110 μm material mixed with salt (NaCl). Unused- and used material.

Element symbol	**Element name**	**Unused material**		**Used material**	
		Atomic conc.	**Weight conc.**	**Atomic conc.**	**Weight conc.**
O	Oxygen	65,15	53,49	65,80	54,03
Si	Silicon	14,58	21,00	15,05	21,69
Na	Sodium	13,67	16,13	13,68	16,14
Mg	Magnesium	2,33	2,91	2,40	2,99
Ca	Calcium	1,62	3,32	1,64	3,37
C	Carbon	1,22	0,75	0,76	0,47
Cl	Chlorine	0,78	1,42	0,60	1,09
Al	Aluminum	0,60	0,83	-	-
Fe	Iron	0,05	0,14	0,06	0,17
Cr	Chromium	0,00	0,00	0,00	0,00
Mn	Manganese	0,00	0,00	0,01	0,04

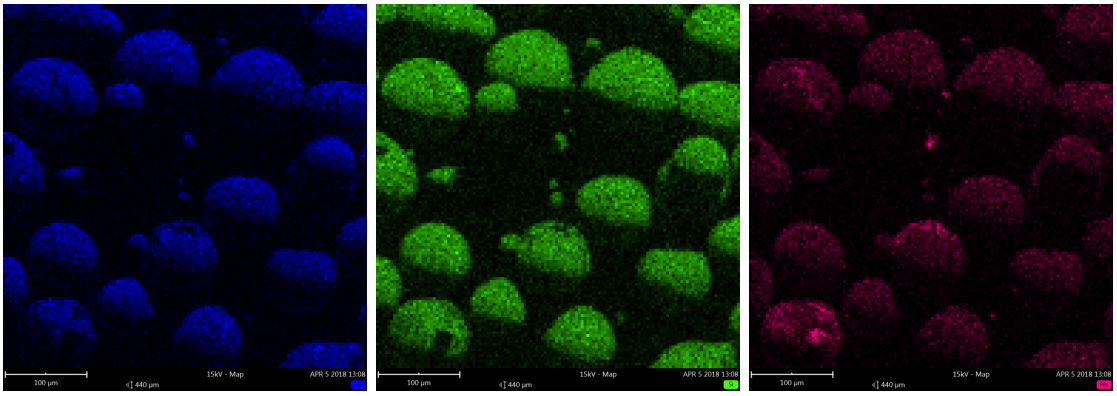

(a) Oxygen. (b) Silicon. (c) Sodium.

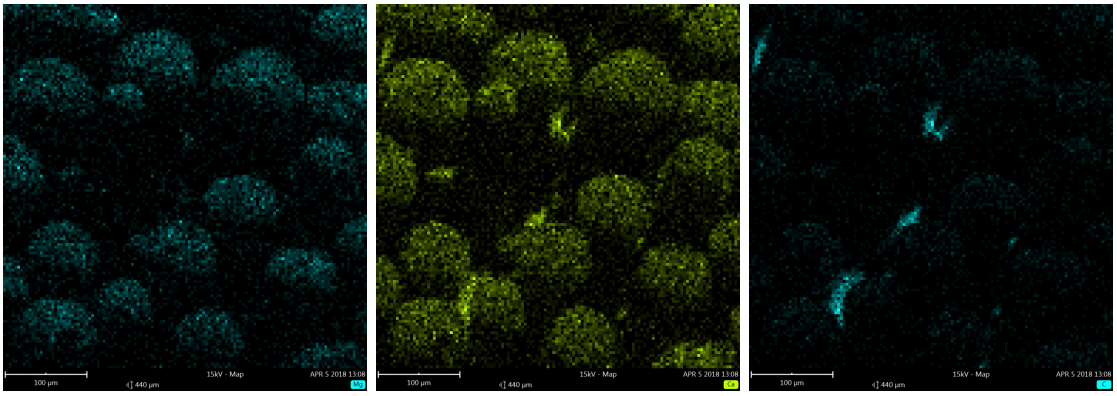

(d) Magnesium. (e) Calcium. (f) Carbon.

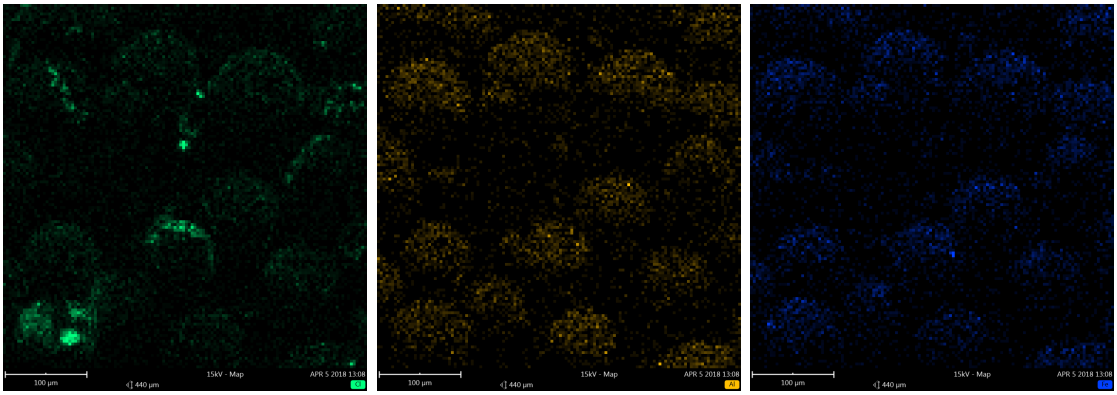

(g) Chlorine. (h) Aluminum. (i) Iron.

Figure 172: Element mapping on material 70-110 μm mixed with NaCl, before usage in CFB.

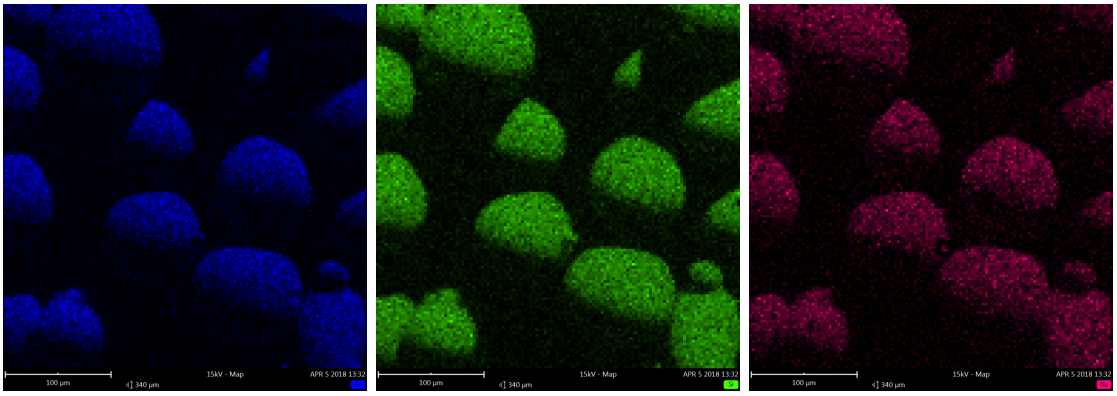

(a) Oxygen. (b) Silicon. (c) Sodium.

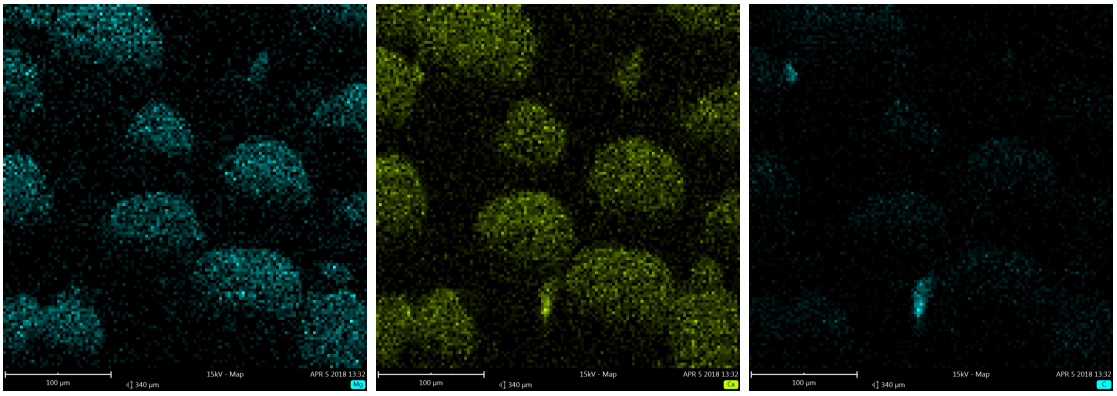

(d) Magnesium. (e) Calcium. (f) Carbon.

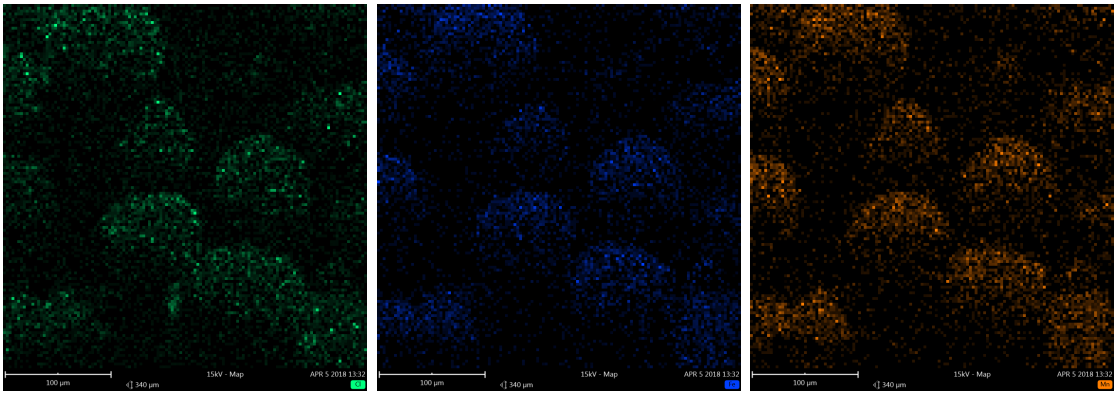

(g) Chlorine. (h) Iron. (i) Manganese.

Figure 173: Element mapping on material 70-110 μm mixed with NaCl, after usage in CFB.

14.2 Material 100-200 μm

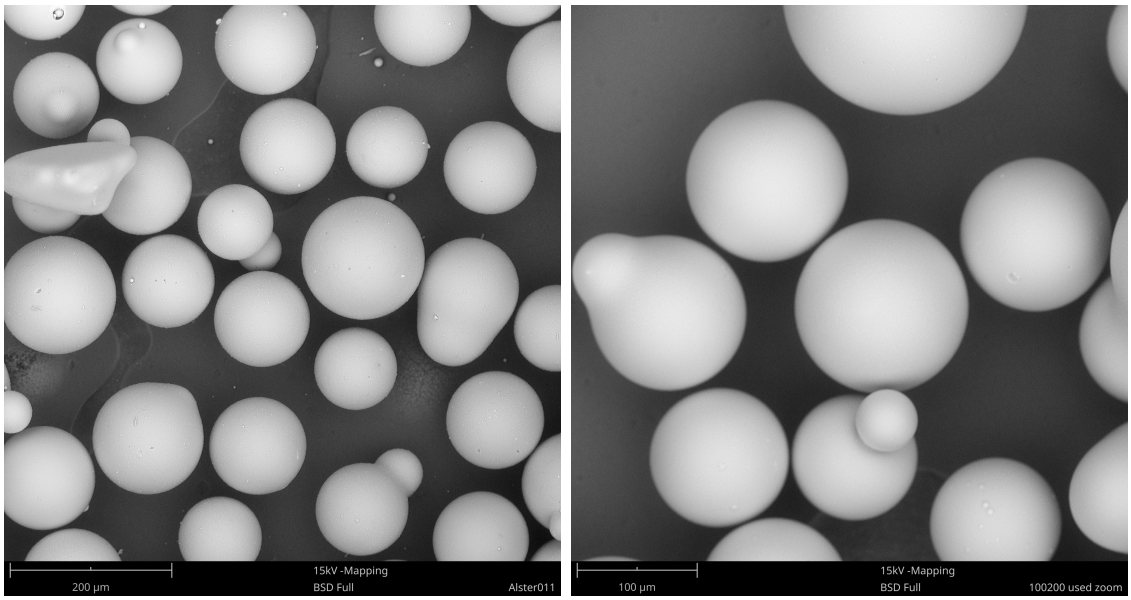

(a) Unused material. (b) Used material.

Figure 174: Material 100-200 μm before and after usage in CFB.

Table 30: Result from element mapping on material 100-200 μm, unused- and used material.

Element symbol	**Element name**	**Unused material**		**Used material**	
		Atomic conc.	**Weight conc.**	**Atomic conc.**	**Weight conc.**
O	Oxygen	68.78	57.48	66.67	56.71
Si	Silicon	14.48	21.25	13.59	20.28
Na	Sodium	11.73	14.09	10.91	13.33
C	Carbon	0.85	0.54	4.86	3.10
Mg	Magnesium	2.51	3.19	2.33	3.01
Ca	Calcium	1.60	3.35	1.57	3.34
Fe	Iron	0.04	0.11	0.06	0.18
Cr	Chromium	0.00	0.00	0.02	0.05

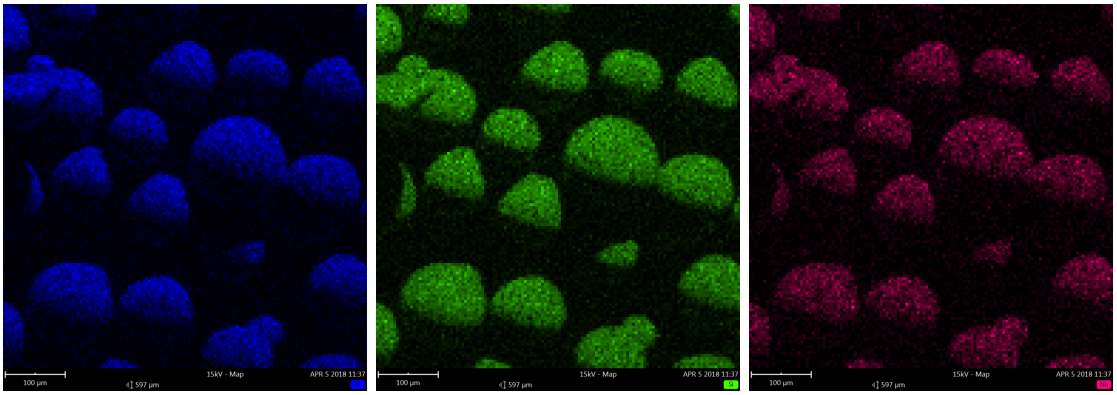

(a) Oxygen. (b) Silicon. (c) Sodium.

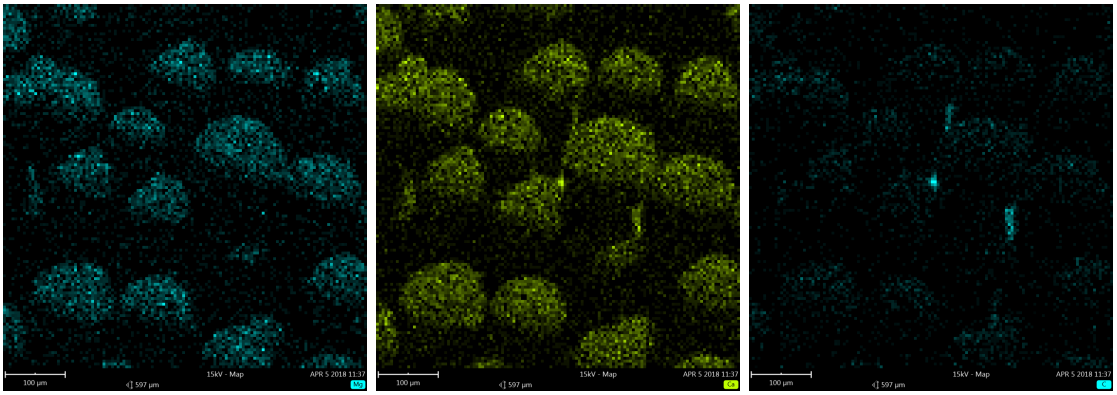

(d) Magnesium. (e) Calcium. (f) Carbon.

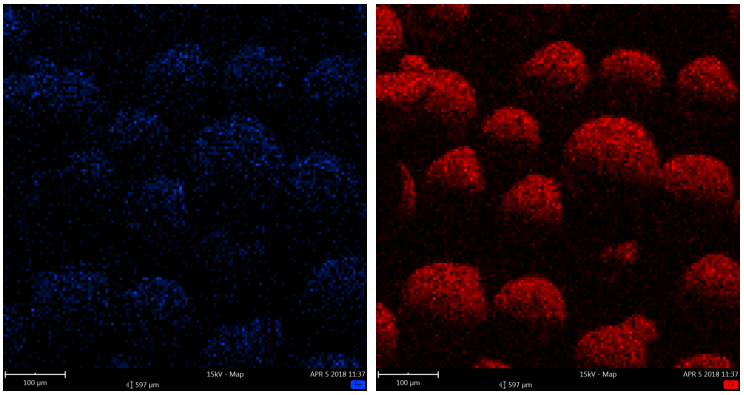

(g) Iron. (h) Chromium.

Figure 175: Element mapping on material 100-200 μm before usage in CFB.

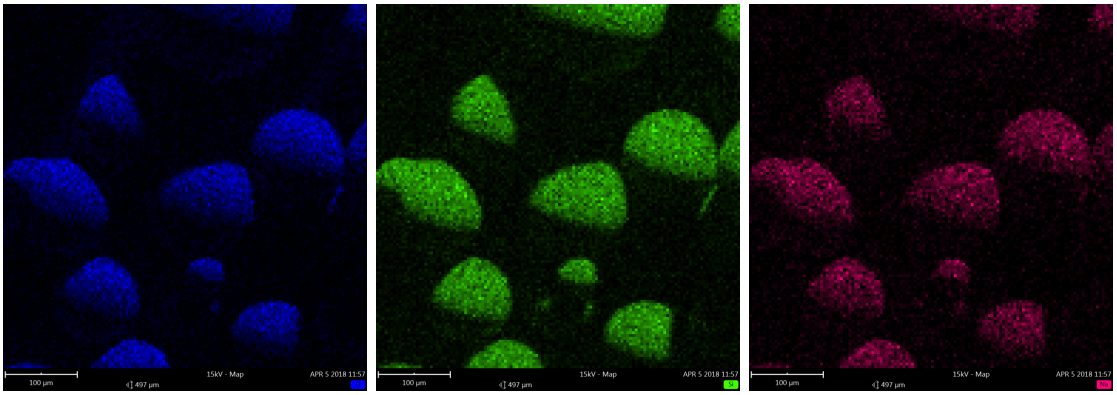

(a) Oxygen. (b) Silicon. (c) Sodium.

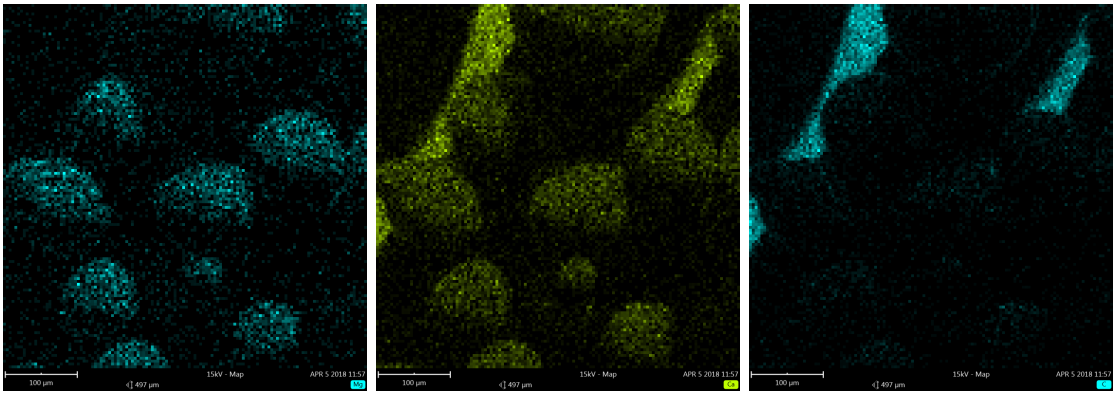

(d) Magnesium. (e) Calcium. (f) Carbon.

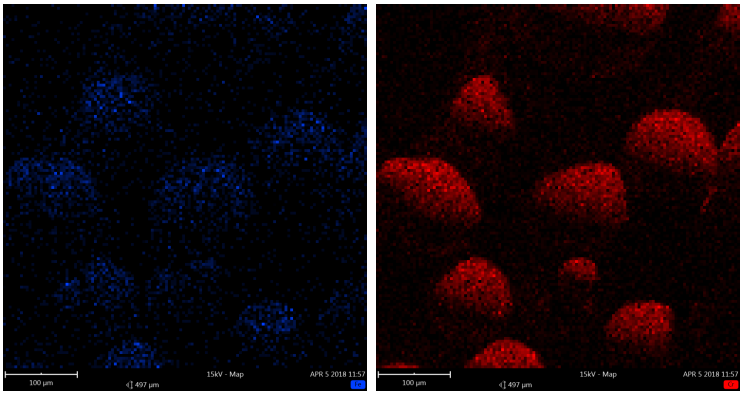

(g) Iron. (h) Chromium.

Figure 176: Element mapping on material 100-200 μm after usage in CFB.

14.3 Material 200-300 μm

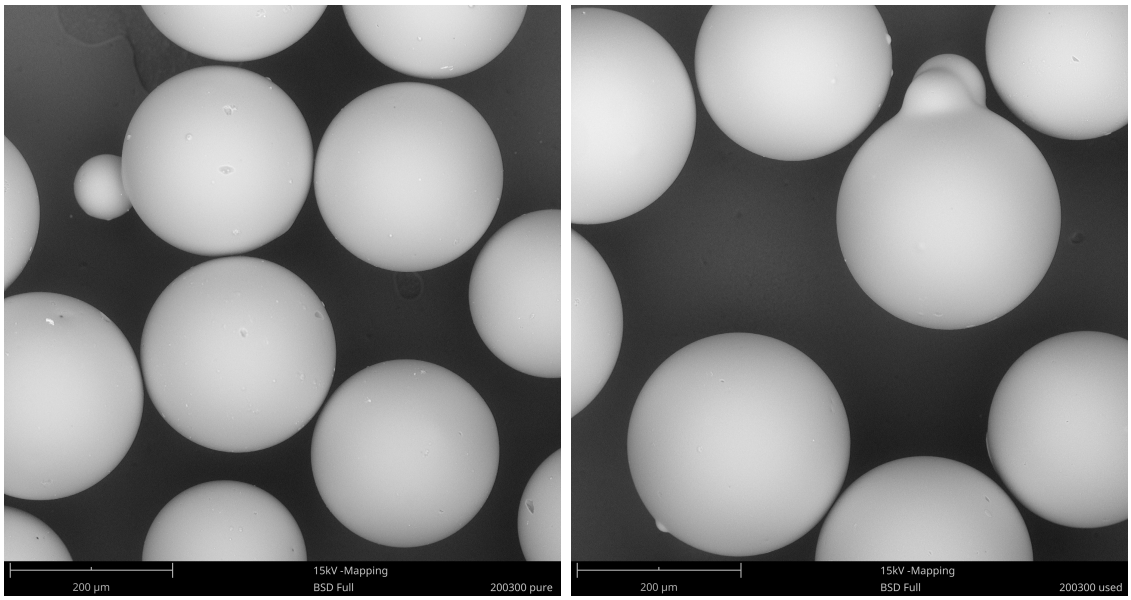

(a) Unused material. (b) Used material.

Figure 177: Material 200-300 μm before and after usage in CFB.

Element analysis, mean value from four different points on the surface of the material.

Table 31: Result from element point analysis on material 200-300 μm, unused- and used material.

Element symbol	**Element name**	**Unused material**		**Used material**	
		Atomic conc.	**Weight conc.**	**Atomic conc.**	**Weight conc.**
O	Oxygen	64.31	52.47	63.00	50.45
Si	Silicon	17.24	24.58	19.11	26.85
Na	Sodium	11.46	13.40	11.70	13.46
Mg	Magnesium	2.85	3.52	2.89	3.51
Ca	Calcium	1.98	4.03	2.23	4.47
Al	Aluminum	0.68	0.94	0.67	0.91
C	Carbon	1.42	0.39	0.36	0.22
Fe	Iron	0.02	0.06	0.05	0.13
Cr	Chromium	0.01	0.02	0.01	0.02
Mn	Manganese	0.03	0.09	0.01	0.02